Rock physics and seismic AVA analysis of gas hydrate-bearing sediments

Sveinung Styve Rundhovde

Thesis for the degree
Master of Science

Department of Earth Science
University of Bergen

June 2014

Abstract

Large amount of natural gas are present in submarine sediments and permafrost areas in the form of gas hydrates. Gas hydrates are a large potential future energy resource, and may contribute to the methane balance in the atmosphere, causing global climate change. Dissociation of gas hydrates can cause seafloor instabilities below constructions such as platforms and pipelines. It is therefore important to be able to quantify the amount of gas hydrate in the sediment.

Rock physics models serve as a link between in-situ properties in the rock and observable properties at the surface. Information regarding seismic properties can be extracted from AVA data via a reflectivity model, and related to hydrate saturation using a rock physics model. Three phase effective medium theory, and a combination of the self consistent approximation and differential effective medium theory are implicated and compared. Large differences in estimated properties were observed for the different models.

When a forward model has been applied, that relates reservoir parameters to AVA data, estimates on these parameters on the basis of data can be made. When the data contain noise, errors in the data are mapped to the estimates on model parameters. Uncertainty analysis was performed in order to investigate the effects of errors in the data. It was seen that when the "true" model is used for inversion, it is possible to make good estimates on the model parameters. When a different model was used for inversion than for the forward modeling, the estimates where good in some cases, and very poor in other.

Acknowledgement

First of all, I would like to express my gratitude towards my supervisor, Professor Morten Jakobsen, for his great guidance, input and discussion. He has from the beginning of my degree taught me about rock physics, seismic wave propagation and inversion, through lectures and meetings. I would also like to thank my co-supervisor, Associate Professor Henk Keers, for teaching me solid earth computational methods using MATLAB.

I want to give a big thank you to my girlfriend for her amazing support and good input. She has stood behind me through the whole process and given me motivation when it was needed.

Finally, I want to thank my parents for their support throughout my time as a student.

Contents

List of Tables

List of Figures

Introduction

Gas hydrate is a solid substance in which the molecules of gas and water chemically interact to form a ice-like crystalline structure. Structurally they are clathrates or compounds which consist of a rigid network of "cages" of water molecules surrounding a gas molecule. Three crystalline structures of gas hydrates I, II and H has been recognized in nature with I being the most common (Kvendvolden, 2000). In order for gas hydrates to form, sufficient amounts of water and suitably sized gas molecules needs to be present in the appropriate pressure and temperature regime. Such conditions are found in continental margins where the bottom-water temperature approaches 0 degrees, at water depths greater than 300-500 m, and in permafrost areas.

The most common indicator of the presence of submarine gas hydrates is an anomaly known as a bottom simulating reflector (BSR), which is a strong inverse polarity reflector that is sub-parallel to the seafloor. The BSR marks the boundary between the higher-velocity hydrate saturated sediment and the lower-velocity underlying sediment, containing brine or a mixture of free gas and brine. This reflector coincides with the base of what is known as the gas hydrate stability zone, which is the region where the temperature and pressure conditions are such that the stability conditions for gas hydrate formation is met. Outside this zone, gas hydrates will dissociate into their water and gas components. Bottom simulating reflectors have been mapped between 100 and 1100 meters beneath the seafloor (Kvenvolden and McMenamin, 1980). They can in many cases be easily recognized because they cut across structural or stratigraphic reflectors.

Recent estimates of the amount of methane contained in gas hydrates range from $3 - 120 * 10^{15}\ m^3$ at standard temperature and pressure conditions (STP), where even the most conservative estimates are large compared to estimates of the conventional gas reserves of $0.15 * 10^{15}\ m^3$ (STP) (Sloan et al., 2009). Because of this and the fact that gas hydrates concentrate methane by as much as a factor of 164 (at STP), and only 15% of the recovered energy is needed for dissociation, gas hydrates are a large potential future energy resource (Sloan et al., 2009). They may also affect the methane balance in the atmosphere, thus influencing global climate (Kvenvolden, 1993). Since gas hydrates affect sediment stiffness, dissociation of gas hydrates can cause seafloor instabilities, and jeopardize the foundation of subsea structures such as platforms and pipelines. Expansion of gas hydrates in the drilling column can also cause blowouts. It is therefore important to be able to quantify the amount of gas hydrates in the sediment.

Hydrate saturation in sediments can be estimated from seismic data by extracting velocity information from the data and then use a rock physics model that relates hydrate saturation to the elastic properties of the sediment. Many attempts have been made to quantify gas hydrate saturation from seismic velocities. Lee et al. (1996) uses a weighted combination of the three phase time average equation and Wood's equation, where in addition to the weighing factor introduced by Nobes et al. (1986) they also introduced an exponential term on the saturation value of the gas hydrate, thereby making the model more flexible so that it can be applicable in the diverse set of growth geometry and conditions where gas hydrates occur in sediments. The disadvantage of this model is that the weighing factors are purely empirical and does not hold any physical meaning, therefore they require substantial data set to be determined.

Other models based on effective medium theory have been made that calculates the elastic properties of the sediments from those of the mineral constituents, porefluids and gas hydrates. These models are based on some assumptions of the grain geometry and connectivity of the sediment, and the hydrate saturation geometry. The best fitting model can therefore be selected from knowledge of the microstructure of the sediment under consideration. The model of Helgerud et al. (1999) is based on hertz-Mindelin contact theory, and hydrates can be added as part of the solid grains or in the pore space, away from grain contacts. Dvorkin and Nur (1995) proposed a model where hydrates can be added as cement at grain contacts, evenly distributed around the grain or concentrated at the grain contact. Another model by Jakobsen et al. (2000) is based on a combination of Self Consistent Approximation (SCA) and Differential Effective Medium Theory (DEM). In this model the gas hydrates can be added as grain coating or in the pore space, and unlike the other models, this model also allows for anisotrophy by first assuming fully aligned elipsoidal clay grains of a certain aspect ratio, and then allowing for varying orientation according to a orientation distribution function.

The outline of this thesis is as follows:

Chapter 1 gives an introduction to the rock physics models that are used in the froward model. The model by Helgerud et al. (1999) and a slightly modified version of the model by Jakobsen et al. (2000) will be introduced. These models will be implemented using MATLAB and results will be plotted and investigated.

Chapter 2 gives an introduction to Aki-Richard's and Rüger's approximations. These are used to model reflectivity properties of a layered model containing a hydrated layer. Also synthetic seismograms are computed using simple seismic modeling.

Chapter 3 gives an introduction to Bayesian non-linear inversion. Inversion experiments will be performed to investigate how noise in data is mapped over to estimates in saturation and porosity. Effects of model error will also be investigated.

Chapter 4 gives concluding remarks and suggestions for further work.

Chapter 1

EFFECTIVE MEDIUM THEORIES OF HYDRATE-BEARING SEDIMENTS

1.1 Introduction

In order to estimate gas hydrate saturation from seismic data it is essential to establish a relation between the gas hydrate saturation and elastic properties of the rock. This is done by using a rock physic model. A rock physics model is a mathematical relation that provides the connection between measurable elastic properties measured at the surface, in a borehole or in a laboratory, to the intrinsic properties of a rock such as mineralogy, grain and pore geometry, porosity and connectivity. In this chapter we will investigate two different models, the three phase effective medium (TPEM) model by Helgerud et al. (1999), and the differential effective medium model (DEM) by Jakobsen et al. (2000). The sensitivity of the models in relation to hydrate saturation for different hydrate saturation structures will be tested, porosities and mineralogies. We will also look at the effects of aspect ratio for the clay platelets and pores in the DEM model and use two different isotropic versions of this model, one with completely disordered non-spherical components and one with spherical components, along with an anisotropic version with partially aligned non-spherical components.

1.2 Three phase effective medium (TPEM) model

This is a first-principle-based effective medium model by Helgerud et al. (1999), based on the model by Dvorkin et al. (1999). The main assumption of the model is that the elastic moduli of the dry sediment at critical porosity can be described by that of a dense random pack of identical spheres with elastic properties calculated from those of the solid constituents using Hill's (Hill, 1952) averaging formula. The elastic moduli can be calculated for other porosities using Hashin-Strikman bounds as described later in this section. As shown in figure 1.1, the hydrates can be accounted for as part of the pore fluid (case 1A) or as part of the solid grains (case 1B). This model is relatively simple and provides a easy way of calculating the bulk and shear moduli of the sediment, however, it does not take into account the anisotropic effects of

preferred clay particle alignment.

The bulk (K_{HM}) and shear (μ_{HM}) moduli of the dry sediment at critical porosity ϕ_c ($\phi_c = 36\%$ for dense random pack of identical spheres , Nur et al. (1998)), is given by the Hertz-Mindlin contact theory:

$$K_{MH} = \left[\frac{n^2(1-\phi_c)^2\mu^2}{18\pi^2(1-v)^2}P\right]^{1/3}$$

$$\mu_{HM} = \frac{5-4v}{5(2-v)}\left[\frac{3n^2(1-\phi_c)^2\mu^2}{2\pi^2(1-v)^2}P\right]^{1/3}$$

where μ and v is the shear modulus and Poisson's ratio, respectively, of the solid phase and P is the effective pressure and n is the average number of grain contacts per grain in the sphere pack ($\sim$9 for dense random pack of identical spheres, Murphy (1982)). The effective pressure can be approximated by the differential pressure, given by $P = (\rho_b - \rho_w)gD$, where ρ_b and ρ_f is the bulk density of the solid components and fluids respectively, g is the acceleration due to gravity, and D is the depth below the seafloor.

At porosities below critical, the elastic moduli of the dry frame is calculated from the lower Hashin-Strikman bounds, where the upper end member is the solid phase of the sediment, and the lower end member is the sediment at critical porosity. For porosities above critical, lower Hashin-Strikman bounds is used, where the upper end member is the sediment at critical porosity, and the lower end member is the open void space, that has zero elastic moduli. This is gives the following equations for the bulk and shear muduli of the dry frame:

$$K_{dry} = \begin{cases} \left[\frac{\phi/\phi_c}{K_{HM}+\frac{4}{3}\mu_{HM}} + \frac{1-\phi/\phi_c}{K+\frac{4}{3}\mu_{HM}}\right]^{-1} - \frac{4}{3}\mu_{HM} & \phi < \phi_c \\ \left[\frac{(1-\phi)/(1-\phi_c)}{K_{HM}+\frac{4}{3}\mu_{HM}} + \frac{(\phi-\phi_c)/(1-\phi_c)}{\frac{4}{3}\mu_{HM}}\right]^{-1} - \frac{4}{3}\mu_{HM} & \phi \geq \phi_c \end{cases} \tag{1.1}$$

$$\mu_{dry} = \begin{cases} \left[\frac{\phi/\phi_c}{\mu_{HM}+Z} + \frac{1-\phi/\phi_c}{\mu+Z}\right]^{-1} - Z & \phi < \phi_c \\ \left[\frac{(1-\phi)/(1-\phi_c)}{\mu_{HM}+Z} + \frac{(\phi-\phi_c)/(1-\phi_c)}{Z}\right]^{-1} - Z & \phi \geq \phi_c \end{cases} \tag{1.2}$$

$$Z = \frac{\mu_{HM}}{6}\left(\frac{9K_{HM}+8\mu_{HM}}{K_{HM}+2\mu_{HM}}\right)$$

For sediment saturated with pore fluid of bulk modulus K_f, the shear modulus remains unchanged $\mu_{sat} = \mu_{dry}$, and the bulk modulus K_{sat} is calculated from Gassman's equation:

$$K_{sat} = K\frac{\phi K_{dry} - (1+\phi)K_f K_{dry}/K + K_f}{(1-\phi)K_f + \phi K - K_f K_{dry}/K} \tag{1.3}$$

Finally, the bulk and shear moduli calculated from the equations above and the bulk density $\overline{\rho}$ of the sediment is used to find the seismic velocities:

$$V_p = \sqrt{(K_{sat} + (4/3)\,\mu_{sat})/\overline{\rho}}, \qquad V_s = \sqrt{\mu_{sat}/\overline{\rho}}$$

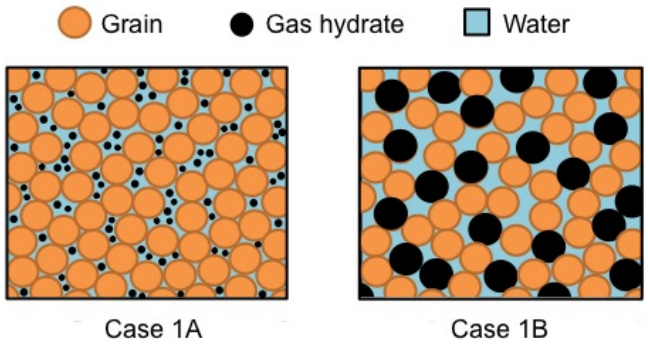

Figure 1.1: Simplified view of the two different hydrate saturation geometries implied by this model. In case 1A the hydrates are distributed in the pore space and in model 1B they form part of the solid frame.

We can account for mixed mineralogy in the solid frame by volume averaging using Hill's formula to calculate the effective elastic parameters from those of the individual mineral constituents, which can be expressed in terms of the effective bulk and shear modulus as:

$$K = \frac{1}{2}\left[\sum_{i=1}^{m} f_i K_i + \left(\sum_{i=1}^{m} f_i/K_i\right)^{-1}\right], \qquad \mu = \frac{1}{2}\left[\sum_{i=1}^{m} f_i \mu_i + \left(\sum_{i=1}^{m} f_i/\mu_i\right)^{-1}\right], \tag{1.4}$$

where m is the number of mineral constituents, f_i, K_i and μ_i are the volume fraction in the solid phase, bulk modulus and shear modulus of the i-th mineral constituent, respectively.

In the case where we assume that hydrates are located in the pore space, away from the solid grains, the elastic constants of the solid frame remain unchanged and the effective bulk modulus $\overline{K}_f$ of the fluid is calculated from Reuss average of the water and gas hydrate bulk moduli (assuming uniform distribution of water and hydrate in the pore space):

$$\overline{K}_f = \left[S_h/K_h + (1 - S_h)/K_f\right]^{-1}, \tag{1.5}$$

where K_h and S_h are the bulk modulus and volumetric concentration in the pore space of the gas hydrate, respectively. K_f in equation 1.3 is then replaced with $\overline{K}_f$ to calculate the effective bulk modulus of the sediment with hydrates. The presence of uniformly distributed gas in the pore space can be accounted for by replacing S_h and K_h in equation 1.5 by the gas saturation (S_g) and bulk modulus (K_g).

If we assume that the hydrates are forming load bearing components of the solid frame, the original porosity will be reduced to $\phi^* = (1 - S_h)\,\phi$, and the fractions of the mineral constituents in equation 1.4 will be replaced by the new mineral fractions f_i^* and the fraction of hydrates in the solid frame f_h, given by:

$$f_i^* = f_i\,(1 - \phi)\,/\,(1 - \phi^*), \qquad f_h = S_h\phi/(1 - \phi^*) \tag{1.6}$$

1.3 Differential effective medium (DEM) model

Jakobsen et al. (2000) proposed a method for modeling clay-rich sediment containing gas hydrates, based on a combination of self-consistent approximation (SCA) (Willis, 1977), differential effective medium theory (DEM) (Nishizawa, 1982), and a method of smoothing (Bonilla and Keller, 1985). The combination of SCA/DEM reproduces the biconnectivity of the sediment Sheng (1990), and a similar approach was shown to give convincing results for the prediction of properties of shale by Hornby et al. (1994). This model starts with an effective material, created by the SCA, at a porosity where this approximation yields a biconnected material (between 40-60% (Sheng, 1990)). Since DEM preserves the connectivity of the phases (Sheng, 1990), the combination can produce a composite that is biconnected at any porosity. In this section, a brief description of this method will be given, however, the method of smoothing used in Jakobsen et al. (2000) will be replaced by Hill average as used in Hornby et al. (1994). This model allows for the anisotropic effect of prefered clay particle alignment.

We consider a statistically uniform composite with a matrix consisting of n different phases with elastic moduli $\mathbf{C}_i$ and volume concentrations v_i $(i = 1, 2, ..., n)$. The self-consistent approximation (SCA) gives the following implicit equation for the stiffness $\mathbf{C}$ of this composite (Willis, 1977):

$$\mathbf{C} = \left\{ \sum_{i=1}^{n} v_i \mathbf{C}_i \mathbf{Q}_i \right\} \left\{ \sum_{j=1}^{n} v_j \mathbf{Q}_j \right\}^{-1}, \tag{1.7}$$

where

$$\mathbf{Q}_i = [\mathbf{I} + \mathbf{P}(\mathbf{C})(\mathbf{C}_i - \mathbf{C})\mathbf{Q}_i] \tag{1.8}$$

and $\mathbf{P}$ is a fourth-rank tensor calculated from the response of a single inclusion embedded in an unbound matrix of the effective material, and $\mathbf{I}$ is the identity tensor. It is assumed that the composite material consists of individual crystals, which each can be approximated by an ellipsoid. $\mathbf{P}$ is found by solving the Eshelby problem (Eshelby, 1957; Mura, 1982; Jakobsen et al., 2000), which involves calculating the strain field in an ellipsoidal region that has been subject to an additional (stress-free) eigenstrain.

The differential effective medium theory (DEM) (Nishizawa, 1982) states that the change in stiffness $d\mathbf{C}$ due to an increment dv_i of the ith component is given by

$$d\mathbf{C} = \frac{dv_i}{1 - v_i} \left(\mathbf{C}_i - \mathbf{C} \right) \mathbf{Q}_i. \tag{1.9}$$

The concentration of all the other components changes proportional to their relative concentrations

$$dv_i = -\frac{v_j dv_i}{\Sigma_{k \neq i} v_k}, \quad j \neq i. \tag{1.10}$$

We can impose a increment dv in the first component and $-dv$ in the second component, leaving the other components as they were, using a modified version of the differential effective medium

theory (DEM) (Jakobsen et al., 2000)

$$d\mathbf{C} = dv\left(\mathbf{C}_1 - \mathbf{C}\right)\mathbf{Q}_1 - dv\left(\mathbf{C}_2 - \mathbf{C}\right)\mathbf{Q}_2, \tag{1.11}$$

where $dv = dv_1/\left(1 - v_1\right)$ and $-dv = dv_2/\left(1 - v_2\right)$.

The combination of SCA/DEM yields a composite with fully alligned microstructure. In reality sedimentary materials are much more heterogeneous. This can be accounted for using the Hill average (following Hornby et al. (1994)). This is given as the mean of the Voigt (1928) average and Reuss (1929) average. It is assumed that the material is an aggregate of crystals where each crystal has a fully aligned microstructure from the SCA/DEM combination. The crystals are assumed to have azimuthal symmetry about their individual axis of transverse isotropy. In this case only the angle θ between the crystalline symmetry axis and the composite symmetry axis needs to be considered (Hornby et al., 1994).

The following scheme for calculating the Voigt average is extracted from Jakobsen (1998). The crystals are oriented according to a orientation distribution function $W\left(\Omega\right)$, where ω is the orientation of a crystal referred to a fixed coordinate system. $\Omega = (\xi, \varphi, \psi)$, where ξ ,φ and ψ are the three Eulerian angles and $\xi = cos(\theta)$. All the crystals must have some orientation, therefore it follows that:

$$\int W\left(\Omega\right) d\Omega = 1. \tag{1.12}$$

We let $C_{ijkl}\left(0\right)$ denote the stiffness of a crystal referred to the axis of transverse isotropy fixed in each crystal. The stiffness of a crystal with orientation given by Ω, referred to a fixed background axis is then (Morris, 1969; Sayers, 1994):

$$C_{ijkl}\left(\Omega\right) = T_{ijklmnpq}\left(\Omega\right) C_{mnpq}\left(0\right), \tag{1.13}$$

where $T_{ijklmnpq}$ is the transformation tensor corresponding to Ω.

The weighted average of the elastic stiffness tensor is (Morris, 1969)

$$\overline{C}_{ijkl} = \overline{T}_{ijklmnpq} C_{mnpq}\left(0\right), \tag{1.14}$$

where

$$\overline{T}_{ijklmnpq} = \int W\left(\Omega\right) T_{ijklmnpq}\left(\Omega\right) d\Omega, \tag{1.15}$$

is the averaging operator.

Following Sayers (1994) we then expand W as a series of generalized Legendre functions $Z_{lmn}\left(\xi\right)$:

$$W\left(\Omega\right) = W\left(\xi, \varphi, \psi\right) = \sum_{l=0}^{\infty} \sum_{m=-l}^{l} \sum_{n=-l}^{l} W_{lmn} Z_{lmn}\left(\xi\right) e^{-im\varphi} e^{-in\psi}, \tag{1.16}$$

where

$$W_{lmn} = \frac{1}{4\pi^2} \int_0^{2\pi} \int_0^{2\pi} \int_{-1}^{1} W\left(\xi, \varphi, \psi\right) Z_{lmn}\left(\xi\right) e^{im\varphi} e^{in\psi} d\xi d\varphi d\psi \tag{1.17}$$

If the orientation distribution is symmetric about the axis $\theta = 0$, then W becomes dependent on ξ only and the parameters W_{lmn} are all zero unless $m = n = 0$. Since $W(\xi) = W(-\xi)$ we also have that W_{l00} is zero unless l is even. The Voigt matrix representations of $\overline{C}_{ijkl}$ can then be calculated from $C_{ijkl}(0)$, W_{200} and W_{400} only, using the following equations (Sayers, 1994):

$$\overline{C}_{11} = \overline{C}_{22} = \lambda + 2\mu + \frac{4\sqrt{2}}{105}\pi^2 \left[2\sqrt{5}a_3 W_{200} + 3a_1 W_{400}\right], \tag{1.18}$$

$$\overline{C}_{33} = \lambda + 2\mu - \frac{16\sqrt{2}}{105}\pi^2 \left[\sqrt{5}a_3 W_{200} - 2a_1 W_{400}\right], \tag{1.19}$$

$$\overline{C}_{12} = \lambda - \frac{4\sqrt{2}}{315}\pi^2 \left[2\sqrt{5}\left(7a_2 - a_3\right) W_{200} - 3a_1 W_{400}\right], \tag{1.20}$$

$$\overline{C}_{13} = \overline{C}_{23} = \lambda - \frac{4\sqrt{2}}{315}\pi^2 \left[\sqrt{5}\left(7a_2 - a_3\right) W_{200} - 12a_1 W_{400}\right], \tag{1.21}$$

$$\overline{C}_{44} = \overline{C}_{55} = \mu - \frac{2\sqrt{2}}{315}\pi^2 \left[\sqrt{5}\left(7a_2 + 2a_3\right) W_{200} + 24a_1 W_{400}\right], \tag{1.22}$$

$$\overline{C}_{66} = \left(\overline{C}_{11} - \overline{C}_{12}\right)/2, \tag{1.23}$$

where a_1, a_2 and a_3 are defined by

$$a_1 = C_{11}(0) + C_{33}(0) - 2C_{13}(0) - 4C_{55}(0), \tag{1.24}$$

$$a_2 = C_{11}(0) - 3C_{12}(0) + 2C_{13}(0) - 2C_{55}(0), \tag{1.25}$$

$$a_3 = 4C_{11}(0) - 3C_{33}(0) + C_{13}(0) - 2C_{55}(0), \tag{1.26}$$

λ and μ are given by

$$15\lambda = C_{11}(0) + C_{33}(0) + 5C_{12}(0) + 8C_{13}(0) - 4C_{55}(0), \tag{1.27}$$

$$30\mu = 7C_{11}(0) + 2C_{33}(0) - 5C_{12}(0) - 4C_{13}(0) + 12C_{55}(0), \tag{1.28}$$

and the formulas for W_{200} and W_{400} are

$$W_{200} = \frac{5}{2}\int_{-1}^{1} W(\xi) P_2(\xi)\, d\xi, \tag{1.29}$$

$$W_{400} = \frac{5}{2}\int_{-1}^{1} W(\xi) P_4(\xi)\, d\xi, \tag{1.30}$$

where P_n is the Legendre polynomal of order n.

The Reuss average is found exactly the same way, by replacing the stiffness components in equation 1.18-1.23 by the corresponding compliance components. The Hill average is then calculated from

$$\overline{\mathbf{C}}^{VRH} = \frac{\overline{\mathbf{C}}^{V} + \overline{\mathbf{C}}^{R}}{2}, \tag{1.31}$$

where $\overline{\mathbf{C}}^{V}$ is the stiffness found from the Voigt average and $\overline{\mathbf{C}}^{R} = \left(\overline{\mathbf{S}}^{R}\right)^{-1}$ is the stiffness from the Reuss average.

We consider two separate cases with a sediment consisting of clay, water, quartz and gas hydrates, at volume concentrations v_c , v_w, v_q and v_h, respectively. A first one where the hydrates are located inside the pore space and a second case where the gas hydrates are forming cement binding around the grains as shown on figure 1.2.

In the case where hydrates are located in the pore space (case 2A), we start by calculating the elastic properties of a fully aligned clay/water composite at water-filled porosity $\phi_0 = \phi/(\phi + v_c)$ using the combination of SCA and DEM (equation 1.7 and 1.9). Consecutive increments dv in the volume concentration of gas hydrates in the sediment and $-dv$ in the water volume concentration are then imposed using modified DEM (equation 1.11), until the desired hydrate saturation $S_h = v_h/\phi_0$ is reached. The hydrate inclusions have the same shape and orientation as the water and clay inclusions and the resulting media is a fully aligned clay/water/hydrate composite with connected clay, connected water and unconnected hydrates.

For the second case (case 2B), where hydrates are present as grain coating, the procedure is exactly the same except that the roles of hydrates and water are interchanged. This yields a clay/water/hydrate composite with connected clay, connected hydrates and unconnected water.

Orientation averaging is then performed using Hill average (equation 1.31), as described above, before isolated quartz inclusions are added using DEM (equation 1.9). The aspect ratio for quartz inclusions should be set to 1. Other minerals, such as feldspar can also be added using this method, but as long as the properties of these minerals are similar to quartz, adding only quartz to represent the unconnected components will be a good approximation.

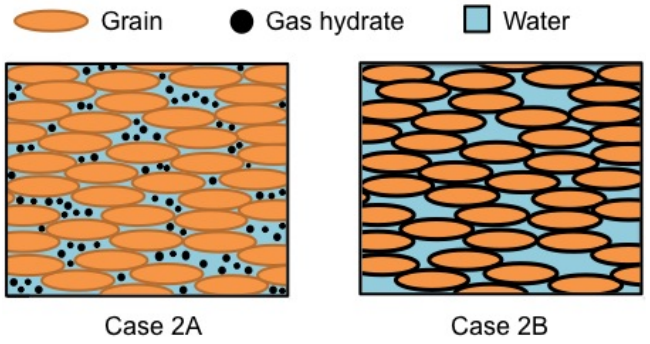

Figure 1.2: Simplified view of the two different hydrate saturation geometries implied by this model. In case 2A the hydrates are distributed in the pore space and in model 2B they are present as grain coating.

1.4 Numerical results and discussion

In order to investigate the effects of gas hydrates on effective elastic parameters, the value of the static parameters used in the models must be determined. The elastic properties of the

components are found in table 1.1. In addition to these parameters and the volume concentration of the components, the models also incorporate some other parameters, related to the microstructure and in-situ conditions. The DEM model is dependent on the aspect ratio of the grains and pores, and the orientation distribution. If the components are isotropic and spherical or randomly oriented, the resulting media will be isotropic (Hornby et al., 1994).

In figures 1.3 and 1.4 the P- and S-wave velocity of a completely disordered clay-water-hydrate-quartz composite are shown as a function of hydrate saturation for different aspect ratios, for hydrates as pore filling and part of the solid frame, respectively. Generally the velocities are higher for higher aspect ratios, except in the case of connected hydrates that fill 100% of the pore space where the velocities seems to merge, and the velocities increase with increasing hydrate saturation for all cases. For the unconnected hydrates the P-wave velocity the P-wave velocities are relatively similar for the different aspect ratios, whereas the S-wave velocities have a much sharper increase for the higher aspect ratios. In the case of connected hydrates, the dependency is more linear for the higher aspect ratios, while the lower aspect ratio show a higher sensitivity with increasing saturation.

Next we will look at the parameters in the TPEM model that are not related to the properties and volume concentration of the components. Figures 1.5 and 1.6 show the velocities plotted as a function of hydrate saturation for different critical porosities and coordination numbers. The values that are used are different results from a packing of identical spheres for the average number of grain contacts and corresponding porosity, taken from Mavko et al. (2009). This appears to have essentially no effect on the velocities. In figures 1.7 and 1.8 the plots are shown for different differential pressures. Also here the effects are modest, but there is an increase in S-wave velocity for the model with hydrates in the pore space over the whole saturation range with increasing pressure, whereas the P-wave velocity is practically unchanged. The model with hydrates as part of the frame also show insignificant effects on the P-wave velocity, and some effect on the S-wave velocity that decreases with increasing saturation before the velocities merge at 100% saturation.

In figures 1.9-1.20 results for three different models are shown, the DEM model with spherical components (DEM spherical), the DEM with completely disordered clay platelets and pores with aspect ratio 1/20 (DEM non-spherical), and the TPEM model. P- and S-wave velocities are plotted as function of hydrate saturation for different porosities and quartz contents. For the TPEM model the effective pressure is set to $5MPa$, and the values used for the coordination number and critical porosity are 9 and 36%, respectively. These values will be used consistently throughout this text.

When the hydrate are distributed in the pore space (figure 1.9-1.14) the models show relatively similar P-wave velocities, especially at higher porosities. When the quartz content is varied, the models only show slight changes. The TPEM model gets a higher velocity at 0% saturation

and a shallower increase so that it has a lower velocity at 100% saturation when the quartz content is increased. The DEM models shows the opposite trend, they start lower and increase more rapidly when the quartz content is higher, with this effect being largest in the case of spherical components.

When it comes to S-wave velocities, the TPEM model shows oposite trend as the other models. It shows a slight decrease with increasing hydrate saturation. This is due to the unchanged shear modulus and slightly increased density caused by the hydrates. This trend is physically questionable since one would expect that the hydrates will contribute to some extent to the shear stiffness of the rock, even at low concentrations. The two other models show sharper increase with hydrate saturation at higher porosities. The effect on the S-wave velocity for the DEM models with varying quartz content is similar to that of the P-wave velocity for these models.

Next we will look at the models with hydrates added as part of the solid frame (Figures 1.15-1.20). As expected, a general trend is a sharper increase in velocity when the hydrates are present as part of the solid frame. The DEM model shows higher velocity at 0% saturation for connected hydrates, where the velocities should be equal. This is not the case for the TPEM model. For both the models, it is assumed that the hydrates are present in the pore space at low concentrations (say less than 50%) and as part of the solid frame at higher concentrations. Therefore, the DEM model with unconnected hydrates should be used to model the sediment when no hydrates are present.

Generally the TPEM model shows a strongly non-linear increase that gets higher as the hydrate saturation increases. This trend is stronger for higher porosities and higher quartz content, and is stronger for S-wave velocities. The DEM models show a more linear trend, though slightly less linear in the case of non-spherical components. The DEM model with spherical components has higher velocity than the non-spherical version up to 100% saturation where the velocities converge. These models show more similar velocities at higher porosities and quartz contents. The velocities increase the most with hydrate saturation for the TPEM model. Regarding the P-wave velocity, this model shows less decrease with porosity than the other models, whereas the S-wave velocity decreases the least for this model. When the quartz content is incremented, the TPEM model shows higher velocities over the whole saturation range, while the velocities decrease at low saturations for the DEM models, and increase at higher saturations.

The DEM model can generate a vertically isotropic (VTI) media by assuming fully or partially aligned microstructure. The anisotropy of a VTI media can be expressed in terms of the anisotropy parameters (Thomsen, 1986):

$$\epsilon = \frac{C_{11} - C_{33}}{2C_{33}}, \tag{1.32}$$

$$\gamma = \frac{C_{66} - C_{44}}{2C_{44}}, \tag{1.33}$$

$$\delta = \frac{(C_{13} + C_{44})^2 - (C_{33} - C_{44})^2}{2C_{33}(C_{33} - C_{44})}, \tag{1.34}$$

where ϵ and γ describe the anisotropy of the P- and S-waves, respectively, and δ is related to the shape of the wavefronts. These parameters, together with the vertical P-wave velocities

$$V_P = \sqrt{C_{33}/\overline{\rho}} \tag{1.35}$$

and S-wave velocities

$$V_S = \sqrt{C_{44}/\overline{\rho}}, \tag{1.36}$$

where $\overline{\rho}$ is the spatial average density of the material, form a convenient measure of the VTI media.

In figure 1.21 these parameters are plotted as a function of aspect ratio for the clay platelets and pores, for a fully aligned DEM composite. The anisotropy parameters are relatively low, except in the case of γ for the unconnected hydrates, where it exceeds 100 for low aspect ratios, and quickly decreases. In figure 1.22 the anisotropy parameters are plotted as function of the standard deviation σ. The grains are assumed to be oriented according to a truncated normal distribution, where the standard deviations shown are the ones of the corresponding un-truncated normal distribution. The anisotropy parameters quickly approaches zero, and already at $\sigma = 2$ the media is nearly isotropic.

Figure 1.23 shows a truncated normal distribution corresponding to a un-truncated normal distribution with $SD = \pi/5$. This distribution will be used for the partially aligned DEM model. In figures 1.24-1.29 the Thomsen's parameters for this model are plotted as function of hydrate concentration for different porosities and quartz contents. Generally, the anisotropy is eliptical ($\epsilon \approx \delta$) and, as expected, the vertical velocities increase more rapidly when the hydrates are present as grain coating.

At low porosities the anisotropy parameters decrease with hydrate saturation, while there is an increase in ϵ and δ at 75% porosity, up to about 50% saturation, before the parameters decrease again. γ always decreases with saturation, while for connected hydrates it drops close to zero at 100% saturation. ϵ and δ are always higher when the hydrates are connected (except in some cases at very high saturation), whereas γ is always lower. There is an increase in γ with porosity, while ϵ and δ decrease at low saturation. All the anisotropy parameters decrease when the quartz content is incremented, something that can be explained by the quartz being added as spherical inclusions.

1.5 Concluding remarks

Two different rock physics models had been implemented and investigated in this chapter, the simple and computationally inexpensive TPEM model and the more complicated and computationally expensive DEM model. The DEM model has been somewhat simplified by replacing

"method of smoothing" with the Hill average. Two different isotropic formulations of the DEM model, one with completely disordered eliptical components and one with spherical components, has been compared with each other and the TPEM model. The DEM model has also been implemented on an anisotropic case, with partially aligned microstructure, and the vertical velocities and anisotropy parameters were calculated.

Generally, the models show similar results at 0% saturation for the plots where the hydrates are located in the pore space. The TPEM model shows the same velocity at 0% saturation when the hydrates form part of the solid frame, whereas the DEM model shows different velocities. This model starts with a clay-water composite when the hydrates are modeled in the pore space, so this model should give the most accurate value in this case. Although the DEM and TPEM model assumed same saturation geometry in the case where hydrates are located in the pore space, they show different trends. The S-wave velocity decreases with hydrate saturation when using the TPEM model. This is the only case where we see a decrease in velocity with hydrate saturation. We have seen that the effects of hydrates on seismic properties calculated using these models can be similar for the different models in some cases and very different in other. In the next chapter we will implement these models on a layered media to investigate the effects this will have on the reflection coefficients and seismic data.

Table 1.1: The component parameters used in the models. The elastic moduli and density of the minerals is taken from Mavko et al. (2009), those of hydrates (structure I methane hydrates) from Waite et al. (1999) and those of water are calculated from Batzle and Wang (1992) (with 30 000 ppm salinity, 35 MPa pressure and 20 C temperature)

	$K(GPa)$	$\mu(GPa)$	$\rho(g/cm^3)$
Clay	21	7	2.6
Quartz	37	44	2.65
Gas hydrate	7.7	3.2	0.9
Brine	2.5	0	1.03
Gas/brine	0.24	0	0.643

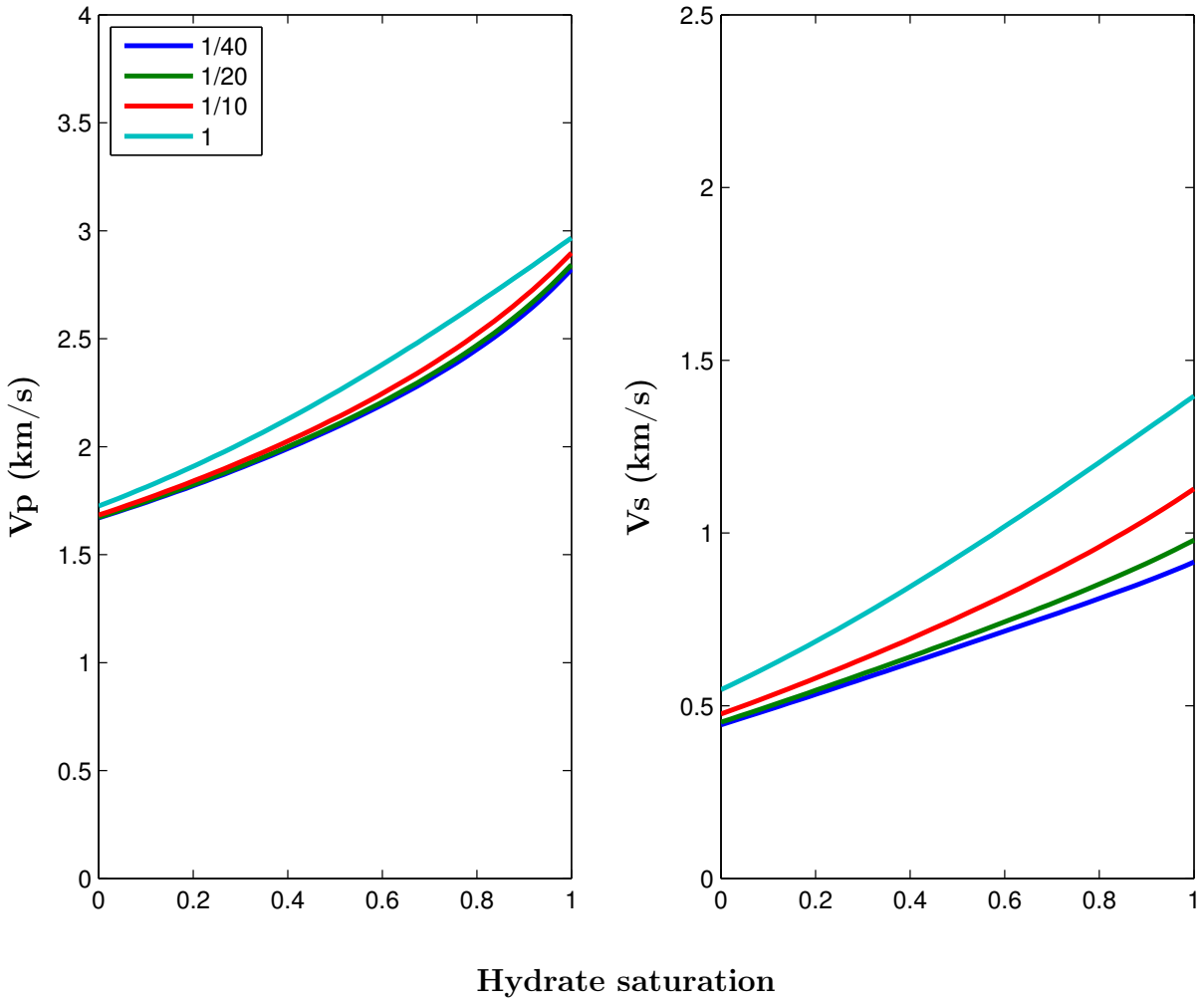

Figure 1.3: V_P and V_S plotted as a function of hydrate saturation at 60% porosity, with hydrates located in the pore space, using the DEM model with different aspect ratio for the clay platelets. The quartz content is 25%.

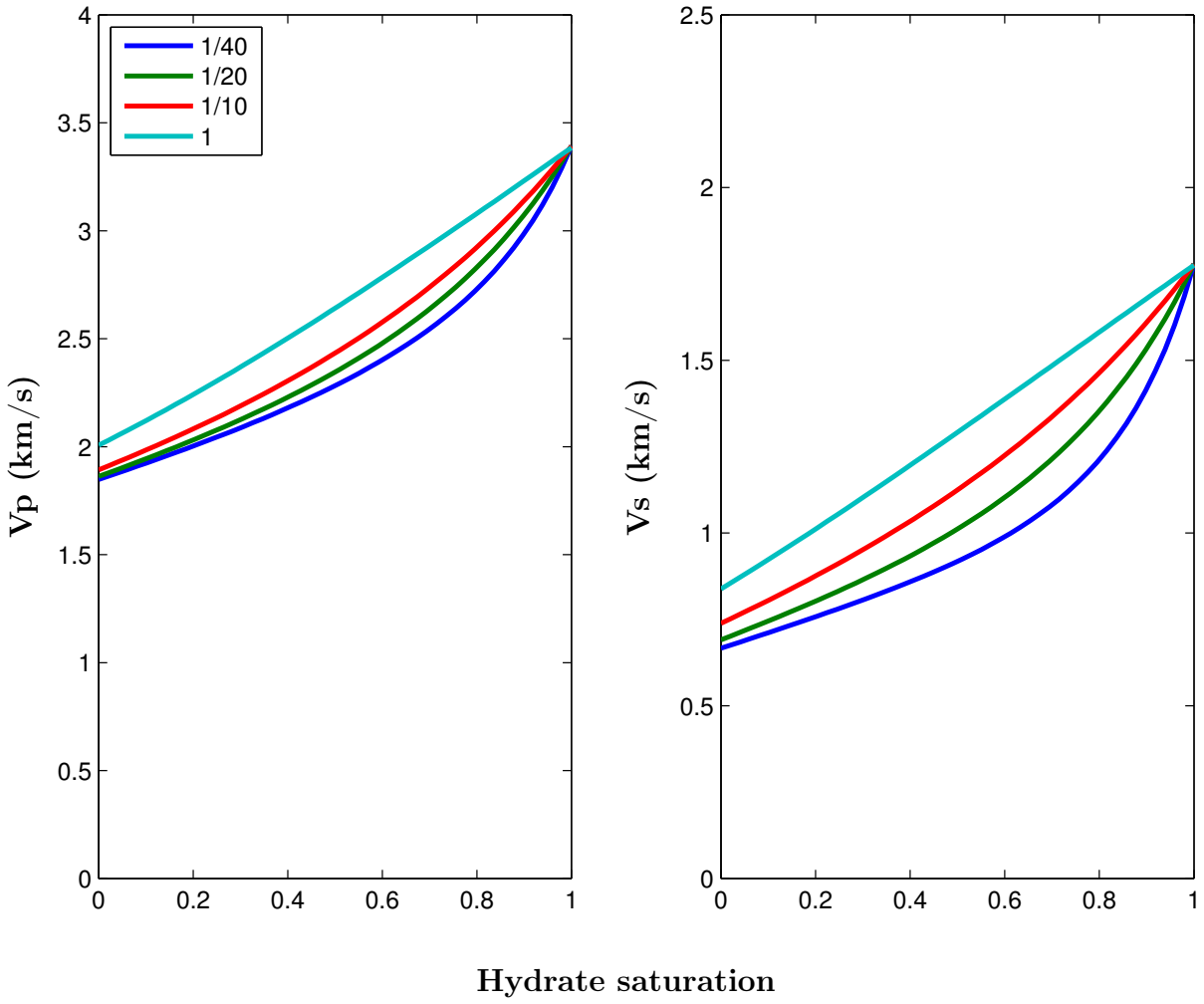

Figure 1.4: V_P and V_S plotted as a function of hydrate saturation at 60% porosity, with hydrates as grain coating, using the DEM model with different aspect ratio for the clay platelets and pores. The quartz content is 25%.

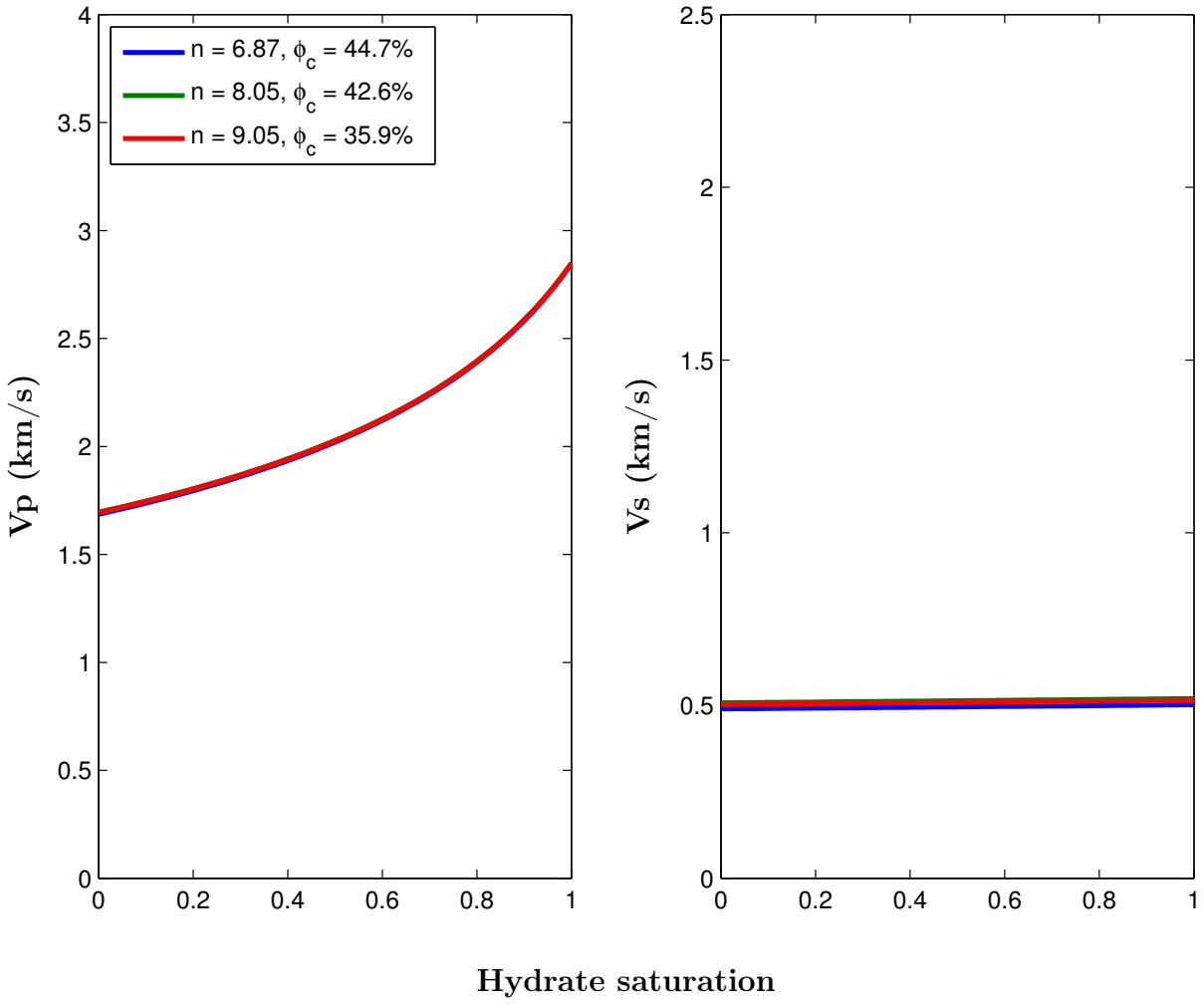

Figure 1.5: V_P and V_S plotted as a function of hydrate saturation at 60% porosity, with hydrates located in the pore space, using the TPEM model with different coordination numbers n. The quartz content is 25% and the depth is set to 300m.

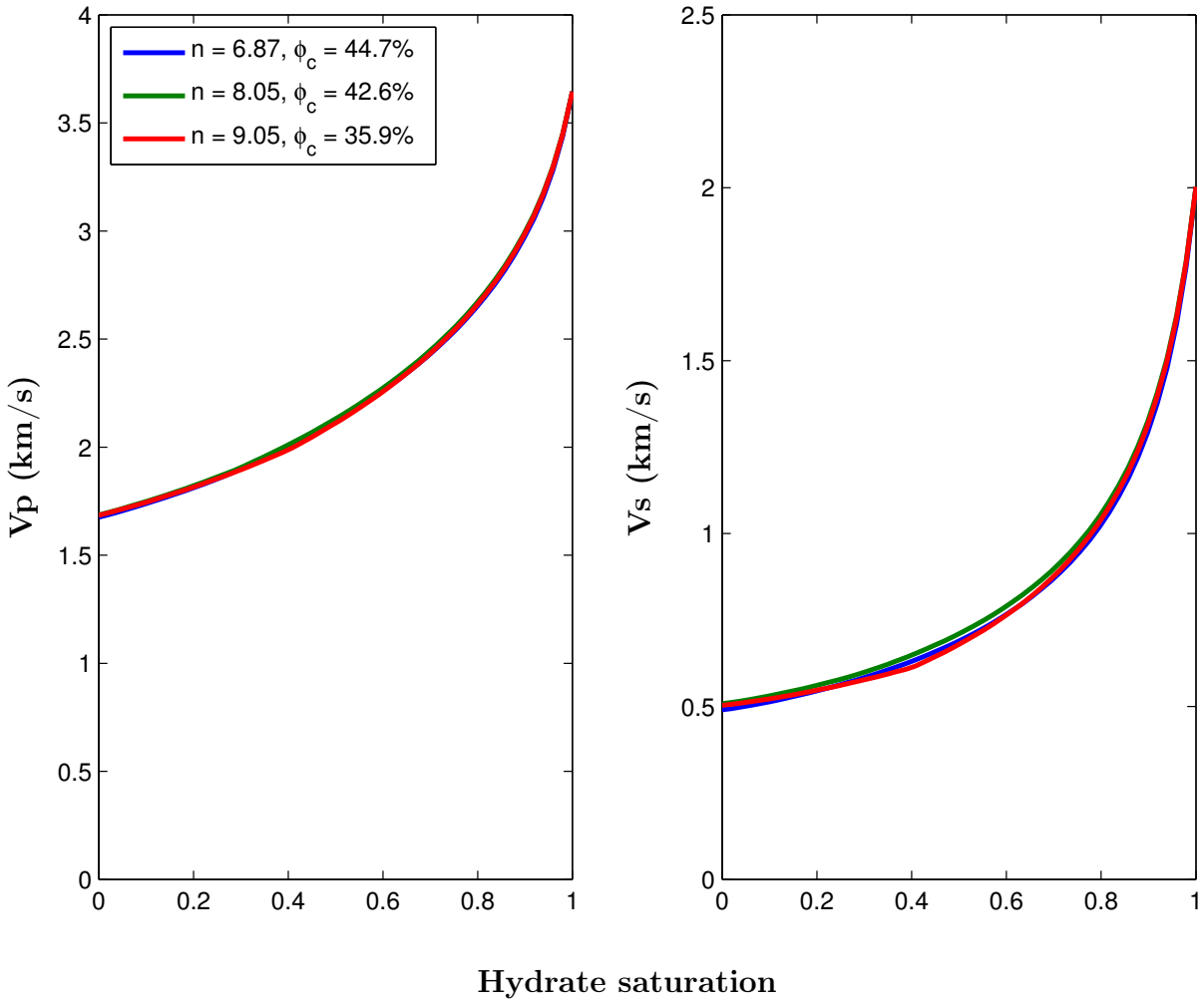

Figure 1.6: V_P and V_S plotted as a function of hydrate saturation at 60% porosity, with hydrates as part of the solid frame, using the TPEM model with different coordination numbers n. The quartz content is 25% and the depth is set to 300m.

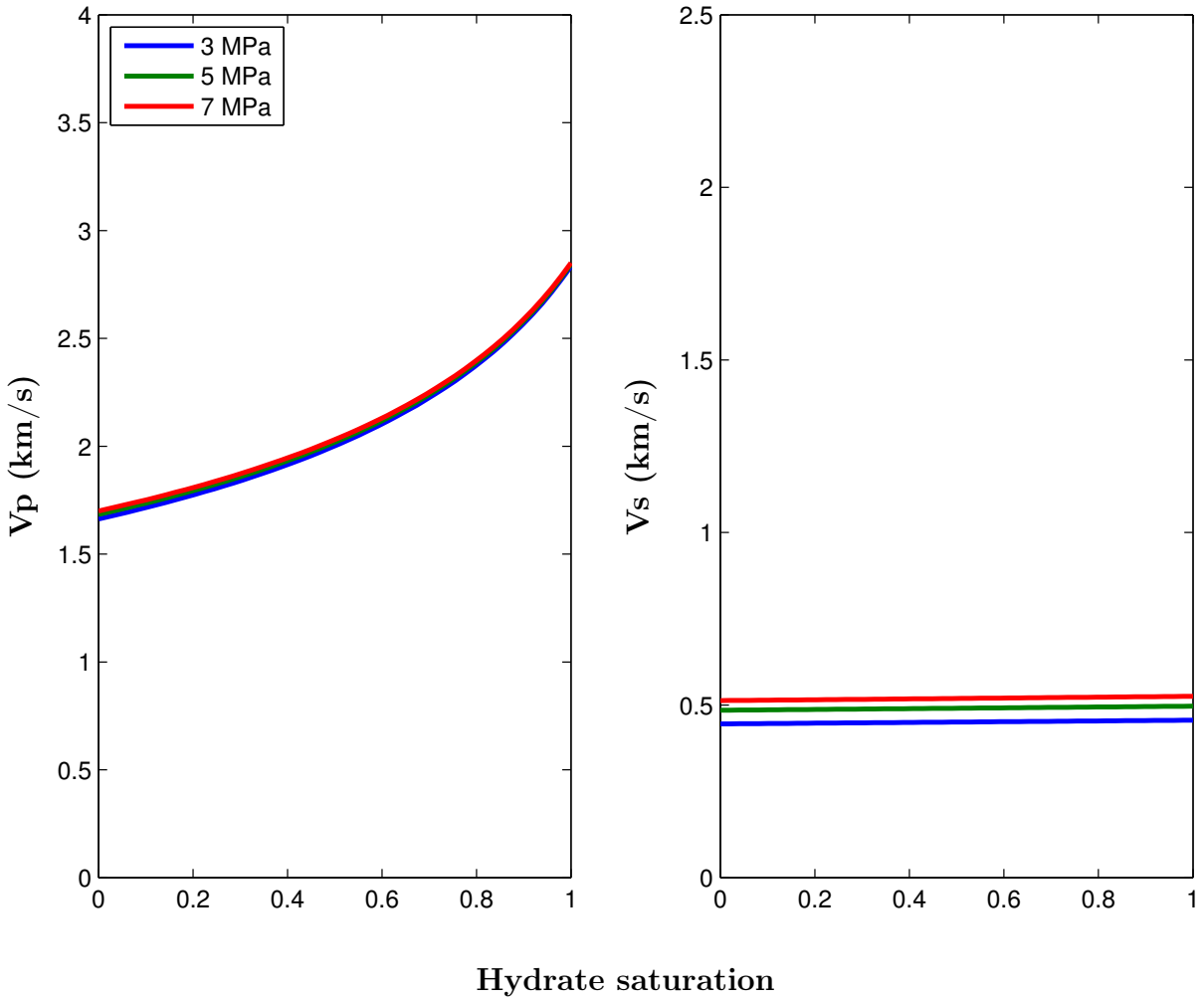

Figure 1.7: V_P and V_S plotted as a function of hydrate saturation at 60% porosity, with hydrates located in the pore space, using the TPEM model with different depths effective pressures. The quartz content is 25%, the coordination number is set to 9 and the critical porosity to 36%.

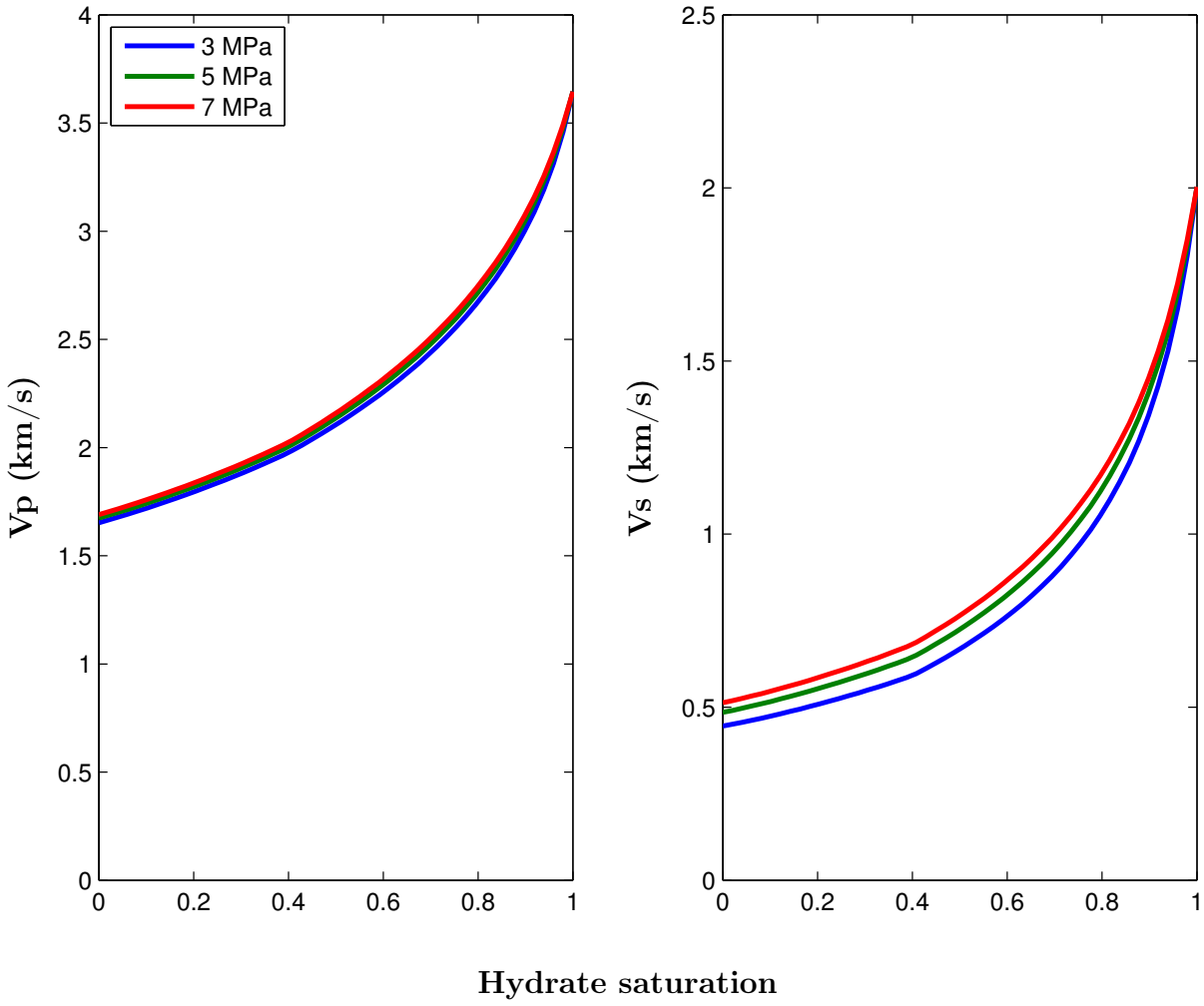

Figure 1.8: V_P and V_S plotted as a function of hydrate saturation at 60% porosity, with hydrates as part of the solid frame, using the TPEM model with different effective pressures. The quartz content is 25%, the coordination number is set to 9 and the critical porosity to 36%.

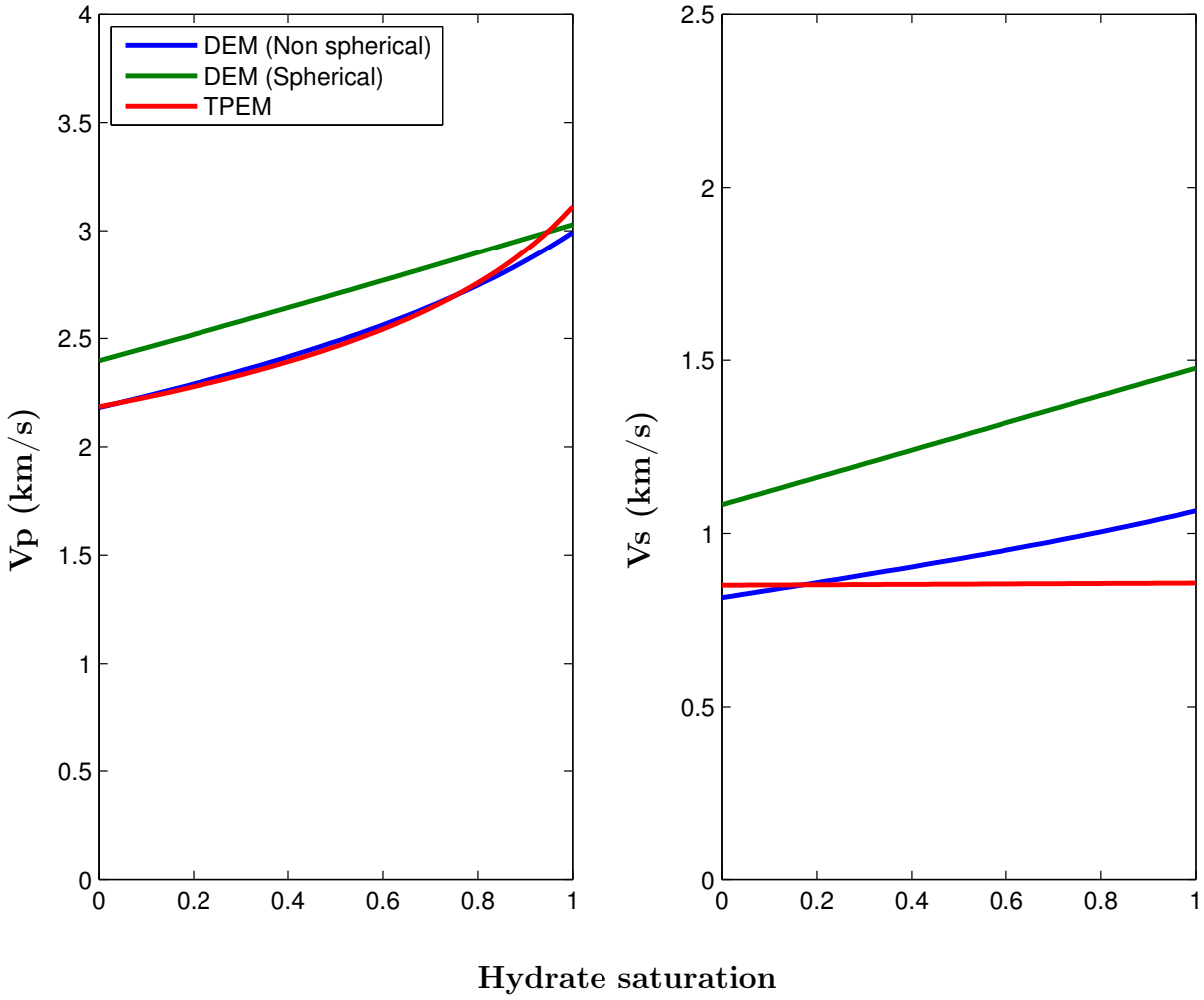

Figure 1.9: V_P and V_S plotted as a function of hydrate saturation at 25% porosity, with hydrates located in the pore space. The blue line is for the DEM model with completely disordered building blocks with aspect ratio 1/20 for the clay platelets and pores. The green line is the DEM model with spherical components. The red line is for the three phase effective medium theory. The quartz fraction is 25%.

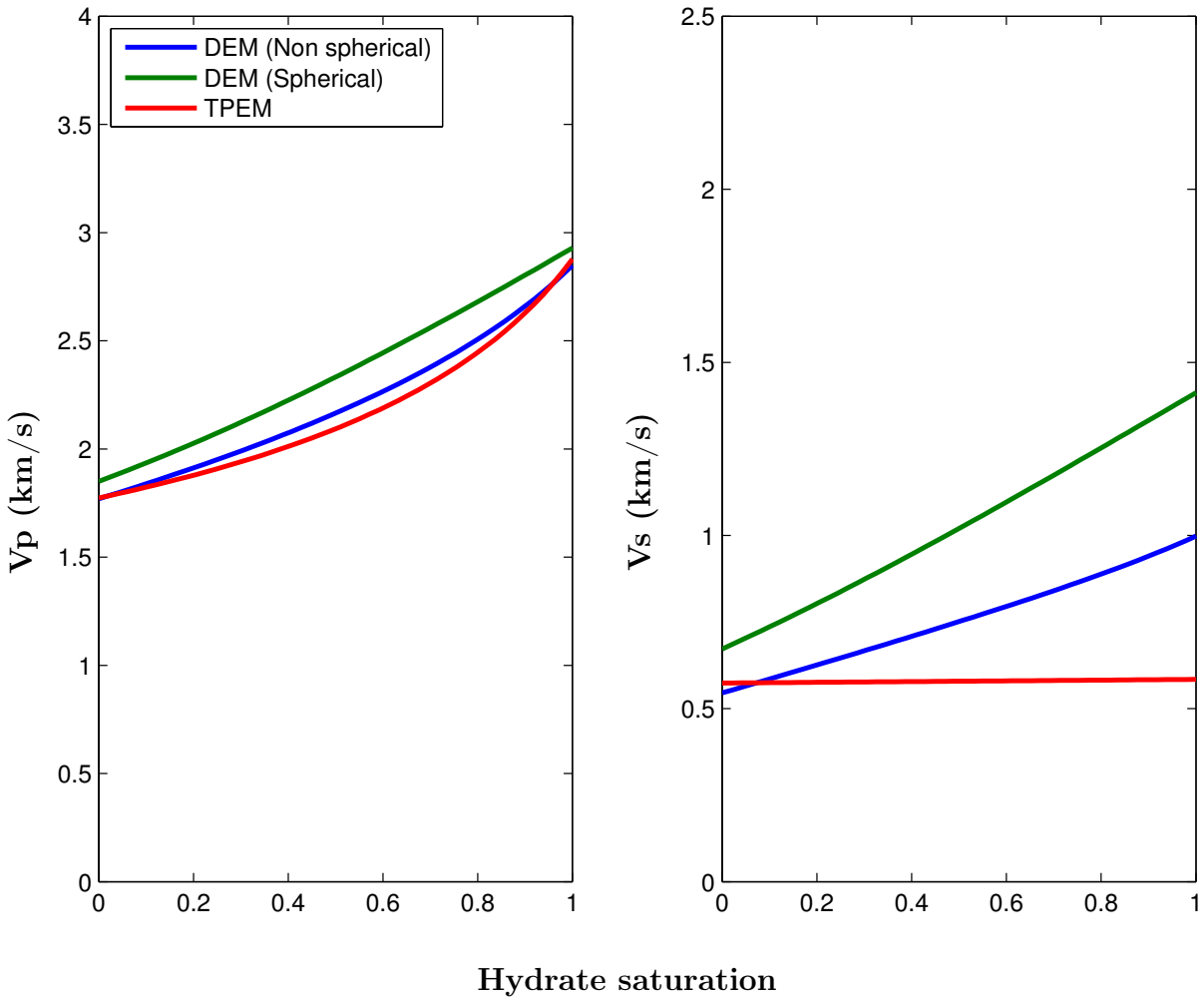

Figure 1.10: V_P and V_S plotted as a function of hydrate saturation at 50% porosity, with hydrates located in the pore space. The blue line is for the DEM model with completely disordered building blocks with aspect ratio 1/20 for the clay platelets and pores. The green line is the DEM model with spherical components. The red line is for the three phase effective medium theory. The quartz fraction is 25%.

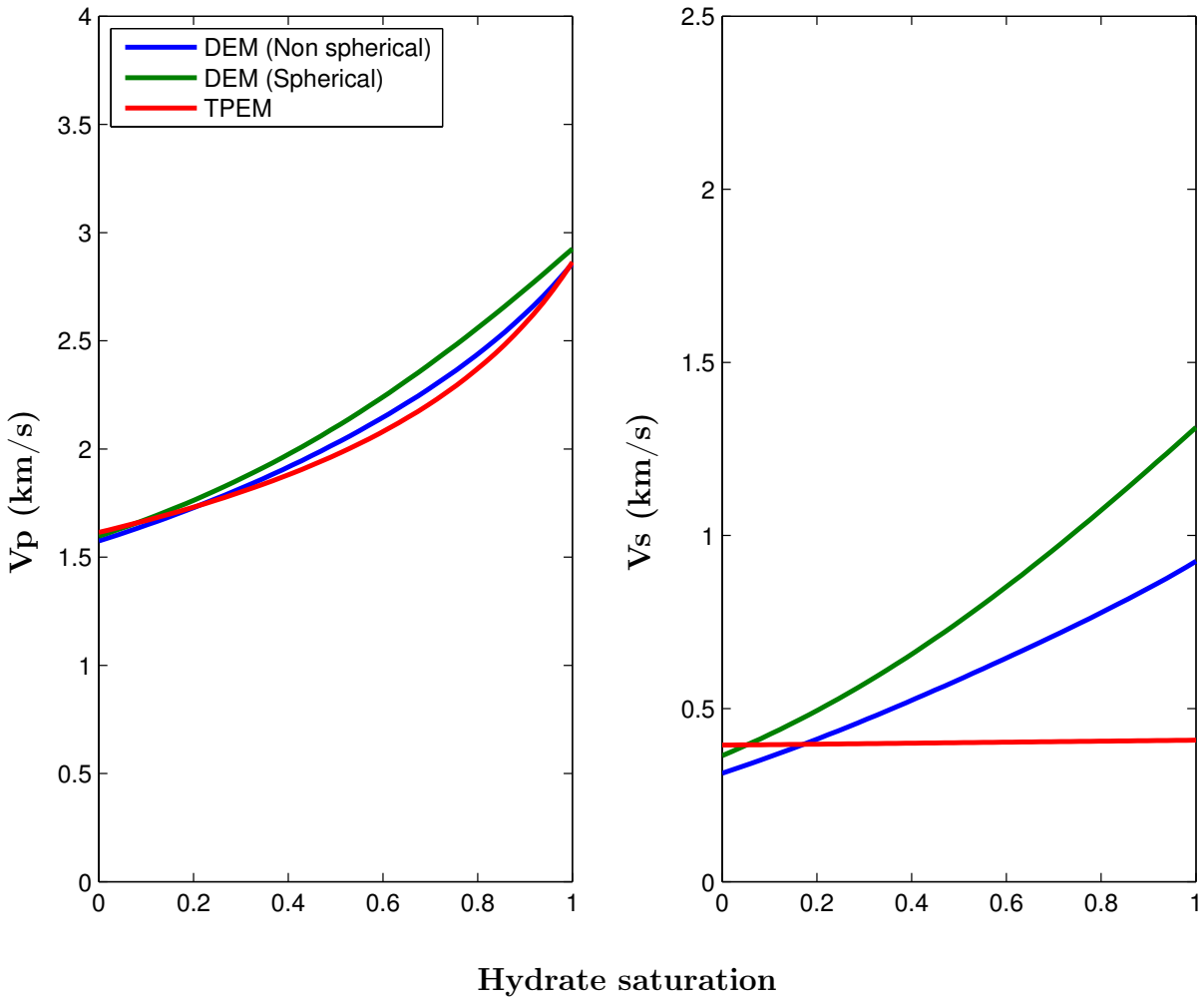

Figure 1.11: V_P and V_S plotted as a function of hydrate saturation at 75% porosity, with hydrates located in the pore space. The blue line is for the DEM model with completely disordered building blocks with aspect ratio 1/20 for the clay platelets and pores. The green line is the DEM model with spherical components. The red line is for the three phase effective medium theory. The quartz fraction is 25%.

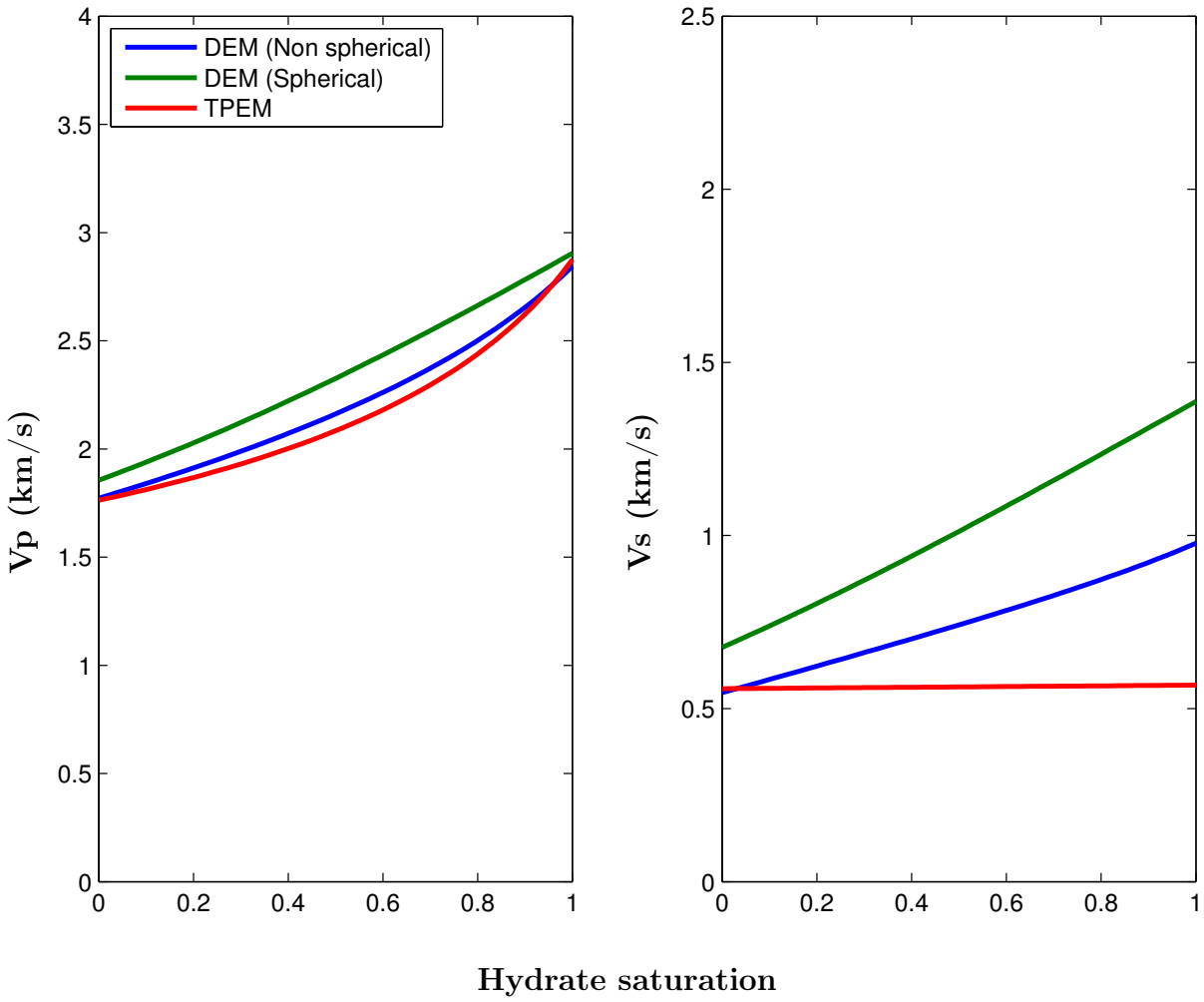

Figure 1.12: V_P and V_S plotted as a function of hydrate saturation with 20% quartz fraction, with hydrates located in the pore space. The blue line is for the DEM model with completely disordered building blocks with aspect ratio 1/20 for the clay platelets and pores. The green line is the DEM model with spherical components. The red line is for the three phase effective medium theory. The porosity is 60%.

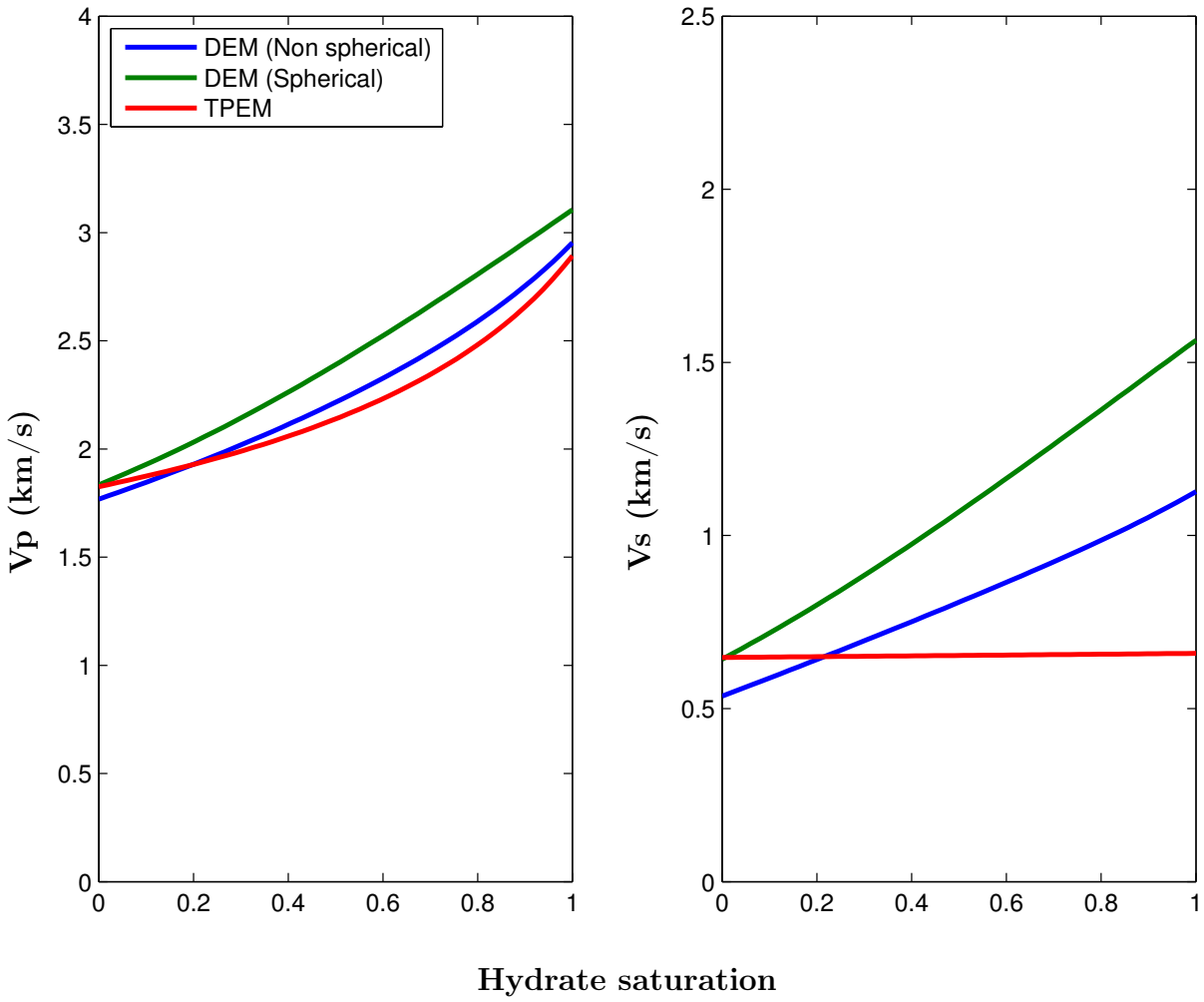

Figure 1.13: V_P and V_S plotted as a function of hydrate saturation with 50% quartz fraction, with hydrates located in the pore space. The blue line is for the DEM model with completely disordered building blocks with aspect ratio 1/20 for the clay platelets and pores. The green line is the DEM model with spherical components. The red line is for the three phase effective medium theory. The porosity is 60%.

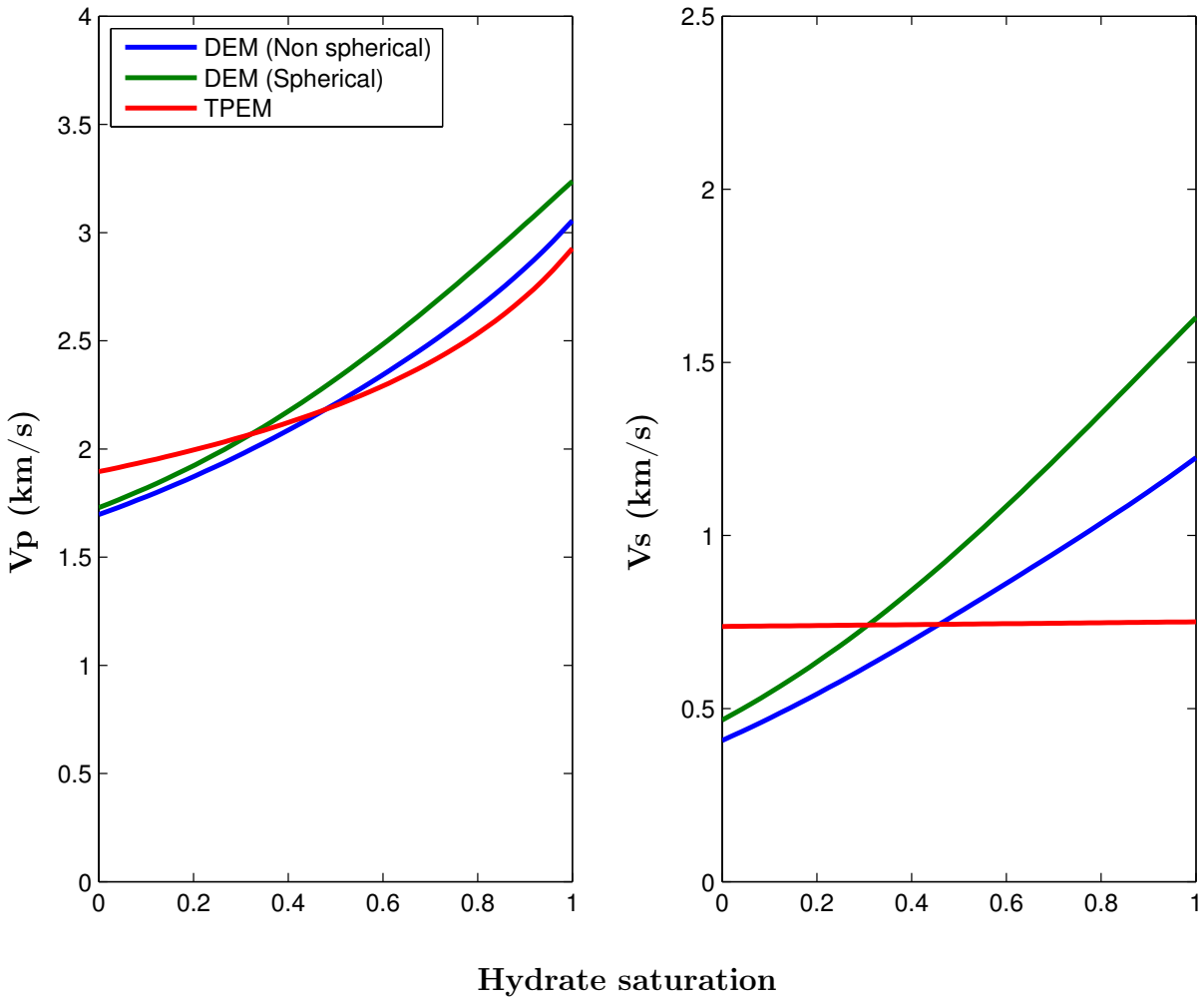

Figure 1.14: V_P and V_S plotted as a function of hydrate saturation with 80% quartz fraction, with hydrates located in the pore space. The blue line is for the DEM model with completely disordered building blocks with aspect ratio 1/20 for the clay platelets and pores. The green line is the DEM model with spherical components. The red line is for the three phase effective medium theory. The porosity is 60%.

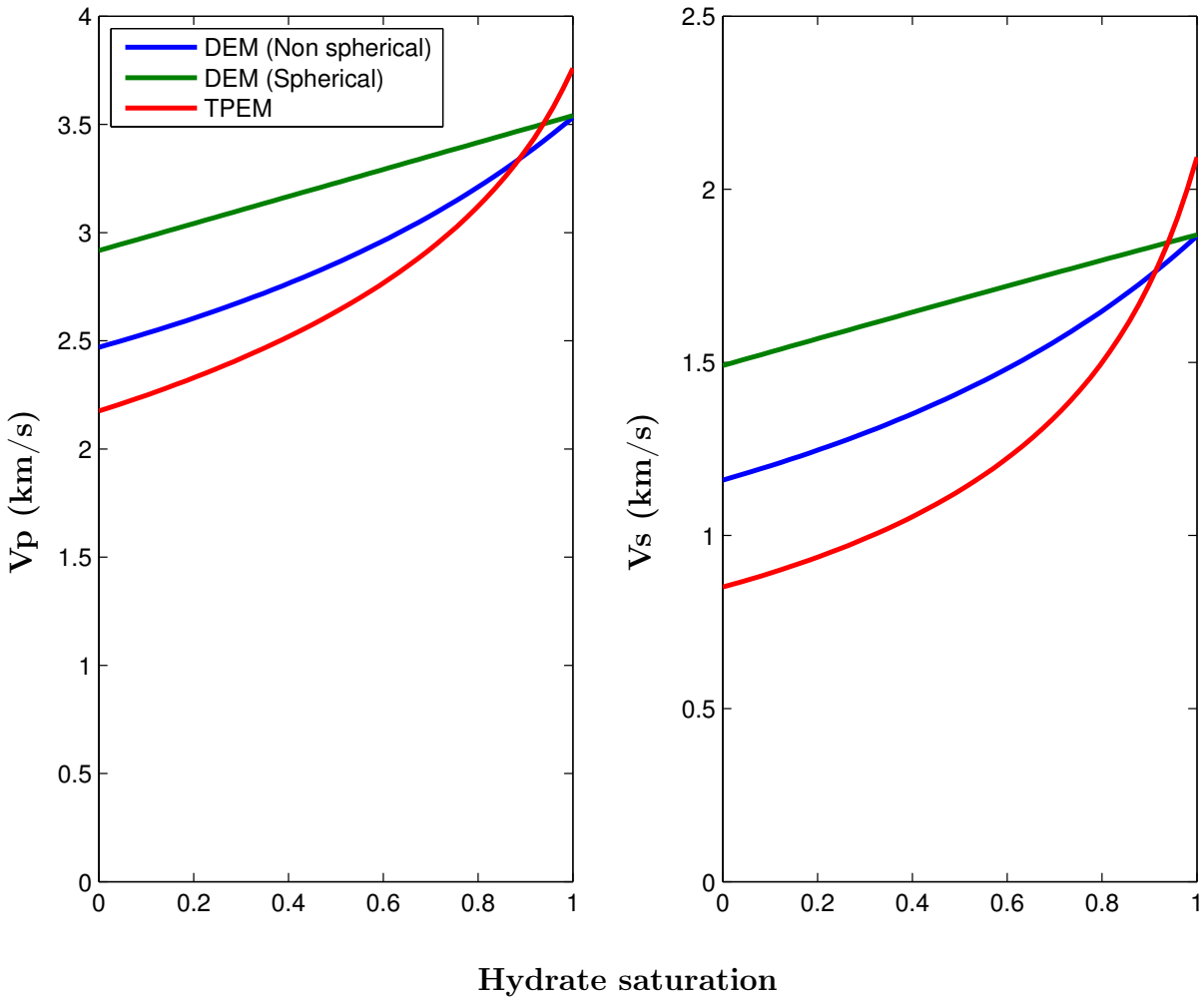

Figure 1.15: V_P and V_S plotted as a function of hydrate saturation at 25% porosity, with hydrates as part of the solid frame. The blue line is for the DEM model with completely disordered building blocks with aspect ratio 1/20 for the clay platelets and pores. The green line is the DEM model with spherical components. The red line is for the three phase effective medium theory. The quartz fraction is 25%.

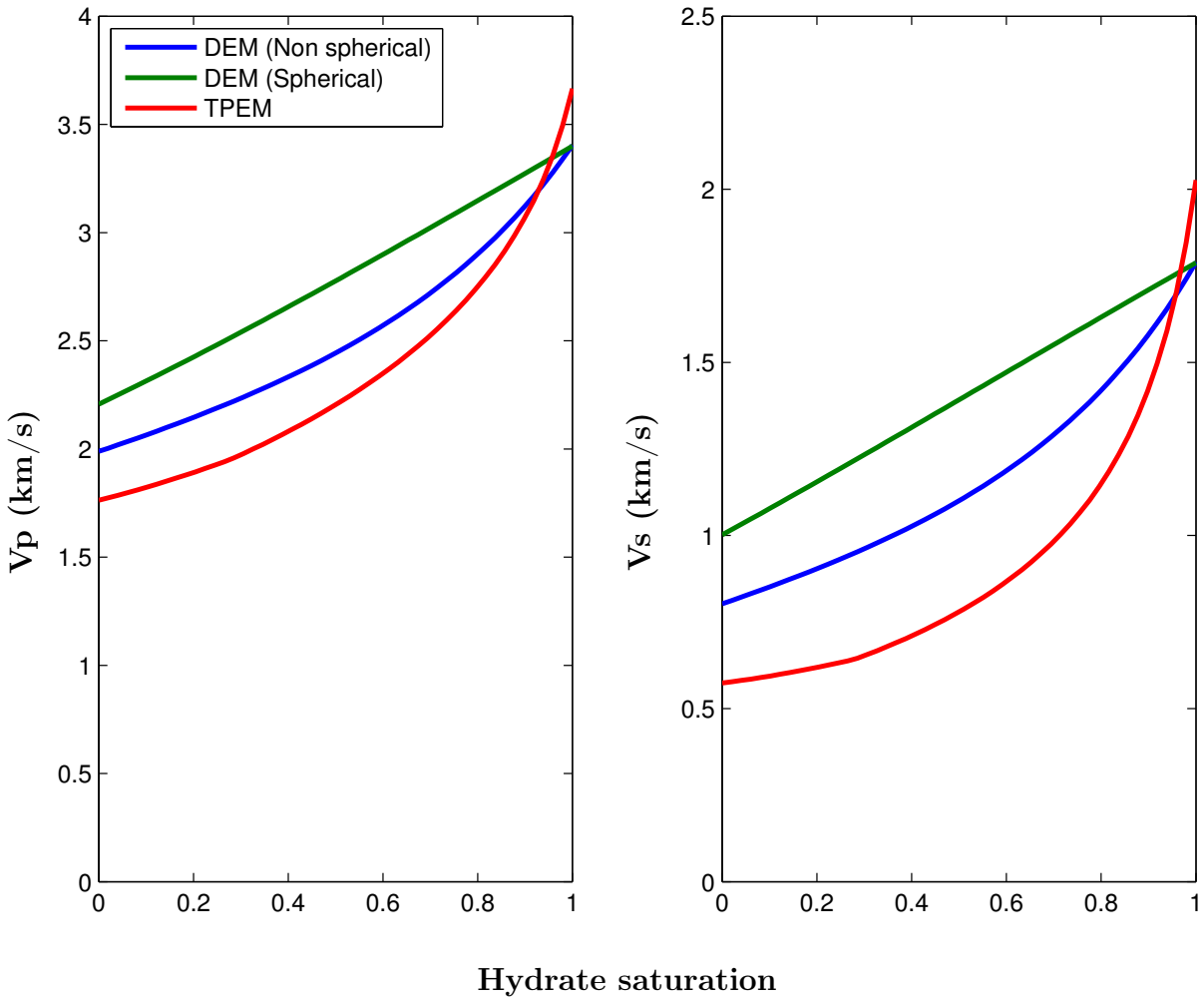

Figure 1.16: V_P and V_S plotted as a function of hydrate saturation at 50% porosity, with hydrates as part of the solid frame. The blue line is for the DEM model with completely disordered building blocks with aspect ratio 1/20 for the clay platelets and pores. The green line is the DEM model with spherical components. The red line is for the three phase effective medium theory. The quartz fraction is 25%.

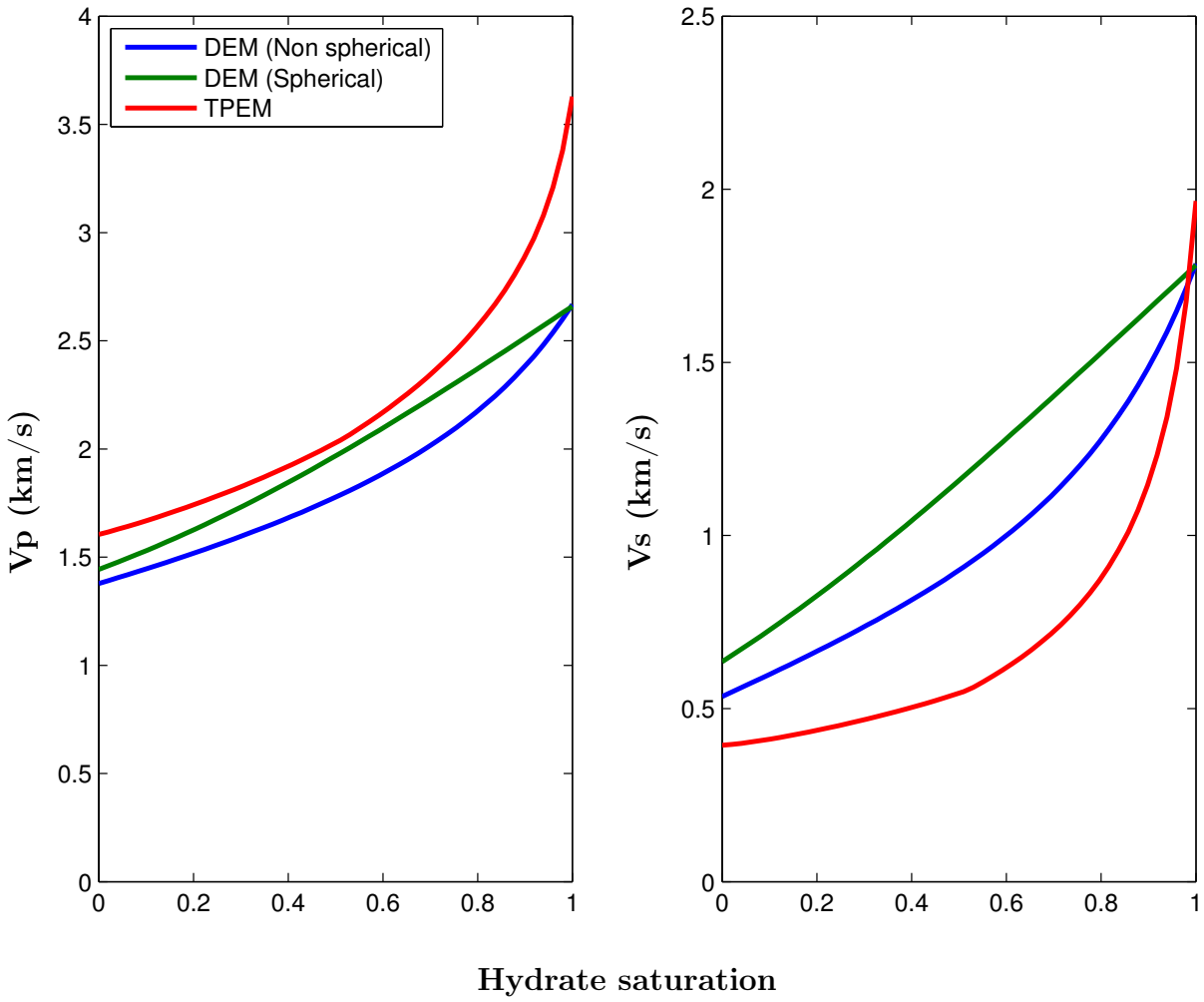

Figure 1.17: V_P and V_S plotted as a function of hydrate saturation at 75% porosity, with hydrates as part of the solid frame. The blue line is for the DEM model with completely disordered building blocks with aspect ratio 1/20 for the clay platelets and pores. The green line is the DEM model with spherical components. The red line is for the three phase effective medium theory. The quartz fraction is 25%.

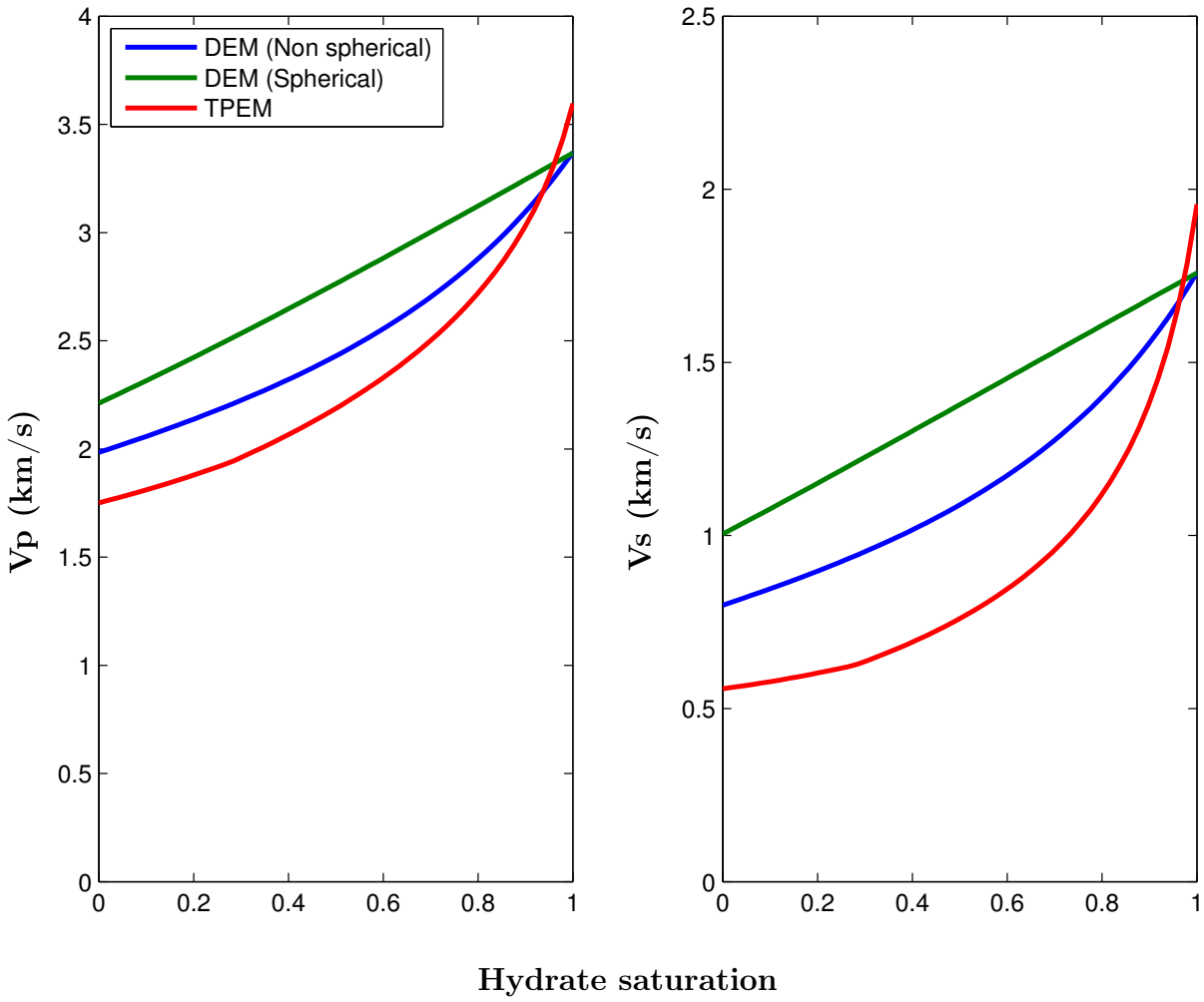

Figure 1.18: V_P and V_S plotted as a function of hydrate saturation with 20% quartz fraction, with hydrates as part of the solid frame. The blue line is for the DEM model with completely disordered building blocks with aspect ratio 1/20 for the clay platelets and pores. The green line is the DEM model with spherical components. The red line is for the three phase effective medium theory. The porosity is 60%.

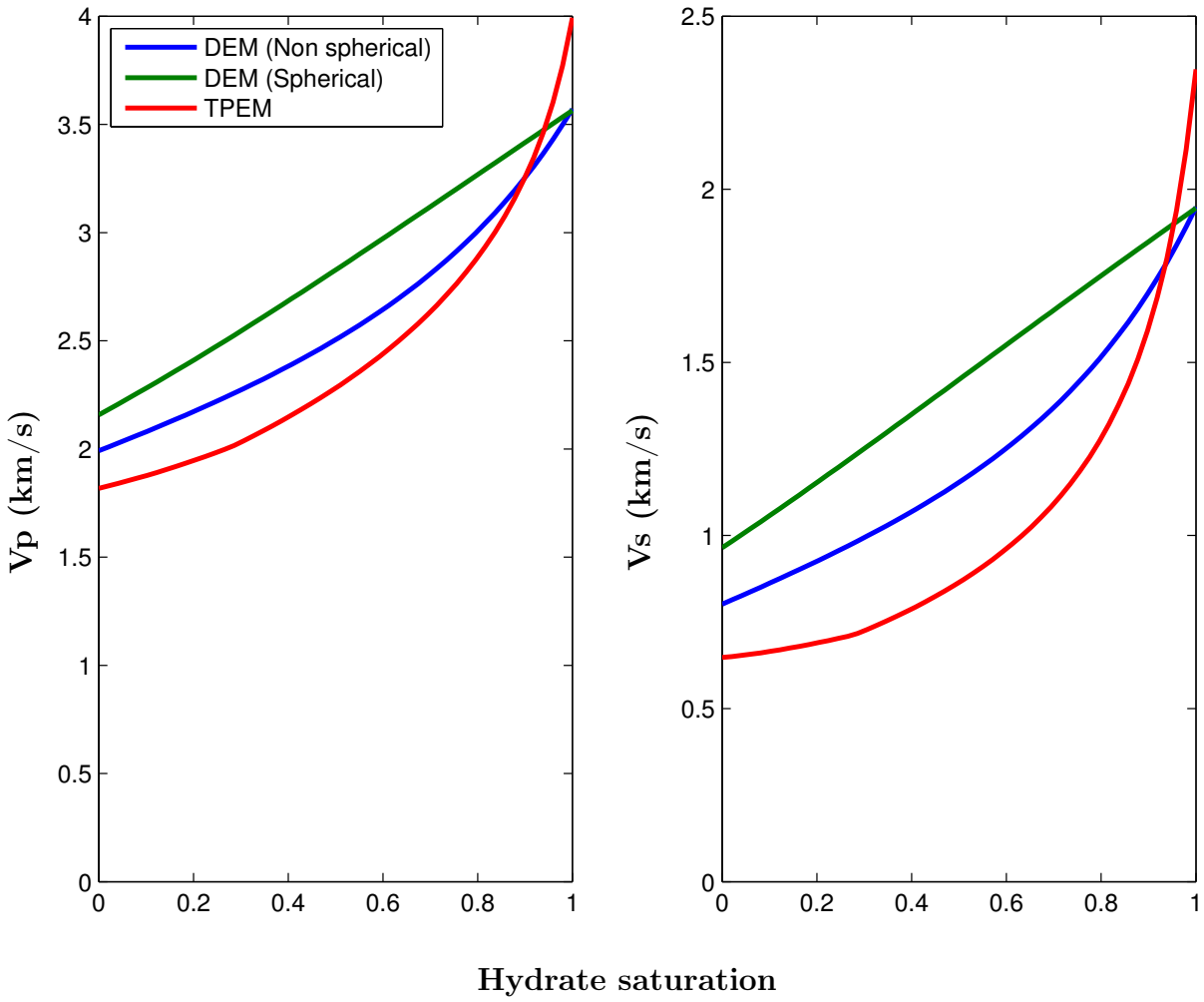

Figure 1.19: V_P and V_S plotted as a function of hydrate saturation with 50% quartz fraction, with hydrates as part of the solid frame. The blue line is for the DEM model with completely disordered building blocks with aspect ratio 1/20 for the clay platelets and pores. The green line is the DEM model with spherical components. The red line is for the three phase effective medium theory. The porosity is 60%.

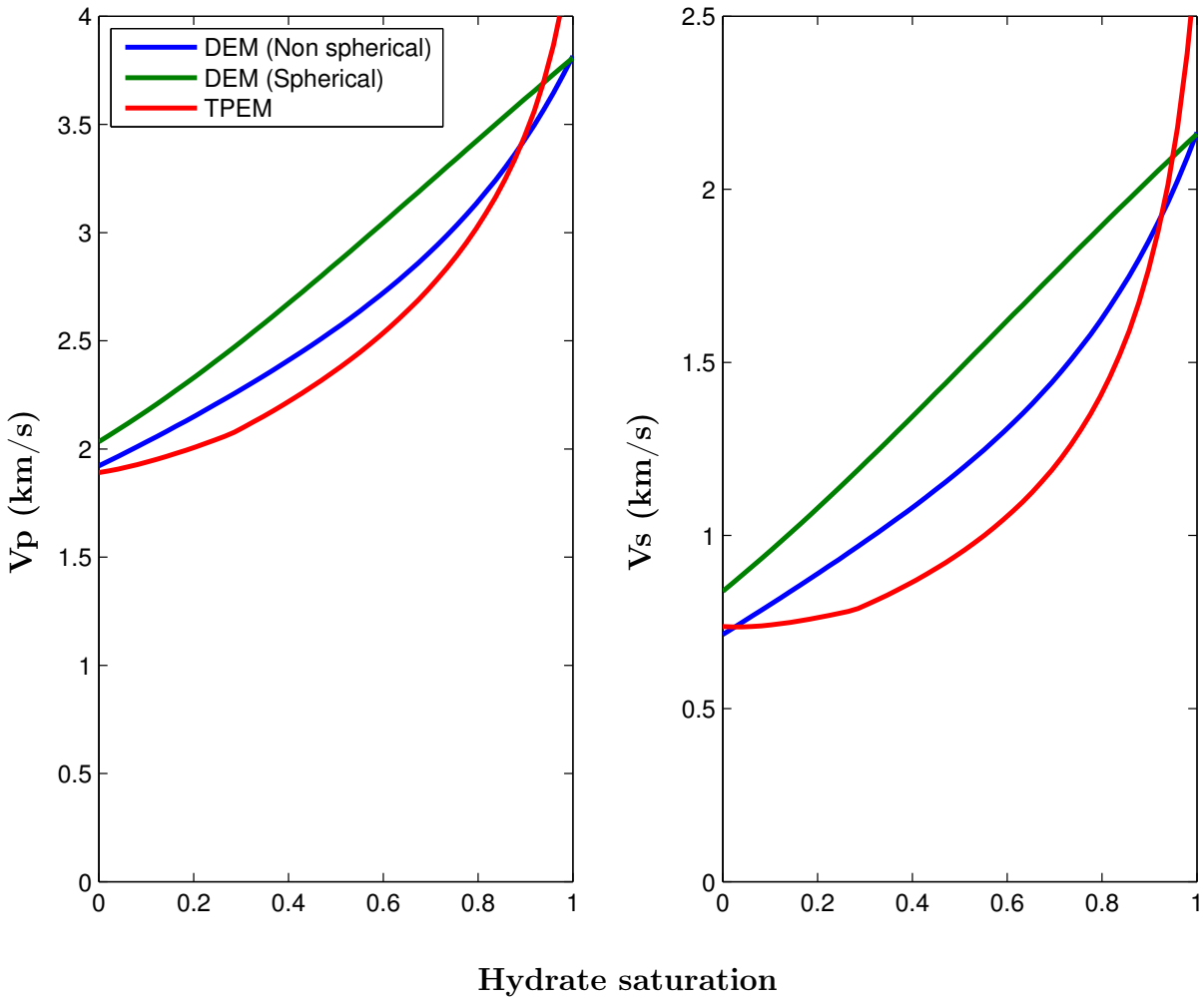

Figure 1.20: V_P and V_S plotted as a function of hydrate saturation with 80% quartz fraction, with hydrates as part of the solid frame. The blue line is for the DEM model with completely disordered building blocks with aspect ratio 1/20 for the clay platelets and pores. The green line is the DEM model with spherical components. The red line is for the three phase effective medium theory. The porosity is 60%.

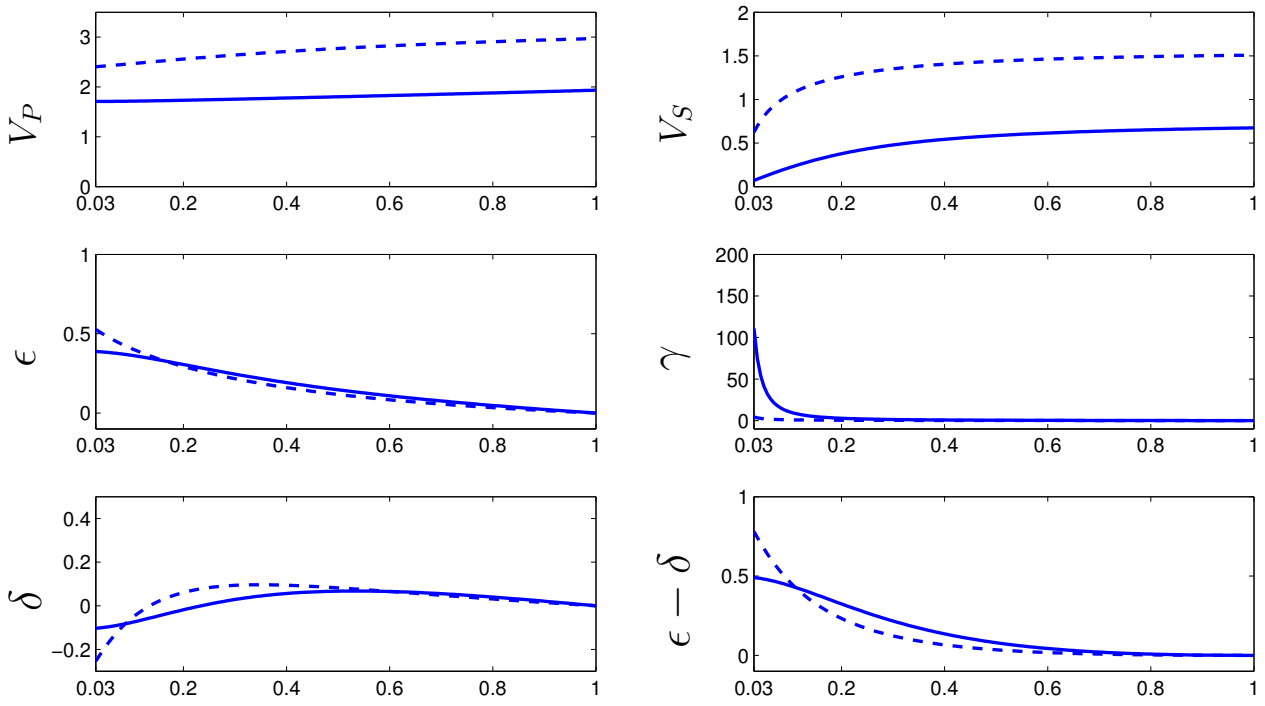

Figure 1.21: The anistotropy parameters for a fully aligned composite plotted as a function of the aspect ratio of the components. The solid lines are for 25% hydrates in the pores pace and the dashed lines are for 75% hydrates as grain coating. The porosity is 65% and the quartz content is 25%.

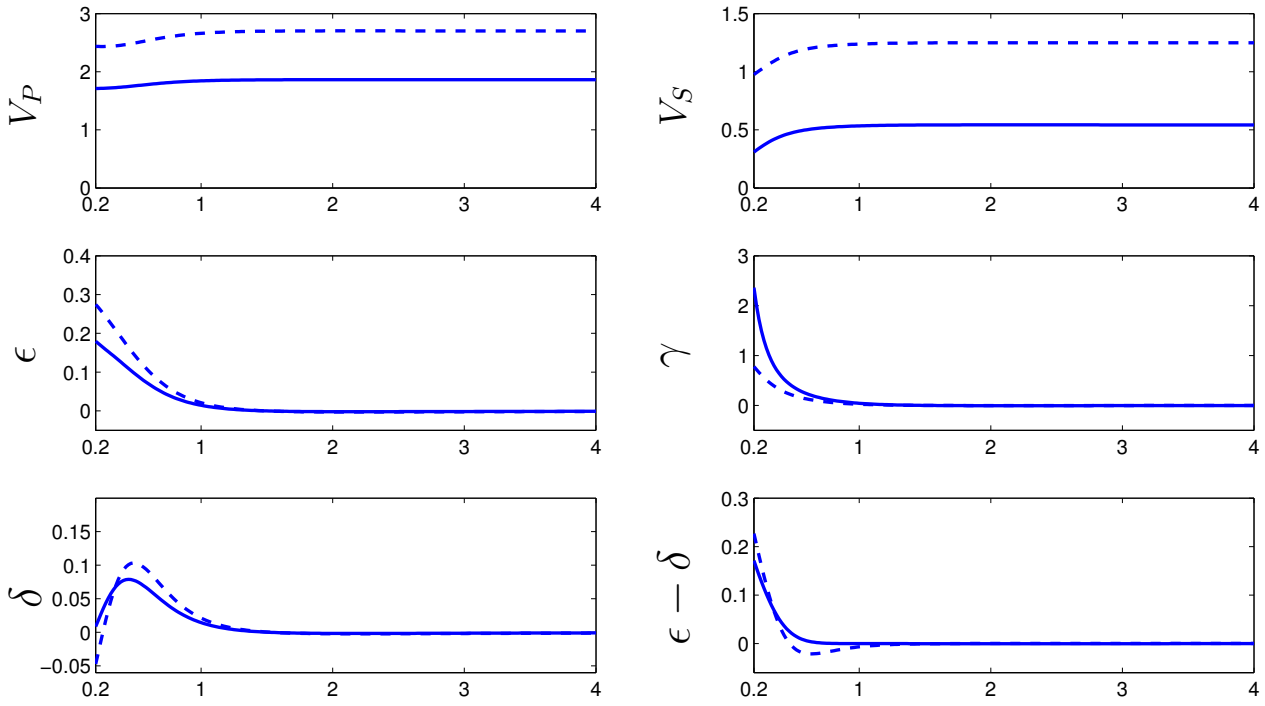

Figure 1.22: The anistotropy parameters plotted as a function of the standard deviation of the orientation distribution function. The solid lines are for 25% hydrates in the pores pace and the dashed lines are for 75% hydrates as grain coating. The porosity is 65%, the quartz content is 25% and the aspect ratio for the clay platelets and pores is 1/20.

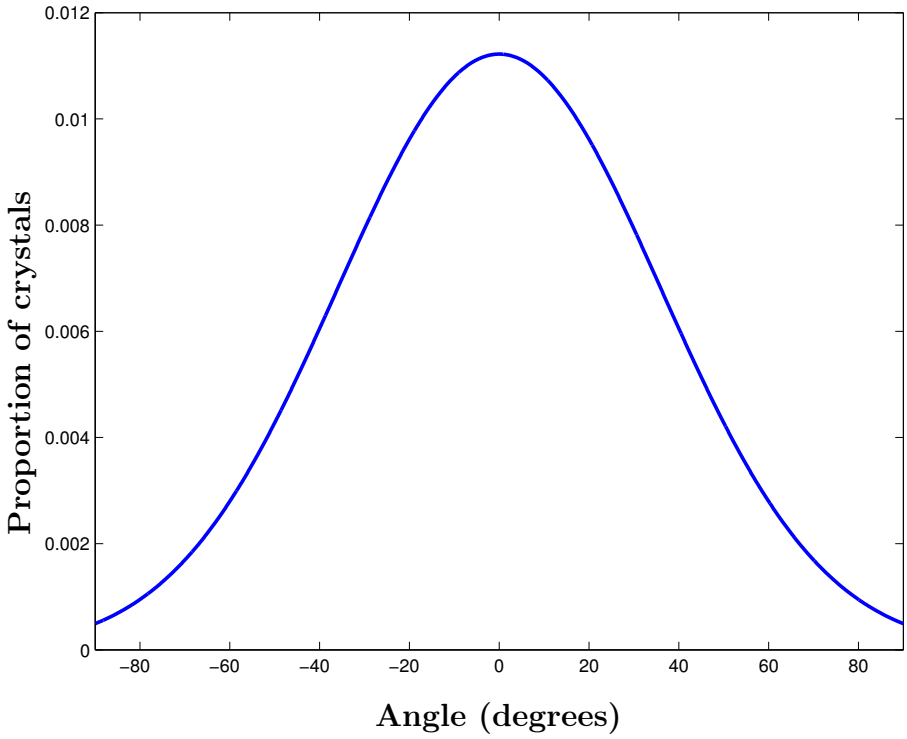

Figure 1.23: Orientation distribution for the building blocks used in the partially aligned case.

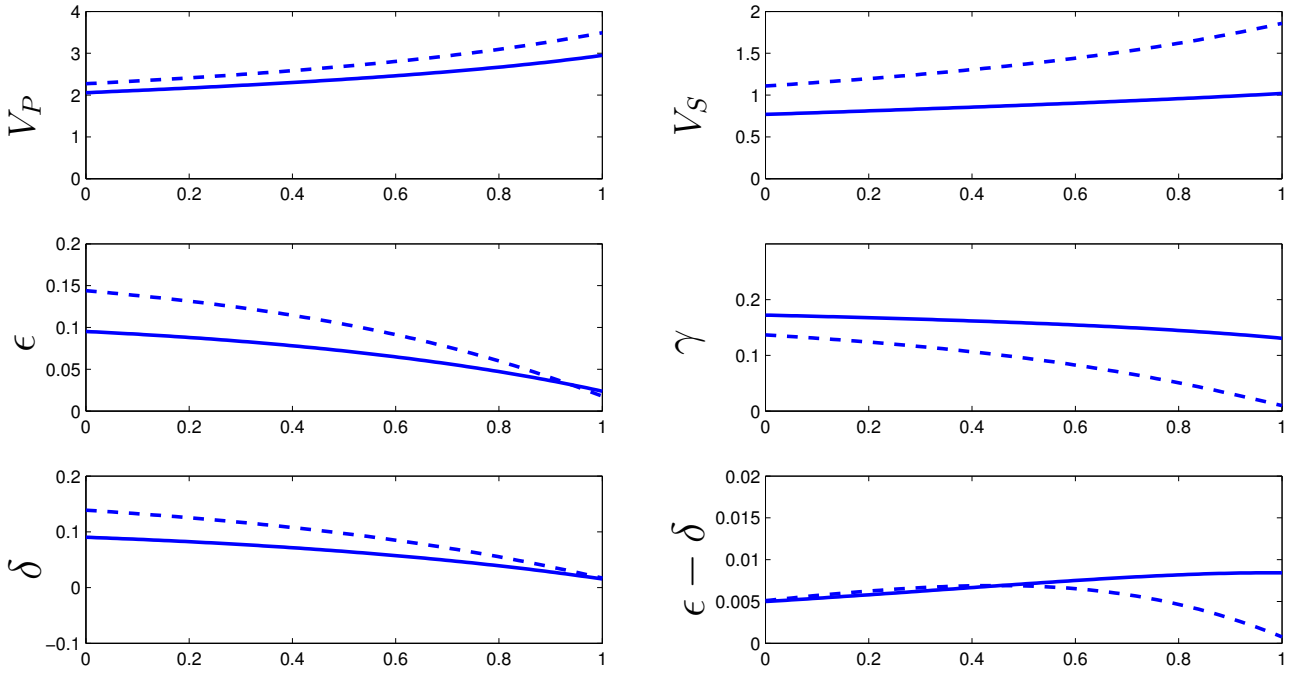

Figure 1.24: The anistotropy parameters plotted as a function of hydrate saturation for 25% porosity. The solid lines are for hydrates in the pore space and the dashed lines are for hydrates as grain coating. The quartz content is 25% and the aspect ratio is 1/20. The building blocks are orientated according to the distribution in figure 1.23.

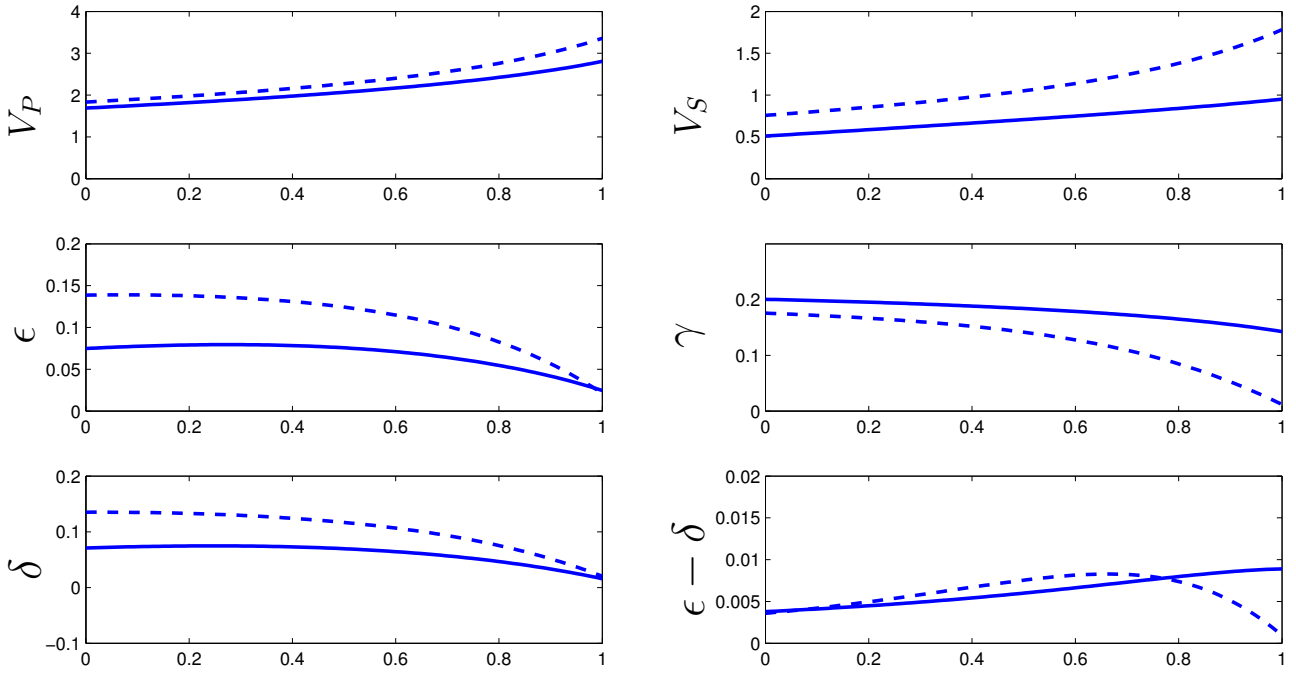

Figure 1.25: The anistotropy parameters plotted as a function of hydrate saturation for 50% porosity. The solid lines are for hydrates in the pore space and the dashed lines are for hydrates as grain coating. The quartz content is 25% and the aspect ratio is 1/20. The building blocks are orientated according to the distribution in figure 1.23.

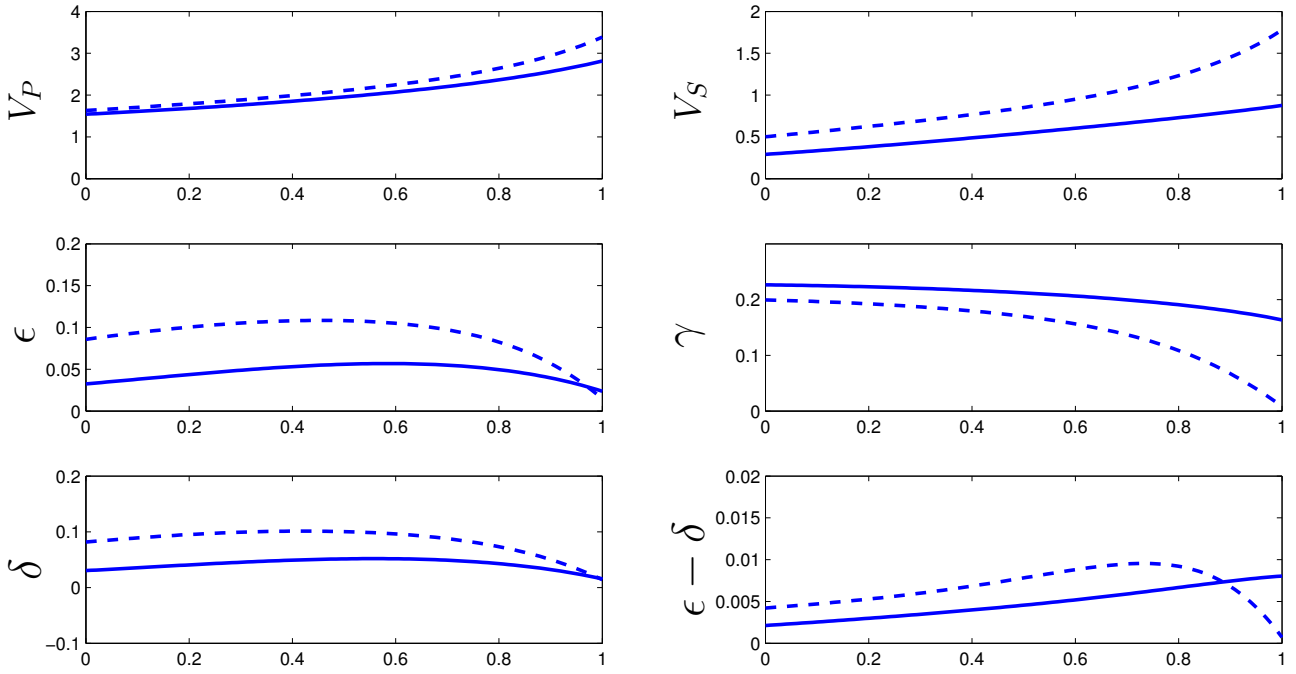

Figure 1.26: The anistotropy parameters plotted as a function of hydrate saturation for 75% porosity. The solid lines are for hydrates in the pore space and the dashed lines are for hydrates as grain coating. The quartz content is 25% and the aspect ratio is 1/20. The building blocks are orientated according to the distribution in figure 1.23.

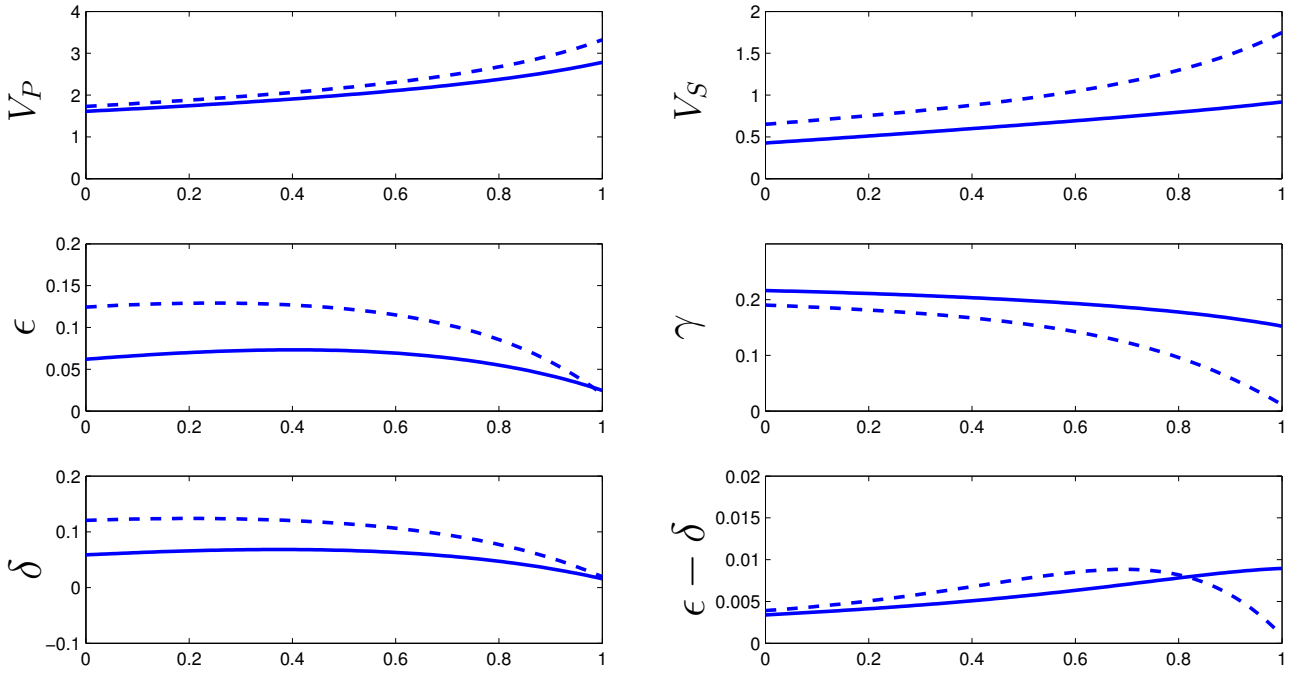

Figure 1.27: The anistotropy parameters plotted as a function of hydrate saturation for 20% quartz content. The solid lines are for hydrates in the pore space and the dashed lines are for hydrates as grain coating. The porosity is 60% and the aspect ratio is 1/20. The building blocks are orientated according to the distribution in figure 1.23.

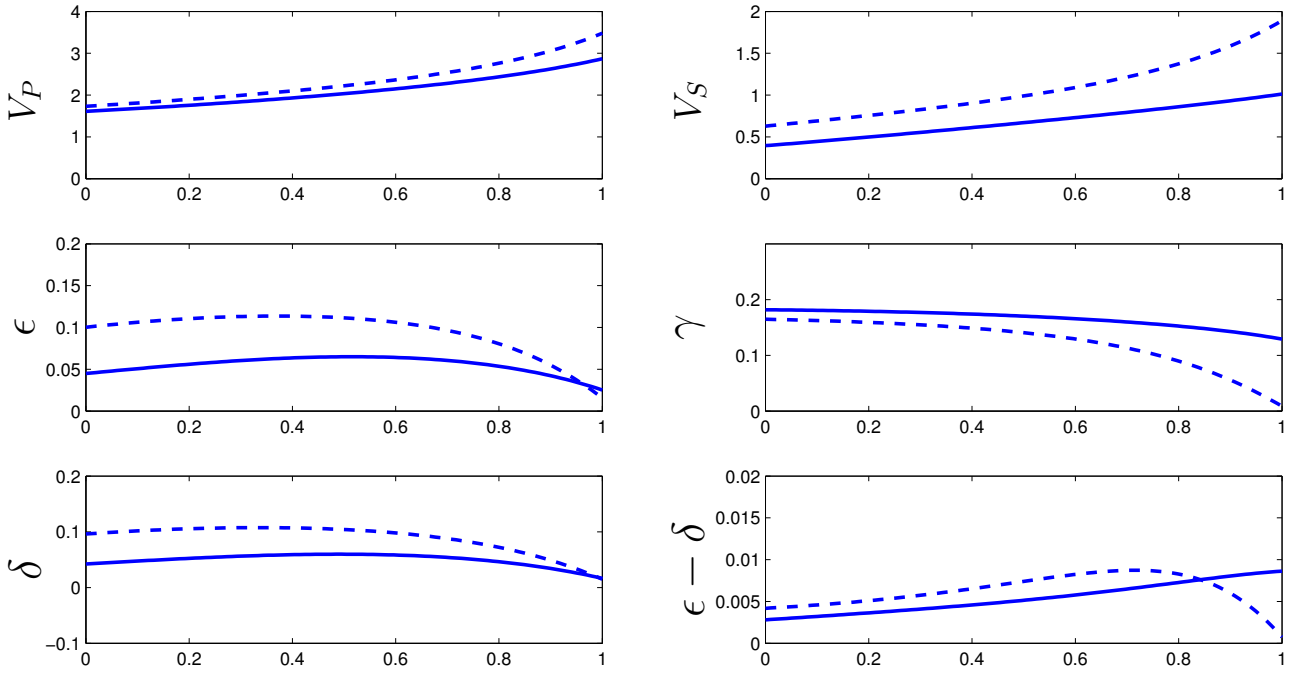

Figure 1.28: The anistotropy parameters plotted as a function of hydrate saturation for 50% quartz content. The solid lines are for hydrates in the pore space and the dashed lines are for hydrates as grain coating. The porosity is 60% and the aspect ratio is 1/20. The building blocks are orientated according to the distribution in figure 1.23.

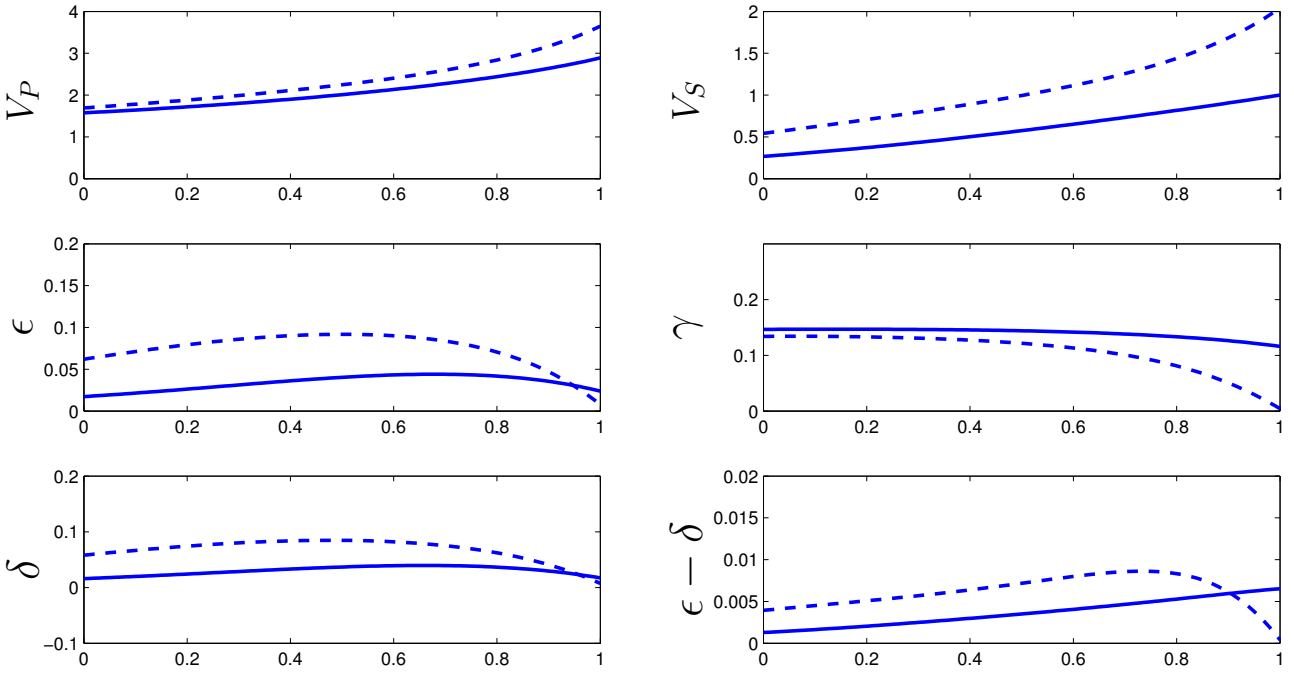

Figure 1.29: The anistotropy parameters plotted as a function of hydrate saturation for 80% quartz content. The solid lines are for hydrates in the pore space and the dashed lines are for hydrates as grain coating. The porosity is 60% and the aspect ratio is 1/20. The building blocks are orientated according to the distribution in figure 1.23.

Chapter 2

EFFECTS OF GAS HYDRATES ON SEISMIC AVO DATA

2.1 Introduction

In the previous chapter the relationship between hydrate saturation, elastic properties and seismic velocities was investigated. The next step is modeling the impact these effects have on seismic AVO data. Reflectivity properties will be modeled using Aki-Richard's and Rüger's approximations and compute synthetic seismograms for a horisontally layered model with a hydrated layer. The effect of hydrate saturation on the reflectivity properties will be investigated together with the effect of the presence of gas bellow the BSR.

2.2 The Aki-Richard approximation

When a plane wave hits an interface between two media with different seismic properties, boundary conditions that must be met at the interface that can not be satisfied by the incident wave alone. It is then necessary to include a certain amount of reflected and transmitted waves. In the case of a normal incident P-wave, only a reflected and refracted P-wave will be present. When we have a P-wave incident at an angle θ_i the situation is more complicated. There will then be a reflected and transmitted P- and S-wave. The amplitude relation between these waves can be derived from the elastic wave equation and boundary conditions at the interface to obtain what is known as the Zoeppritz (1919) equations.

The full Zoeppritz equations are complicated to solve and provide little physical insight. The well known approximation by Aki and Richards (1980) can therefore be useful for analysis of P-wave reflections. Assuming low incident angle (less than $40\,^\circ$) and weak layer contrast, the P-wave reflection coefficient R_{PP} at incident angle θ_i can be written (Mavko et al., 2009) In the case of an interface between two isotropic layers, the well known approximation by Aki and Richards (1980) can be used to calculate the P-wave reflection coefficient. Assuming low incident angle (less than $40\,^\circ$) and weak layer contrast, the P-wave R_{PP} at incident angle θ_i

can be written (Mavko et al., 2009)

$$R_{PP}(\theta) \approx \frac{1}{2}\left(\frac{\Delta V_P}{\overline{V}_P} + \frac{\Delta\rho}{\overline{\rho}}\right) + \left[\frac{1}{2}\frac{\Delta V_P}{\overline{V}_P} - 2\frac{\overline{V}_S^2}{\overline{V}_P^2}\left(2\frac{\Delta V_S}{\overline{V}_S} + \frac{\Delta\rho}{\overline{\rho}}\right)\right]\sin^2\theta + \frac{1}{2}\frac{\Delta V_P}{\overline{V}_P}\left(\tan^2\theta - \sin^2\theta\right), \tag{2.1}$$

where

$$\overline{V}_P = \frac{1}{2}(V_{P1} + V_{P2}) \qquad \Delta V_P = V_{P2} - V_{P1}$$
$$\overline{V}_S = \frac{1}{2}(V_{S1} + V_{S2}) \qquad \Delta V_S = V_{S2} - V_{S1}$$
$$\overline{\rho} = \frac{1}{2}(\rho_1 + \rho_2) \qquad \Delta\rho = \rho_2 - \rho_1$$
$$\theta = \frac{1}{2}(\theta_i + \theta_2) \approx \theta_i.$$

2.3 Rüger's approximation for VTI media

The full Zoeppritz equations were generalized to anisotropy by Schoenberg and Protazio (1992), and can be used to calculate the reflection coefficients for an interface between two anisotropic layers. But same as in the isotropic case, these are complicated to solve and provide little physical insight. In the case of a weakly anisotropic VTI media with small layer contrast Rüger's (Rüger, 1997) approximation can therefore be usefull for calculating the P-wave reflection coefficient (Mavko et al., 2009):

$$R_{PP}(\theta) = R_{PP-iso}(\theta) + R_{PP-aniso}(\theta)$$
$$R_{PP-iso}(\theta) \approx \frac{1}{2}\left(\frac{\Delta Z}{\overline{Z}}\right) + \frac{1}{2}\left[\frac{\Delta V_P}{\overline{V}_P} - \left(\frac{2\overline{V}_S}{\overline{V}_P}\right)\frac{\Delta\mu}{\overline{\mu}}\right]\sin^2\theta \tag{2.2}$$
$$R_{PP-aniso}(\theta) \approx \frac{\Delta\delta}{2}\sin^2\theta + \frac{\Delta\epsilon}{2}\sin^2\theta\tan^2\theta$$

where

$$\overline{Z} = (Z_1 + Z_2)/2 \qquad \Delta Z = Z_2 - Z_1$$
$$\overline{\epsilon} = (\epsilon_1 + \epsilon_2)/2 \qquad \Delta\epsilon = \epsilon_2 - \epsilon_1$$
$$\overline{\delta} = (\delta_1 + \delta_2)/2 \qquad \Delta\delta = \delta_2 - \delta_1$$
$$\theta = (\theta_1 + \theta_2)/2 \approx \theta_i.$$

θ is the P-wave phase angle of incidence, $Z = \rho V_P$ is the vertical P-wave impedance and $\mu = \rho V_S$ is the vertical shear modulus. V_P and V_S are in this case the vertical P- and S-wave velocities.

2.4 Seismic modeling of a layered media

In order to investigate the effect of hydrates on seismic data, it can be useful to generate synthetic seismograms for a geological model consisting of a layer containing hydrates. This is

done by finding a numerical solution for the equation of motion. Ray theory is a well known method, where high frequency is assumed so that the travel time along a ray path can be computed from the eikonal equation (Krebes, 2004):

$$(\nabla T)^2 = \left(\frac{\partial T}{\partial x}\right)^2 + \left(\frac{\partial T}{\partial y}\right)^2 + \left(\frac{\partial T}{\partial z}\right)^2 = \frac{1}{V^2}, \tag{2.3}$$

where $v = v(\mathbf{x})$ is the wave speed at the point $\mathbf{x}$.

In the case of a horizontally layered homogeneous media, the travel time can be computed from some simple algebraic formulas. First the desired source-receiver offset X is chosen. The ray parameter p is then calculated from the equation (Krebes, 2004):

$$X = \sum_{j=1}^{m} \frac{pV_j h_j}{\sqrt{1 - p^2 V_j^2}}, \tag{2.4}$$

where m , V_j and h_j are the is the number of ray segments, wave speed and thickness, respectively, along the ray path. It should be noted that in the case of anisotropy, V_j is dependent on the propagation direction of the ray segment. The ray parameter is simply the horizontal component of the slowness vector $p = \sin\theta_j / V_j$, and Snell's law states that this is constant along the ray path. Next step is to calculate the travel time from source to receiver, given by (Krebes, 2004):

$$T = \sum_{j=1}^{m} \frac{h_j}{V_j \sqrt{1 - p^2 V_j^2}}. \tag{2.5}$$

For an anisotropic layer, since the slowness vector is dependent on propagation direction, an analytic statement of snell's law is hard to obtain. The scattering angles can, however, be obtained graphically from the slowness surface. The slowness of a plane wave propagating along the direction $\hat{\mathbf{l}}$, can be obtained by solving the Christoffel equation (Auld, 1973):

$$k^2 \mathbf{\Gamma u} = \rho\omega^2 \mathbf{u}, \tag{2.6}$$

where

$$\mathbf{\Gamma} = \mathbf{LCL}^T \tag{2.7}$$

is the Christoffel matrix and the matrix $\mathbf{L}$ is given by:

$$\mathbf{L} = \begin{bmatrix} l_x & 0 & 0 & 0 & l_z & l_y \\ 0 & l_y & 0 & l_z & 0 & l_x \\ 0 & 0 & l_z & l_y & l_x & 0 \end{bmatrix} \tag{2.8}$$

Equation 2.6 is then solved for the slowness, which is the inverse of the phase velocity $k/\omega = 1/V_{phase}$, by setting the characteristic determinant equal to zero(Auld, 1973):

$$\det\left(\mathbf{\Gamma} - \rho V_{phase} \mathbf{I}\right) = 0 \tag{2.9}$$

The phase angle θ for the transmitted wave can then be calculated by finding the point on the slowness surface where the horizontal component is equal to that of the layer above, as shown

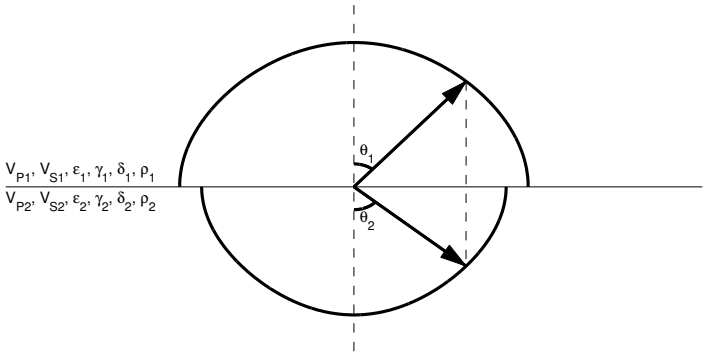

Figure 2.1: Schematic sketch showing P-wave scattering properties for a plane wave incident at a boundary between two anisotropic layers. The slowness surfaces shown are for layer 2 (top) and layer 3 case b (bottom).

in figure 2.1. Next step is to calculate the group angle φ, which for a weakly anisotropic media can be expressed in terms of the phase angle and anisotropy parameters by (Thomsen, 1986):

$$\tan\varphi = \tan\theta\left[1 + 2\delta + 4\left(\epsilon - \delta\right)\sin^2\theta\right] \tag{2.10}$$

Once the propagation direction of the ray segments is known, the corresponding group velocites can be calculated from (Thomsen, 1986):

$$V_{P_{group}}\left(\varphi\right) = V_{P_{phase}}\left(\theta\right) \tag{2.11}$$

Next, the vertical component of the inverse of the group velocity is found for each ray segment:

$$\frac{\sin\varphi}{V_{P_{phase}}\left(\varphi\right)} \tag{2.12}$$

V_j and p in 2.4 is then replaced by the group velocity and vertical component of the inverse of the group velocity, respectively, for each segment to obtain p corresponding to the chosen source-receiver offset, before the travel time is calculated from equation 2.5 following the same procedure.

Now that the travel times to the reflectors are known, a reflectivity series with the corresponding two way times can be produced. The reflection coefficients are determined from Aki-Richard's or Rüger's approximation. The seismograms can then be computed from a convolution between the reflectivity series and a source pulse series.

2.5 Numerical results and discussion

In order to investigate reflectivity properties of hydrated sediments, a layered model with a hydrated layer will be defined. In table 2.1 the properties of the layers are shown. The model has four different alternatives for hydrate saturation (5%, 25%, 75% and 95%), and the layer below the hydrates can be either completely brine saturated or contain 50% gas. It is assumed that the hydrates are present as pore filling at 5% and 25% saturation, and as part of the solid frame at 75% and 95%. In table 2.2 the calculated velocities for the isotropic models are shown,

and table 2.3 show the vertical velocities and anisotropy parameters for the anisotropic DEM model.

Figures 2.2-2.5 show the reflection coefficients for the top of the hydrated layer plotted as a function of angle using Aki-Richard's (isotropic) and Rüger's (anisotropic) approximation. The two isotropic DEM models (figure 2.2 and 2.3) show very similar reflectivity properties, with shallow dip when the hydrates are located in the pore space. When the hydrates are connected, we see a more sharply dipping curve as the saturation increases and a upward bend from around 25 degrees at 95% saturation. The TPEM model (figure 2.4) has a weakly dipping reflection coefficient at 5% saturation and weakly rising at 25% and at 50% when the hydrates are present as pore filling. The reflection coefficient is similar to the isotropic DEM models at 5% saturation and lower at 25% and 50%. Also when the hydrates form part of the solid frame, this model shows lower reflection coefficient at 50% saturation, that dips shallowly. At 75% saturation this model has a reflection coefficient that increases with angle, and is lower than for the isotropic DEM models at low offset, while it at 95% shows similar reflectivity properties as these models.

In figure 2.5 the reflection coefficients for the DEM model with partially aligned microstructure are shown. At 5% and 25% saturation, the reflection coefficients are flat and similar in value to the isotropic DEM models. At 50% saturation, when the hydrates are located in the pore space, the reflectivion coefficients are also similar to the isotropic DEM models, but slightly rising. When the hydrates are connected, the reflection coefficients dip shallowly up to $20 - 25$ degrees, before they start to increase. This increase is barely visible at 50% saturation, a bit stronger at 75% and very sharp at 95%.

Figures 2.6-2.13 show synthetic seismograms computed using the methods described in section 2.4. Geometrical spreading and multiples are not accounted for. The seismograms are noise free, and can be seen as corresponding to perfectly processed data. The seismograms for the different models look similar, but with lower velocities at small offsets and a slightly shallower dip from reflector 4 for the anisotropic DEM model when the layer below the hydrates contain 50% gas. This can be explained by the much lower vertical velocity and strong P-wave anisotropy of the gas layer. Generally, the reflectors at the top of the hydrate layer are weak when the hydrate saturation is low, and quite strong at higher saturation. At the bottom of the hydrate layer, when there is no gas bellow the hydrate layer, the reflection is barely visible and normal polarity at 5% saturation. At 25% it changes polarity, but is still barely visible. When the hydrate saturation is increased to 75% and 95% the reflection is strong and inversely polarized, showing the typical characteristics of a bottom simulating reflector. When gas is present bellow the hydrate layer, this reflector is strong and inversely polarized at all saturations.

2.6 Concluding remarks

In this chapter the rock physics models were applied to a layered model with a hydrated layer, and reflectivity properties were investigated and compared. We have seen that the reflectivity properties were quite similar at low saturations for the different models. The DEM model with spherical components and non-spherical completely disordered components showed similar reflection coefficients for all saturations. The TPEM model show similar properties as these model, except in the case of 75% saturation, where it has opposite AVA trend. The DEM model with partially aligned structure showed similar vertical reflection coefficients as the DEM with completely disordered structure at low offsets. The AVA trends were similar at low saturations, but showed large variations at higher saturations. In the next chapter these synthetic data will be used to analyze uncertainty in the estimate of the hydrate saturation and porosity, on the basis of data containing noise and the effect of the differences in the models have on the estimates will be analyzed.

Table 2.1: Properties of the layers. This model is similar to the one investigated by Jakobsen et al. (2001), but with constant quartz fraction f_q.

Layer	Alterative	Thickness (km)	ϕ	f_q	Description
1	-	3.27	1	0	Sea water
2	-	0.24	0.65	0.25	Sediments with brine
3	-	0.23	0.60	0.25	Sediments with hydrate/brine
	a				5% hydrate in pore space
	b				25% hydrate in pore space
	c				75% hydrate in pore space
	d				95% hydrate in pore space
4	-	0.18	0.55	0.25	Sediments with gas/brine
	a				50% gas in pore space
	b				Sediments with brine
5	-	-	0.5	0.25	Sediments with brine

Table 2.2: Calculated V_P and V_S for the layers with properties from table 2.1.

Layer	Alternative	DEM (non-spherical)		DEM (spherical)		TPEM		
		V_P	V_S	V_P	V_S	V_P	V_S	ρ
1	-	1.483	0	1.483	0	1.483	0	1.030
2	-	1.639	0.412	1.679	0.491	1.663	0.468	1.584
3	a	1.709	0.477	1.767	0.582	1.719	0.504	1.659
	b	1.866	0.571	1.954	0.726	1.834	0.506	1.644
	c	2.727	1.279	3.003	1.532	2.539	0.949	1.606
	d	3.219	1.646	3.306	1.726	3.235	1.563	1.584
4	a	1.001	0.522	0.882	0.442	1.022	0.596	1.529
	b	1.720	0.501	1.785	0.611	1.731	0.538	1.742
5	-	1.770	0.545	1.850	0.672	1.774	0.574	1.821

Table 2.3: Calculated vertical V_P and V_S, ϵ, γ and δ for the layers with properties from table 2.1, using the partially aligned microstructure for the DEM model. The aspect ratio is 1/20.

Layer	Alternative	V_P	V_S	ϵ	γ	δ	ρ
1	-	1.483	0	0	0	0	1.030
2	-	1.586	0.384	0.051	0.216	0.048	1.584
3	a	1.644	0.446	0.062	0.209	0.059	1.659
	b	1.786	0.534	0.070	0.204	0.065	1.644
	c	2.578	1.234	0.094	0.109	0.086	1.606
	d	3.138	1.625	0.041	0.037	0.037	1.584
4	a	0.829	0.485	0.348	0.219	0.401	1.529
	b	1.648	0.468	0.068	0.205	0.064	1.742
5	-	1.689	0.510	0.075	0.201	0.071	1.821

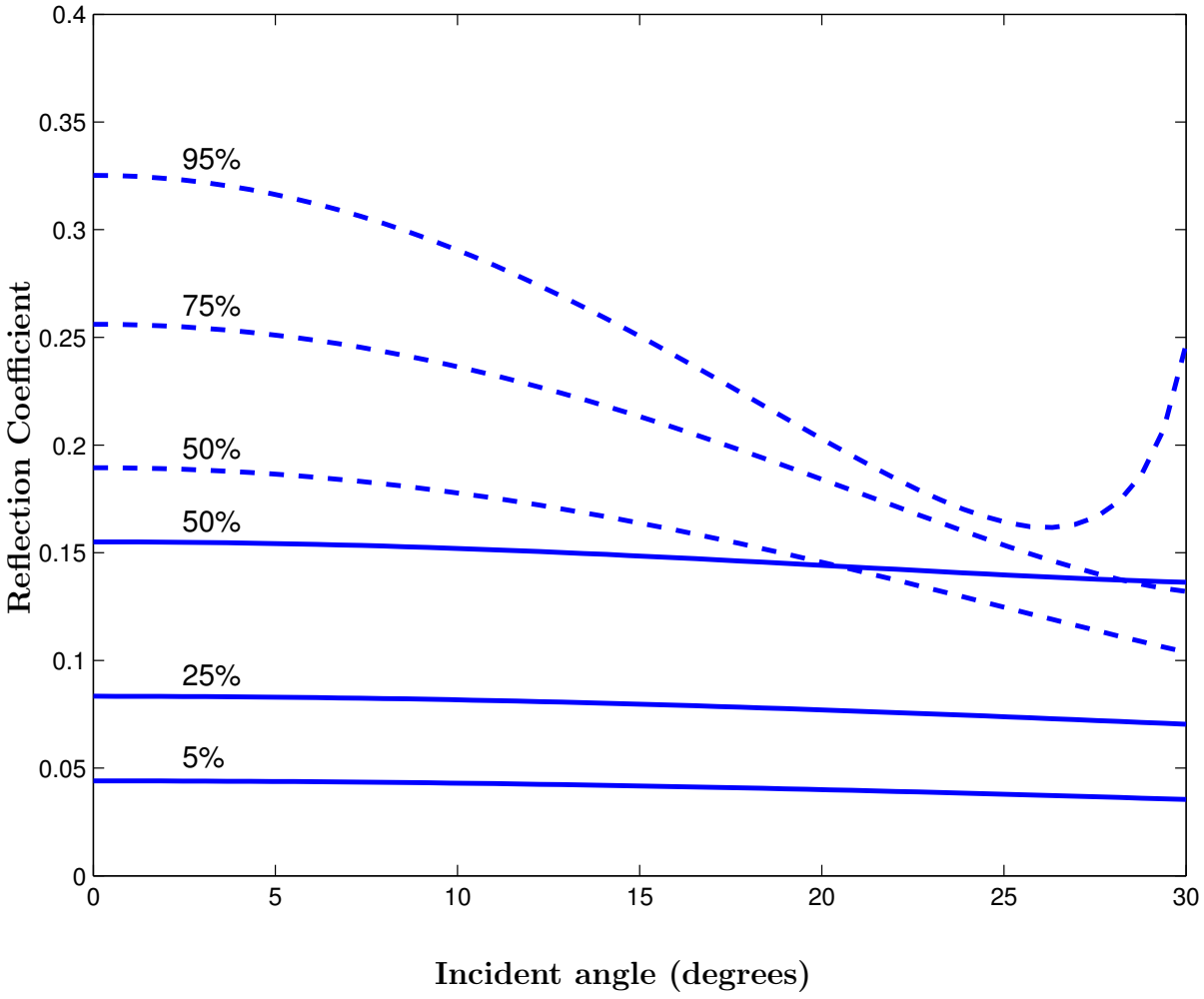

Figure 2.2: P-wave reflection coefficients R_{PP} for the top of the hydrate layer plotted as a function of incident angle for different hydrate saturation. The solid lines are for hydrates in the pore space and the dashed lines are for hydrates as part of the solid frame. The properties of the layers are given in table 2.1, and the model used is the DEM model with aspect ratio 1/20 for the grains and pores.

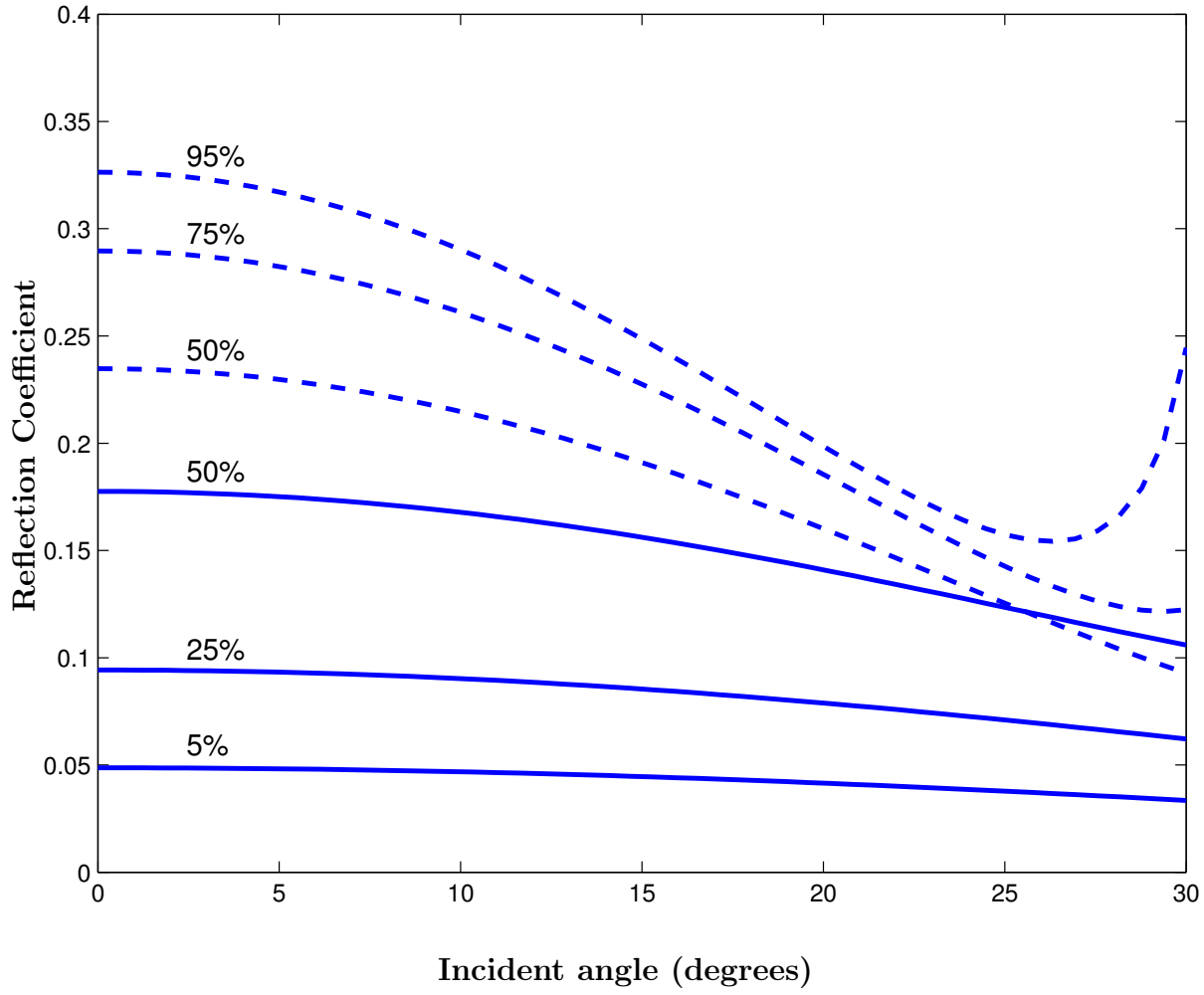

Figure 2.3: P-wave reflection coefficients R_{PP} for the top of the hydrate layer plotted as a function of incident angle for different hydrate saturation. The solid lines are for hydrates in the pore space and the dashed lines are for hydrates as part of the solid frame. The properties of the layers are given in table 2.1and the model used is the DEM model with spherical components.

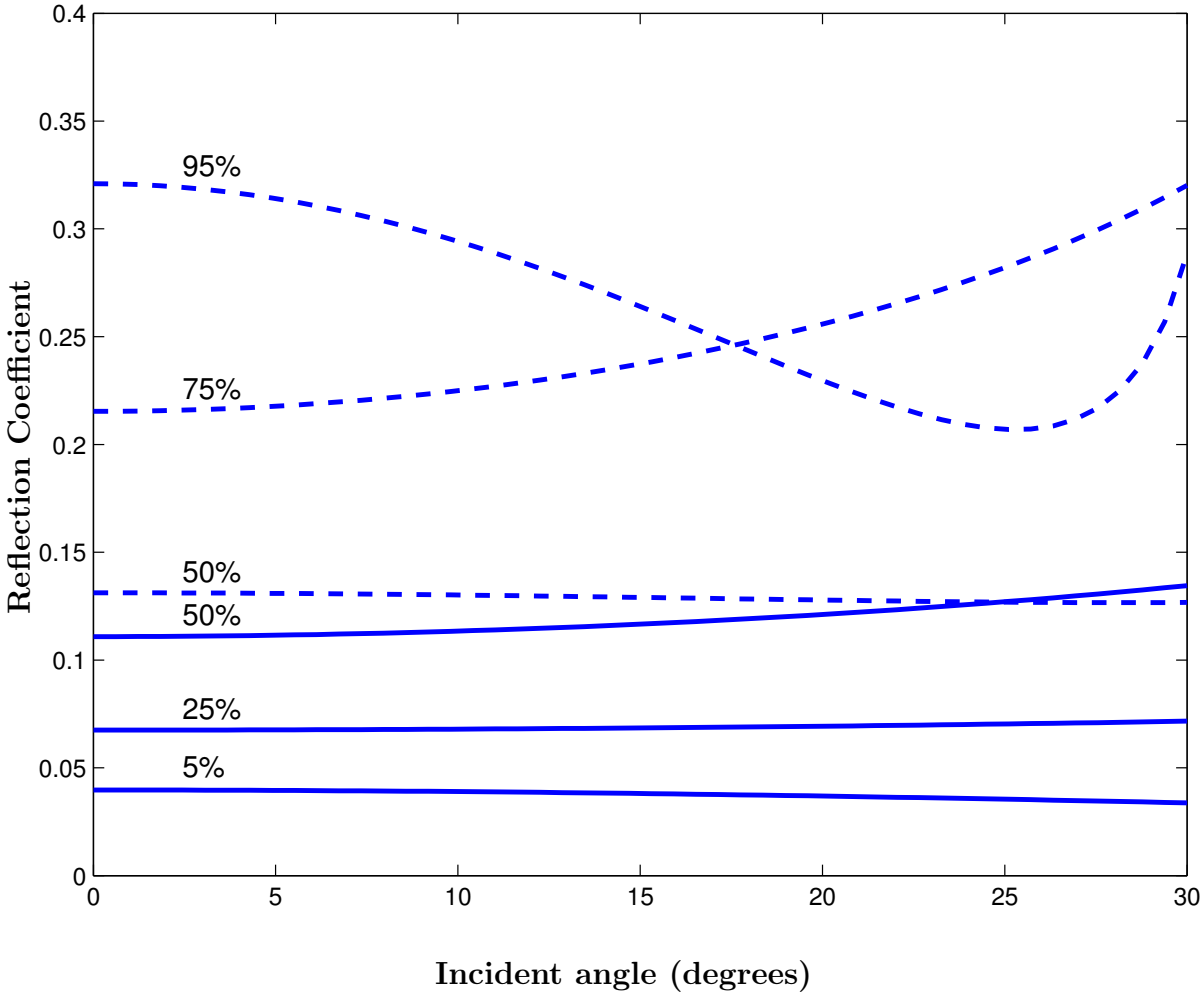

Figure 2.4: P-wave reflection coefficients R_{PP} for the top of the hydrate layer plotted as a function of incident angle for different hydrate saturation. The solid lines are for hydrates in the pore space and the dashed lines are for hydrates as part of the solid frame. The properties of the layers are given in table 2.1, and the model used is the TPEM model.

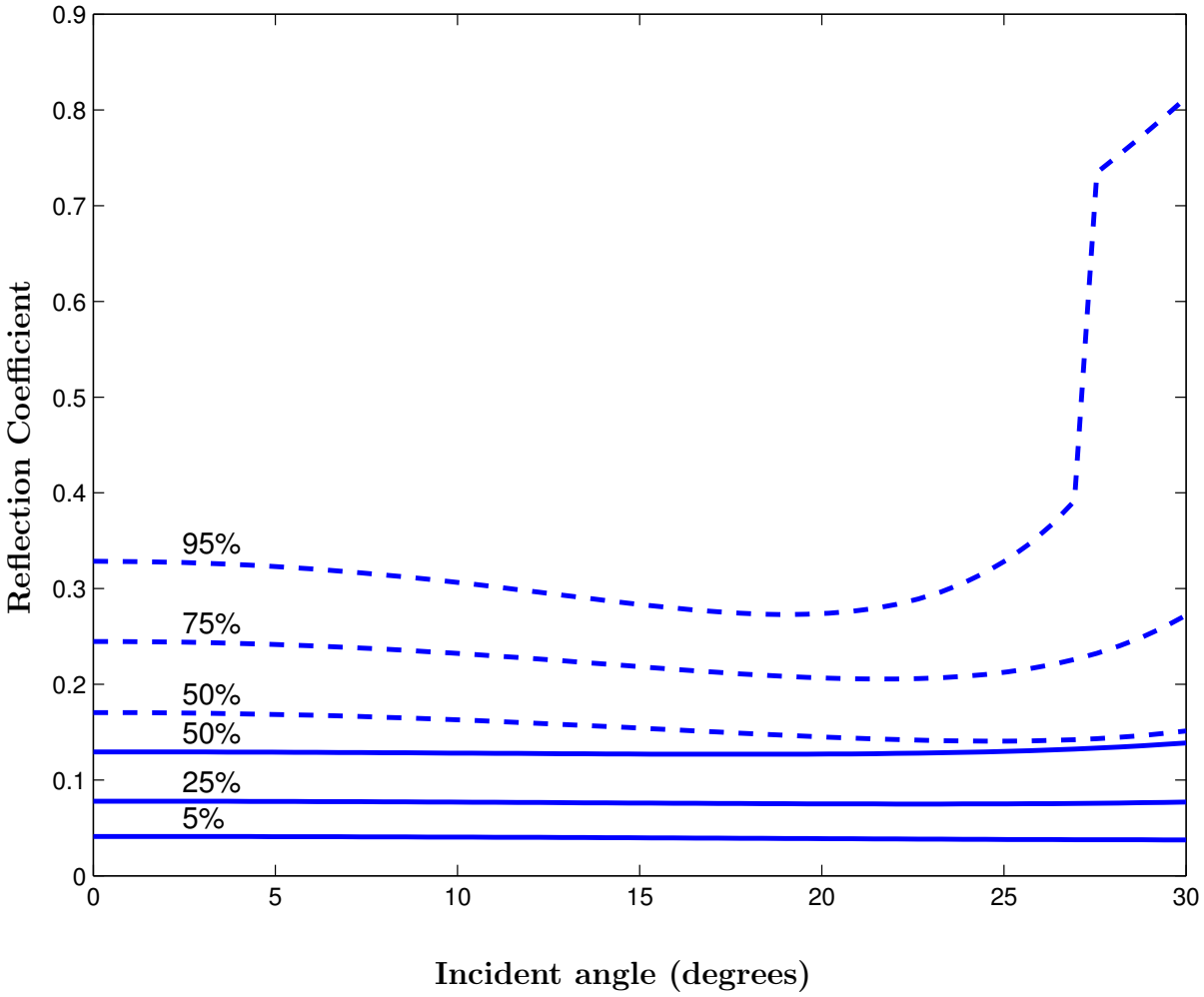

Figure 2.5: P-wave reflection coefficients R_{PP} for the top of the hydrate layer plotted as a function of incident angle for different hydrate saturation. The solid lines are for hydrates in the pore space and the dashed lines are for hydrates as part of the solid frame. The properties of the layers are given in table 2.1. The aspect ratio is 1/20 and the grains are orientated according to the distribution in figure 1.23.

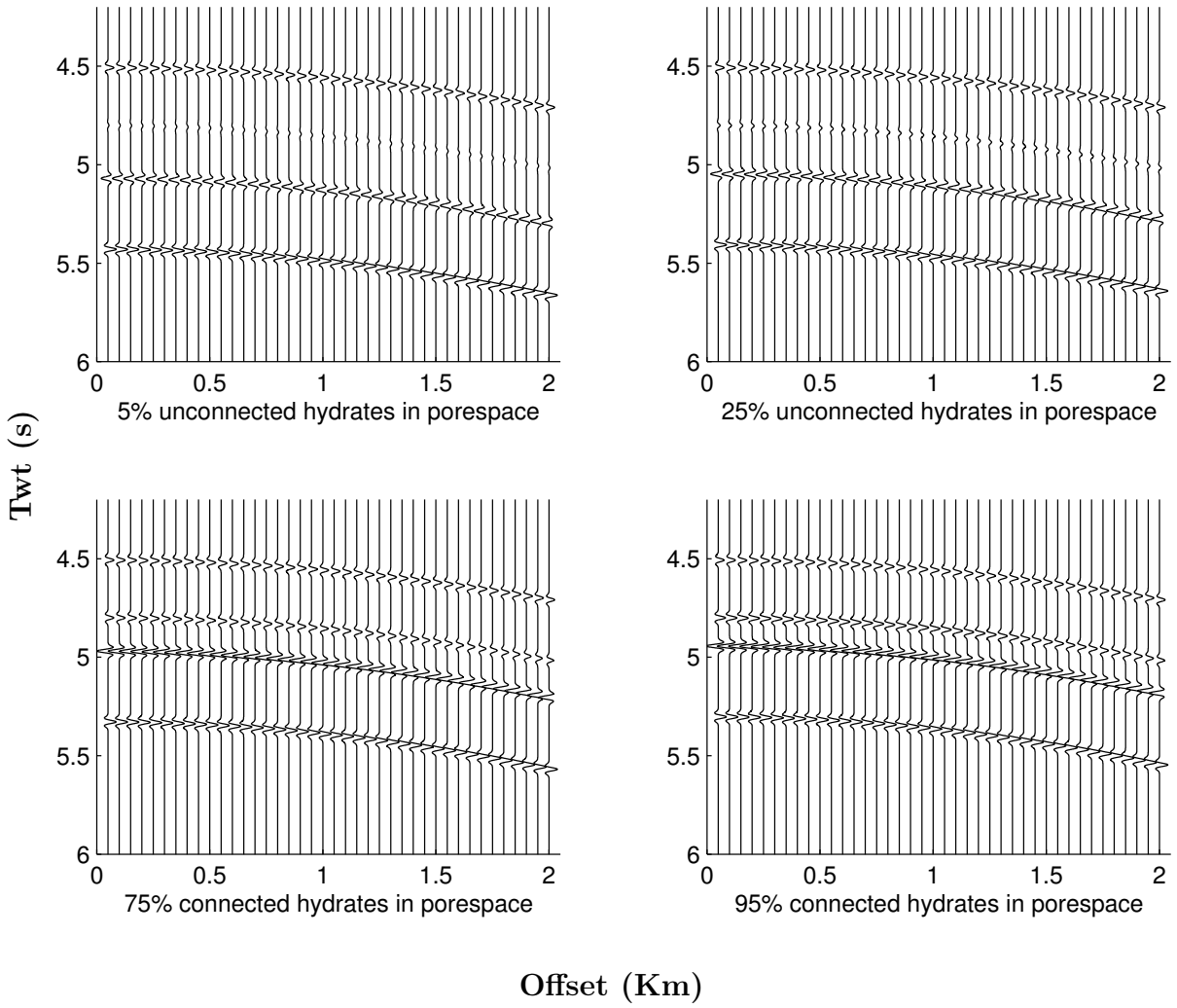

Figure 2.6: Synthetic seismograms for the DEM model with completely dissordered crystals. The layer below the hydrate layer is filled with 50% gas in the pore space.

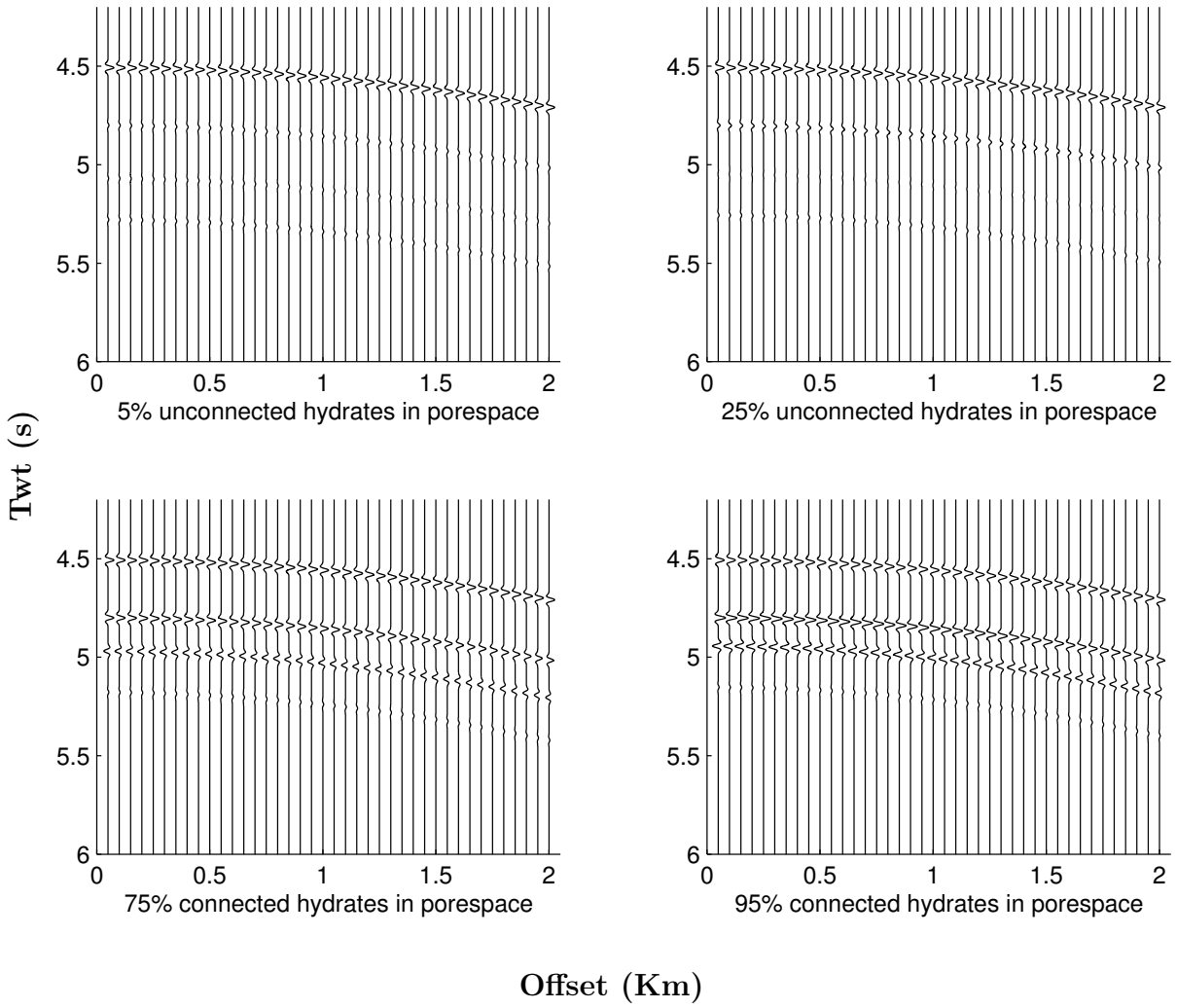

Figure 2.7: Synthetic seismograms for the DEM model with completely dissordered crystals. The layer below the hydrate layer is completely brine saturated.

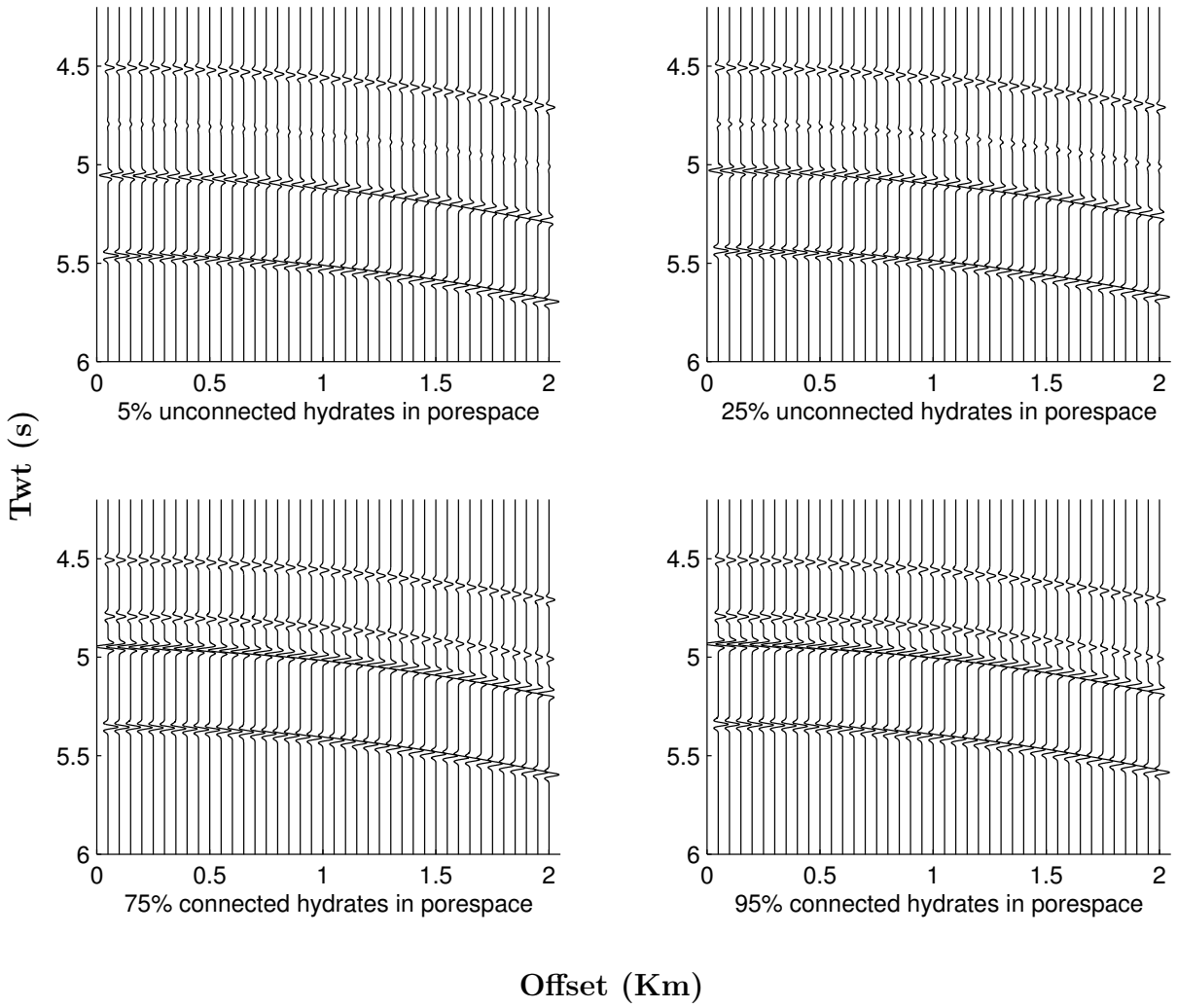

Figure 2.8: Synthetic seismograms for the DEM model with spherical components. The layer below the hydrate layer is filled with 50% gas in the pore space.

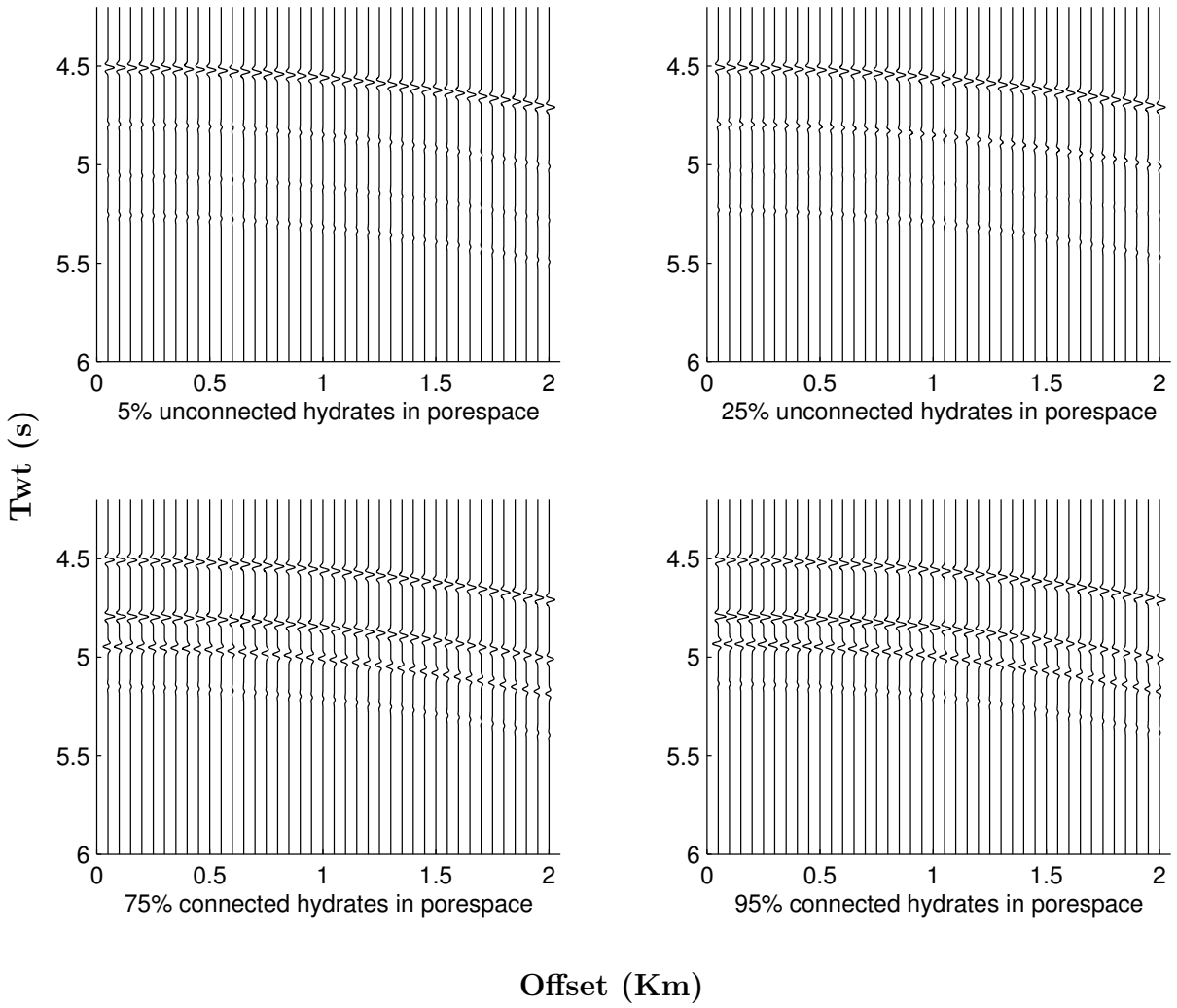

Figure 2.9: Synthetic seismograms for the DEM model with spherical components. The layer below the hydrate layer is completely brine saturated.

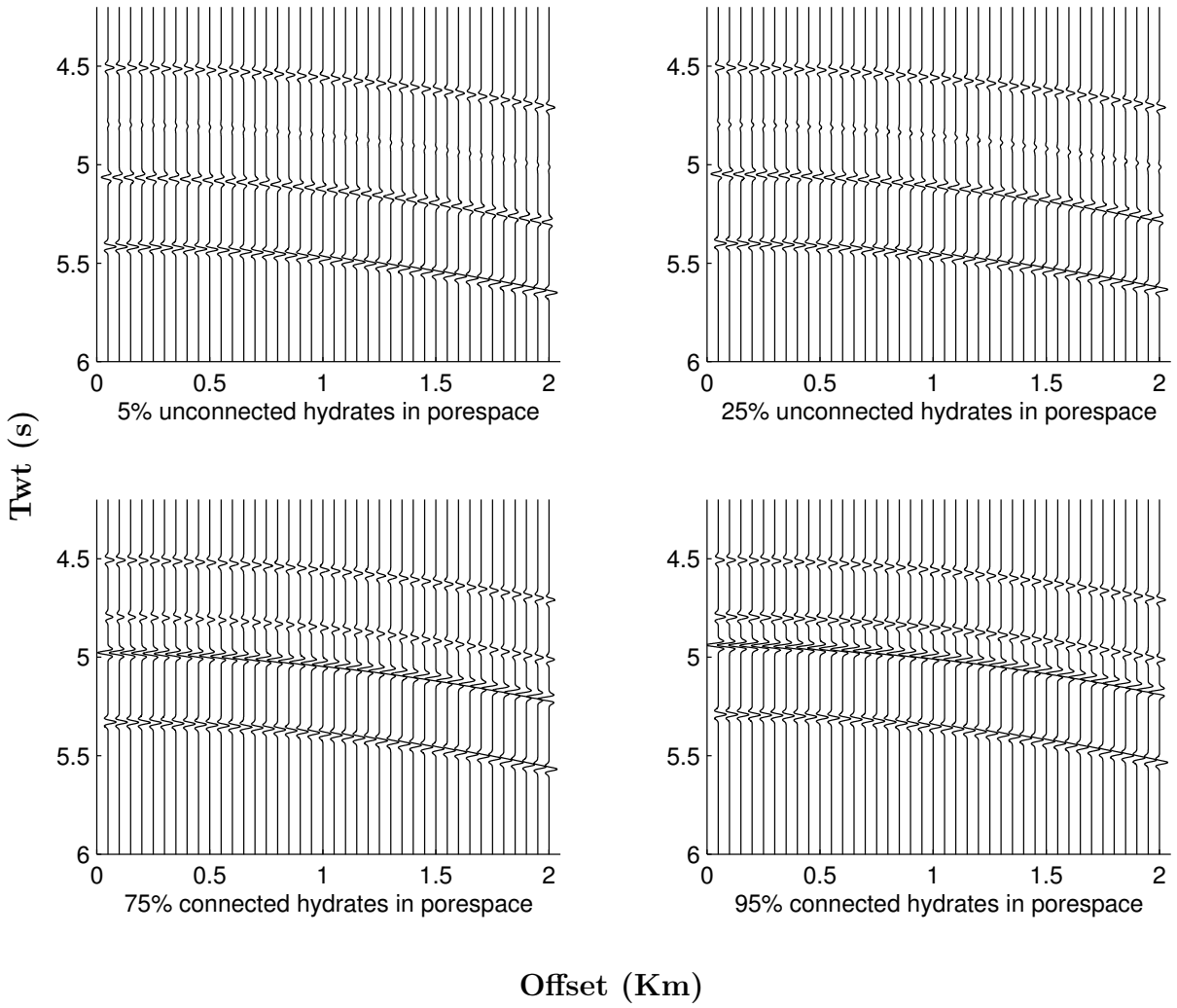

Figure 2.10: Synthetic seismograms for the TPEM model. The layer below the hydrate layer is filled with 50% gas in the pore space.

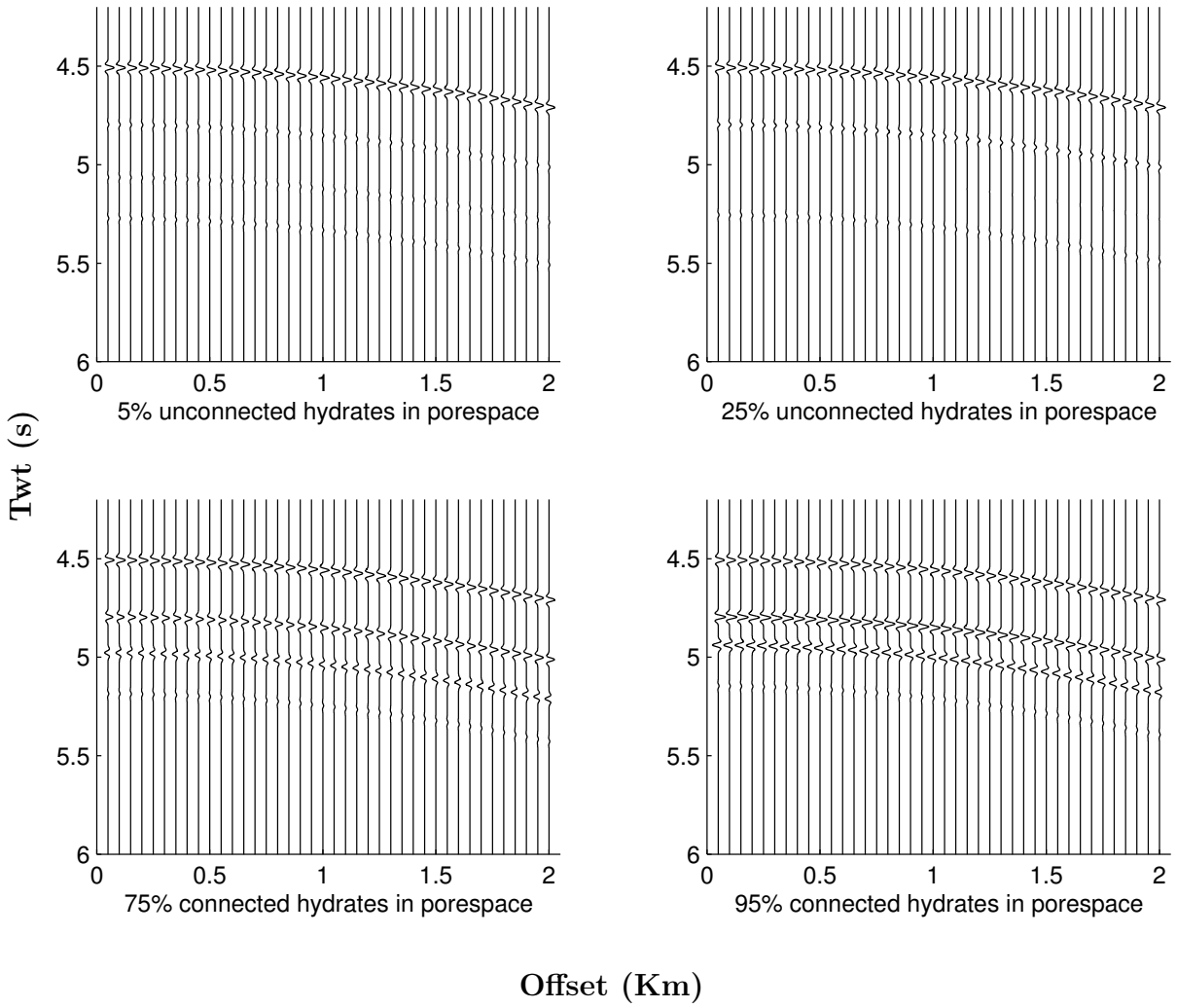

Figure 2.11: Synthetic seismograms for the TPEM model. The layer below the hydrate layer is completely brine saturated.

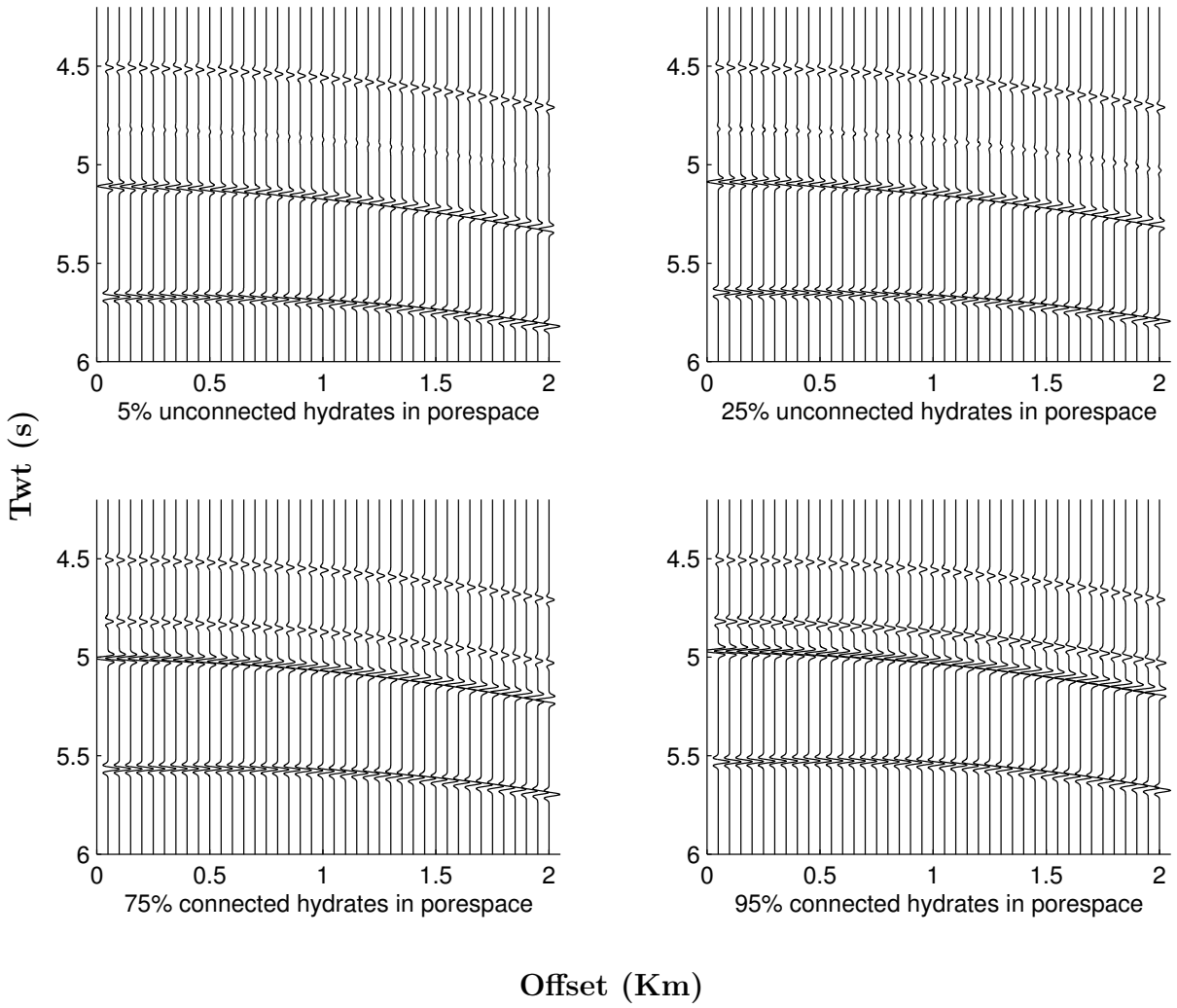

Figure 2.12: Synthetic seismograms for the DEM model with partially aligned microstructure. The layer below the hydrate layer is filled with 50% gas in the pore space.

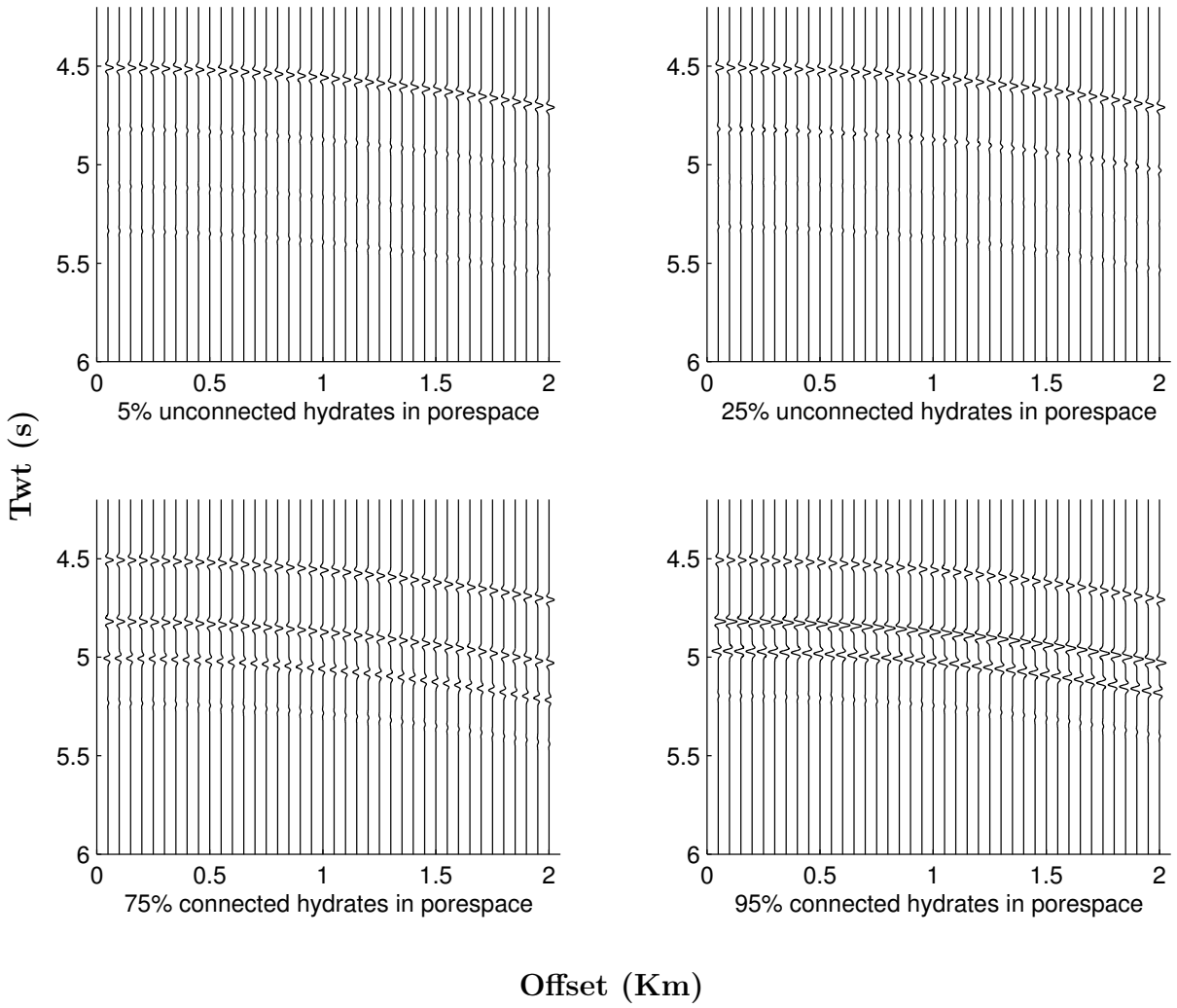

Figure 2.13: Synthetic seismograms for the DEM model with partially aligned microstructure. The layer below the hydrate layer is completely brine saturated.

Chapter 3

INVERSION OF SEISMIC AVA DATA FOR HYDRATE CONCENTRATION

3.1 Introduction

In chapter 1 and 2 the effect of gas hydrates on seismic properties was modeled. Rock physics models were used that related the porosity and hydrate saturation to elastic properties and seismic velocities. Next Aki-Richard's (isotopic case) and Rüger's (anisotropic case) approximations were used to calculate the AVO data, $R_{PP}(\theta)$. In this chapter we will try to make quantitative estimates on the hydrate saturation on the basis of AVO data, and investigate the uncertainties that arise from noise in the data. The effects of using a different model for the inversion, than was used in the forward modeling will be explored.

3.2 Bayesian non-linear inversion

The goal of inverse theory is to obtain information regarding the parameters that describes a physical system from some measurable quantities. In other words, one wishes to make some sort of quantitative inference about the model m on the basis of some measured data d. The data always consists of a finite number of measures that can be represented in a vector $\mathbf{d}$. The model on the other hand, depending on the problem, can either be a finite set of parameters or some continuous function. In practice it is however necessary to make a discretized approximation, described as a vector $\mathbf{m}$. It is commonly assumed that the fundamental physics is understood so that $\mathbf{d}$ and $\mathbf{m}$ can be related by a operator $\mathbf{g}$ (known as the forward operator) working on the data (Aster et al., 2013):

$$\mathbf{g}(\mathbf{m}) = \mathbf{d}. \tag{3.1}$$

An important issue is that measurements will always contain noise and if the same observation was performed several times, each measurement would be different. We can regard the data as consisting of two parts, a noiseless observation from a "perfect" experiment $\mathbf{d}_{true}$ and a noise

component $\boldsymbol{\eta}$ (Aster et al., 2013):

$$\begin{aligned} \mathbf{d} &= \mathbf{g}(\mathbf{m}_{true}) + \boldsymbol{\eta} \\ &= \mathbf{d}_{true} + \boldsymbol{\eta} \end{aligned}, \tag{3.2}$$

where $\mathbf{m}_{true}$ is the true model satisfying equation 3.1 perfectly for the true, noise free data, assuming the forward modeling is exact. The noise can be regarded as a random variable, that can be described by an arbitrarily complicated probability density function. In many cases, however, the noise will follow a Gaussian normal distribution. This distribution is so common because it is the limiting probability density function for a sum of random variables. The probability density function for the data can then be written as a Gaussian normal distribution with mean value $\mathbf{g}(\mathbf{m})$ (Menke, 2012):

$$f(\mathbf{d}|\mathbf{m}) \propto exp\left(-\frac{1}{2}\left[\mathbf{g}(\mathbf{m}) - \mathbf{d}\right]^T \mathbf{C}_D^{-1}\left[\mathbf{g}(\mathbf{m}) - \mathbf{d}\right]\right), \tag{3.3}$$

where $\mathbf{C}_D$ is the covariance matrix for the data. The diagonal elements of $\mathbf{C}_D$ are the variance σ_d^2 for the elements of the data vector, and the off diagonal elements describes the correlation between pairs of data.

The classical approach to the inverse problem assumes the existence of a specific but unknown model parameters that needs to be uncovered. In the Bayesian approach on the other hand, the model is regarded as a random variable and the solution is given as a probability distribution for the model parameters, for a given set of data, known as the posterior distribution $q(\mathbf{m}|\mathbf{d})$. Any information we may have on the model before the experiment is expressed as a prior distribution $p(\mathbf{m})$. This information is incorporated into the solution using Bayes theorem to form an expression for the posterior distribution (Aster et al., 2013)

$$q(\mathbf{m}|\mathbf{d}) = \frac{f(\mathbf{d}|\mathbf{m})\, p(\mathbf{m})}{c}, \tag{3.4}$$

where c is a normalization constant given by an integral over all models

$$c = \int_{all\ models} f(\mathbf{d}|\mathbf{m})\, p(\mathbf{m})\, . \tag{3.5}$$

The prior distribution can take many forms, but it can in some cases be useful to describe it as a Gaussian normal distribution with mean value defined as some prior expected value for $\mathbf{m}$. We also introduce a covariance matrix $\mathbf{C}_M$ where the diagonals describe the certainty of the prior knowledge regarding an elements in the model vector, and the off diagonal describes the correlation between pairs of model parameters in the prior distribution. We then have the following expression for the prior distribution (Aster et al., 2013):

$$p(\mathbf{m}) \propto exp\left(-\frac{1}{2}\left[\mathbf{m} - \mathbf{m}_{prior}\right]^T \mathbf{C}_M^{-1}\left[\mathbf{m} - \mathbf{m}_{prior}\right]\right) \tag{3.6}$$

When we combine this distribution with the one from equation 3.3 into equation 3.4, we obtain

$$q(\mathbf{m}|\mathbf{d}) = N \cdot e^{-J(\mathbf{m})}, \tag{3.7}$$

where $N = 1/c$ is a normalization constant and $J(\mathbf{m})$ is the objective function given by (Aster et al., 2013):

$$J(\mathbf{m}) = \frac{1}{2}\left(\left[\mathbf{g}(\mathbf{m}) - \mathbf{d}\right]^T \mathbf{C}_D^{-1}\left[\mathbf{g}(\mathbf{m}) - \mathbf{d}\right] + \left[\mathbf{m} - \mathbf{m}_{prior}\right]^T \mathbf{C}_M^{-1}\left[\mathbf{m} - \mathbf{m}_{prior}\right]\right). \tag{3.8}$$

In the case of a uninformative prior, the objective function reduces to:

$$J(\mathbf{m}) = \frac{1}{2}\left(\left[\mathbf{g}(\mathbf{m}) - \mathbf{d}\right]^T \mathbf{C}_D^{-1}\left[\mathbf{g}(\mathbf{m}) - \mathbf{d}\right]\right). \tag{3.9}$$

The model that best matches the data and prior knowledge on the model parameters can be found by maximizing the objective function (equation 3.8). It can, however, be useful to perform an analysis to quantify the uncertainties in the estimate of the model parameters to determine the quality of the estimate. For non-linear problems, this can not be done analytically and the exploration of the posterior distribution can only be done by sampling. As long as the number of model parameters is relatively small, we can define a grid, dense enough to incorporate all the features of the posterior distribution, and compute the value of the distribution everywhere on that grid. In order to analyze the uncertainty regarding a specific model parameter m_i, the marginal distribution is calculated. This can be done by numerical integration with respect to the other model parameters:

$$q(m_i) = \int q(\mathbf{m}|\mathbf{d})\, dm_1 ... dm_{i-1} dm_{i+1} ... dm_n. \tag{3.10}$$

The numerical integration should be done on a grid dense enough so that all the important features of the distribution are incorporated. If the number of model parameters is large, this will be very time consuming. In this case, sampling from the distribution using Mote Carlo Markov chain (MCMc) can be more effective. MCMc methods involves random sampling from the distribution, where each step is only dependent on the previous step. The Metropolis-Hasting algorithm is a McMc method with a specified limiting distribution. This method can be used for sampling the posterior distribution (Tarantola, 2005):

$$q(\mathbf{d}|\mathbf{m}) = N \cdot p(\mathbf{m})\, f(\mathbf{d}|\mathbf{m}) \tag{3.11}$$

We design a random walk that if all the transitions where accepted, would sample the prior distribution $p(\mathbf{m})$. Suppose that at a given step the random walker is at a point $\mathbf{m}_i$, and the transition to a point $\mathbf{m}_j$ is governed by the following rules (Tarantola, 2005):

- If $f(\mathbf{m}_j|\mathbf{d}) \geq f(\mathbf{m}_i|\mathbf{d})$, then accept the proposed transaction to $\mathbf{m}_j$
- If $f(\mathbf{m}_j|\mathbf{d}) < f(\mathbf{m}_i|\mathbf{d})$, then decide randomly to move to $\mathbf{m}_j$, or stay at $\mathbf{m}_i$, with the following probability of accepting the transition to $\mathbf{m}_j$,

$$P_{i\to j} = \frac{f(\mathbf{m}_j|\mathbf{d})}{f(\mathbf{m}_i|\mathbf{d})} \tag{3.12}$$

The random walk will then sample the posterior distribution.

3.3 Inversion procedure

The Bayesian non-linear inversion procedure will be adopted and applied to the case of inversion of seismic AVA data for hydrate saturation and porosity. The data vector of equation 3.1 will in this case be the reflection coefficient for n angles θ_i, and the forward operator will be a combination of the rock physic model and the reflectivity approximation. It is assumed that the overburden and other parameters in the rock physics models are fully known, such that $R_{PP}^{calc}(\theta)$ becomes a function of hydrate saturation S_h and porosity ϕ only. The data are assumed to be uncorrelated and gaussian distributed with standard deviation σ_i, and uninformative prior. The objective function then becomes:

$$J(S_h, \phi) = \sum_{i=1}^{n} \left[\frac{R_{PP}^{calc}(S_h, \phi, \theta_i) - R_{PP}^{obs}(\theta_i)}{\sigma_i} \right]^2 . \tag{3.13}$$

The next step is then to calculate the marginal distributions. This can be done numerically by solving the integral in equation 3.1 over a set of grid points, using the trapezoidal rule. First the normalization constant is calculated:

$$\frac{1}{N} \approx \frac{\Delta S_h \Delta \phi}{4} \sum_{k=1}^{K} \sum_{l=1}^{L} \left[e^{-J\left(S_{h_{l+1}}, \phi_{k+1}\right)} + e^{-J\left(S_{h_{l+1}}, \phi_k\right)} \right] \tag{3.14}$$

The marginal distribution for hydrate saturation is then given by

$$q(S_h) \approx N \frac{\Delta \phi}{2} \sum_{k=1}^{K} \left[e^{-J(S_h, \phi_{k+1})} + e^{-J(S_h, \phi_k)} \right], \tag{3.15}$$

and for porosity

$$q(\phi) \approx N \frac{\Delta S_h}{2} \sum_{l=1}^{L} \left[e^{-J\left(S_{h_{l+1}}, \phi\right)} + e^{-J\left(S_{h_l}, \phi\right)} \right]. \tag{3.16}$$

In the case of MCMc sampling, marginal distributions can be calculated by making histograms of the occurrence of model parameters within a given range. Since we have an uninformative prior, the samples are drawn such that if all the samples were accepted, the random walk would sample a uniform distribution over the model space.

3.4 Numerical results and discussion

We will now look at some results for inversion of synthetic AVA data from the top of the hydrate layer in the model from the previous chapter. The full posterior distributions are shown first with 5% standard deviation for the noise in the data. Thereafter the marginal distributions are calculated for 5% (blue line) and 10% (red line) standard deviation. The porosity is assumed to lay between $20 - 80\%$ and the hydrate saturation between $0 - 100\%$. The distributions are computed over a 500×500 grid when the TPEM model is used for inversion and 384×384 when the more computationally expensive DEM model is used.

Figure 3.1 shows the posterior distribution when the TPEM model is used for forward modeling

and inversion. The distributions are shaped as short narrow ridges, except at 75% saturation where the ridge is longer. In figure 3.2 the marginal distributions are shown. Also here the distributions are wider when the true saturation is 75%, as expected from the full posterior distribution. When the standard deviation is set to 10% the marginals at 75% true saturation are wide, with a long tail. At other saturations, the marginals stay relatively narrow.

Figure 3.3 shows the posterior distribution when the DEM model with completely disordered non-spherical components is used for forward modeling and inversion. At 5% and 25% saturation the distributions are shaped as long narrow ridges. At 75% saturation the ridge is wider, with a long declining tail. At 95% saturation the distribution is shaped as a short narrow ridge. In figure 3.4 the marginal distributions are shown. The spiked hydrate saturation marginals at 5% and 25% saturation are probably due to discretisation error. The top of the narrow ridge of the full posterior distribution falls between grid points, causing sudden drops. The hydrate saturation marginals are wide up to 95% saturation, where the distribution is very narrow. The porosity marginals are relatively narrow except at 75% saturation. Gennreally it should be possible to make a good estimate on the model parameters, except in the case of 75% true saturation, when the standard deviation for the data is 10%. In this case errors up to 80% for the hydrate saturation and 20% for the porosity are quite plausible.

Figure 3.5 shows the posterior distribution when the DEM model with spherical components is used for forward modeling and inversion. At 5% and 25% saturation the distributions are shaped as long narrow ridges, with high probability along large part of the ridges, which means that there are many specific combinations of model parameters that gives a good match to the data. At 75% it takes the form of an ellipsoid with a tail, and 95% it takes the form of a small ellipsoid, both with a defined peak, implying that there is one set of model parameters that match the data and an increasing mismatch moving away from these.

In figure 3.6 the marginal distributions are shown. Also here we see some spiked distributions that probably are caused by discretisation error. The hydrate saturation marginals show wide distributions for 5% and 25% saturation, even in the case of 5% standard deviation for the data. Errors as large as 25% in the case of 25% saturation are have high likelihood. The result at 5% saturation are hard to interpret due to the discretisation errors, but also here it appears that large errors are plausible. The porosity distributions at these saturations have a peak to the left of the true saturation. This can also be due to discretisation error, but can also mean that the number of likely combinations are larger at this porosity. At 75% saturation, the uncertainty is small when the standard deviation for the data is 5%, while at 10% large errors in estimates of saturation and porosity are likely. At 95% saturation the uncertainties are small.

In figure 3.7 and 3.8 the distributions for inversion using the TPEM model of data generated with the DEM model with completely disordered non-spherical components are shown. The peaks of the distributions are quite close to the true model parameters, except in the case of

75% saturation, where the maximum is at 0% saturation and around 35% porosity.

In figures 3.9 and 3.10 the distributions for inversion using the isotropic DEM with completely disordered non-spherical components for inversion and the anisotropic DEM model with partially aligned structure used to generate the data. The velocity of the overburden is set to the vertical velocity from the anisotropic DEM model. Also here some of the distributions are spiked, and can be hard to interpret. It appears that the peak is close to the true model parameters when the saturation is 5%. When the saturation is 25%, we see an error of around 10% in the hydrate saturation and $5-10\%$ in the porosity. At 75% saturation, there is a very sharp spike in the saturation and porosity marginals at around 90% and 70% ,respectively, when the standard deviation for the data is set to 10%. When the standard deviation is set to 5% the saturation distribution is everywhere zero, and the posrosity distribution has a top at the true porosity. Probably, the spike is also present at 5% standard deviation, but here it is sharper so it falls between grid points. At 95% saturation the distributions are everywhere zero.

In figures 3.11 and 3.12 the distributions for inversion and forward modeling with the TPEM model, but with the wrong saturation geometry for the inversion, are shown. At 5% saturation the peak is very close to the true porosity, and close at around 10% to the true saturation. At 25% saturation, the peak is close to the true porosity, between $60-65\%$. In this case the peak is a bit higher on the hydrate saturation at around 35%. When the saturation is higher the errors become larger. When the saturation is 75% the peak is around $35-40\%$ and 40% for the hydrate saturation and porosity, respectively. At 95% saturation, the peak is around 5% and $25-30\%$ for the porosity and saturation.

In figure 3.13 results from MCMc and numerical integration are compared. As we can see we can obtain the same distribution using MCMc. This is a more general method that can be applied when the number of model parameters are large, for example in the case where velocities are inverted for hydrate concentration for a random Gaussian reservoir model. In our case, however, numerical integration was more practical, because the distributions could be computed for different expected values (true model parameters) and standard deviations simultaneously.

3.5 Concluding remarks

In this chapter we have analyzed the uncertainties that arise when making estimates on saturation and porosity on the basis of AVA data containing Gaussian noise. The uncertainties for the TPEM model where small on the entire saturation range, whereas larger uncertainties where seen for the DEM model at low saturations. When the TPEM model was used to invert data generated with the DEM model, the estimates where in some cases close to the true values and in some cases far off. When data generated using anisotropic theory was inverted using

a similar isotropic model, some strange results arised. Also when using the wrong saturation geometry, the estimates where in some cases quite accurate and in some cases far off.

Generally, these results show that modeling errors can have a big impact on the hydrate saturation estimates. Caution should be used when selecting the rock physics model, even if it appear to give good results at one particular saturation. Isotropy is commonly assumed, even when we know that it is often not the case. We have seen that this can give large errors in the estimates.

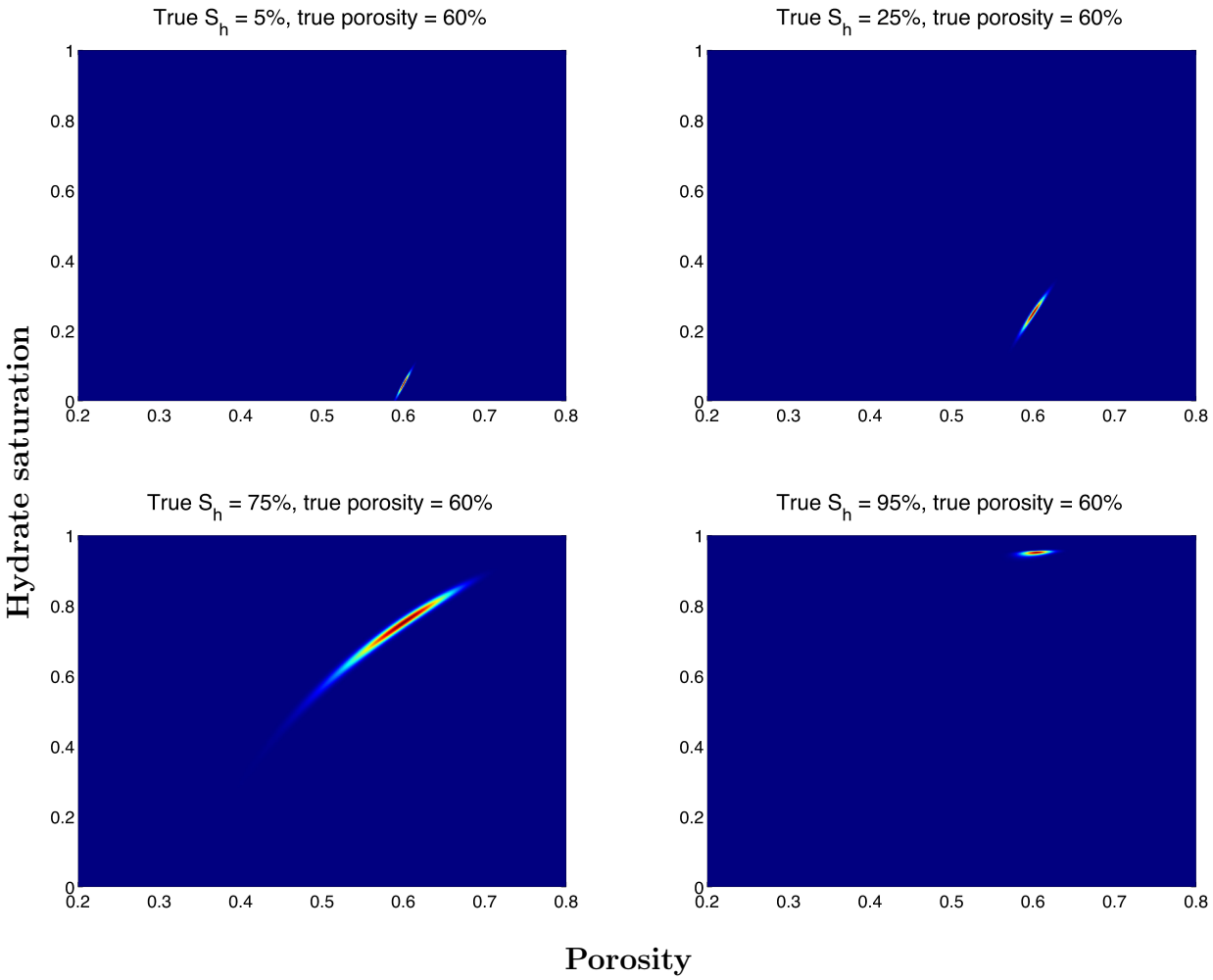

Figure 3.1: Posterior distribution for the TPEM model used for both forward and inverse modeling.

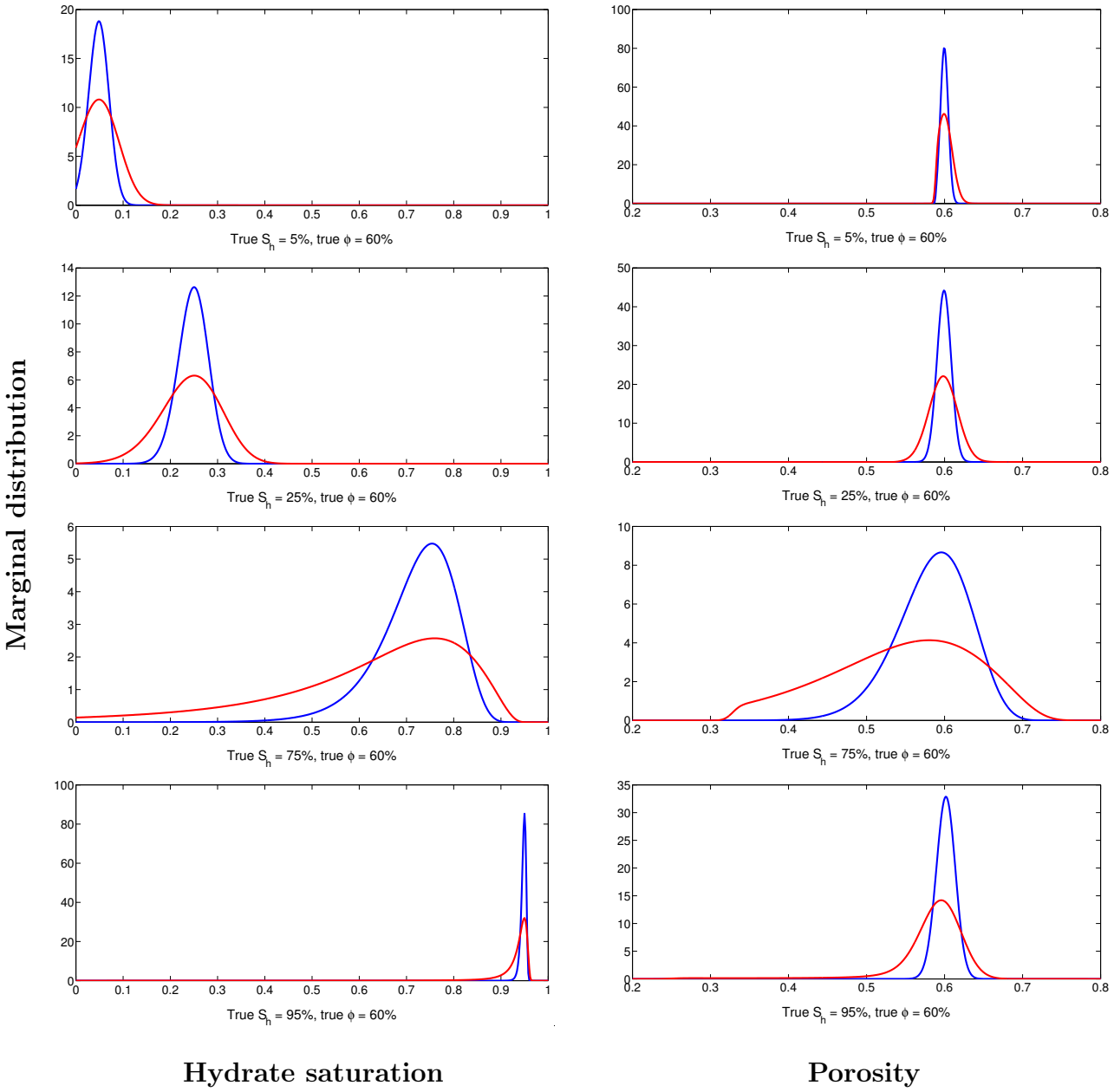

Figure 3.2: Marginal distributions for inversion with the TPEM model, with the same model used to generate the data as was used for the inversion. The blue line is for 5% standard deviation for the data error and the red line is for 10%.

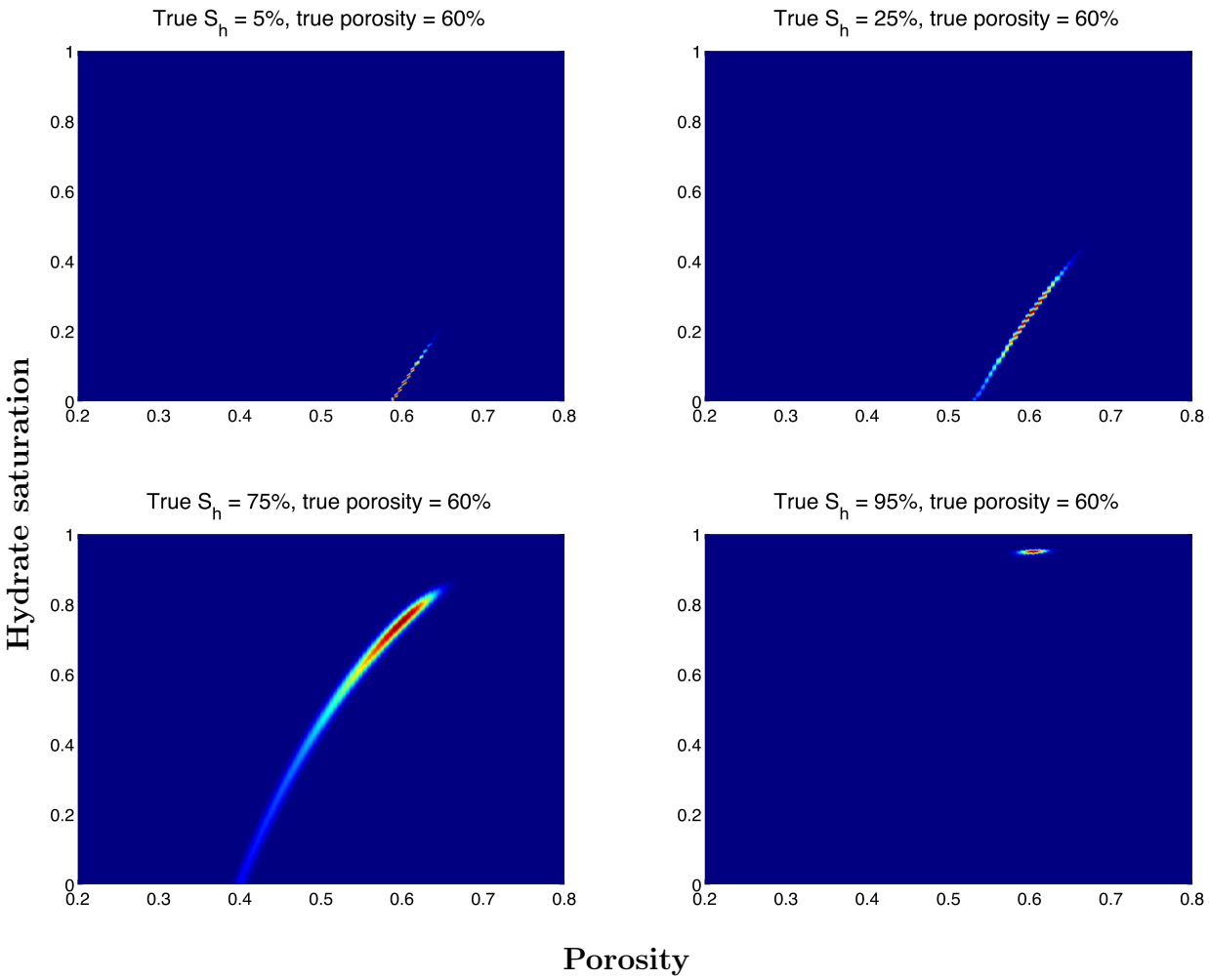

Figure 3.3: Posterior distribution for the DEM model with completely disordered non-spherical components used for both forward and inverse modeling.

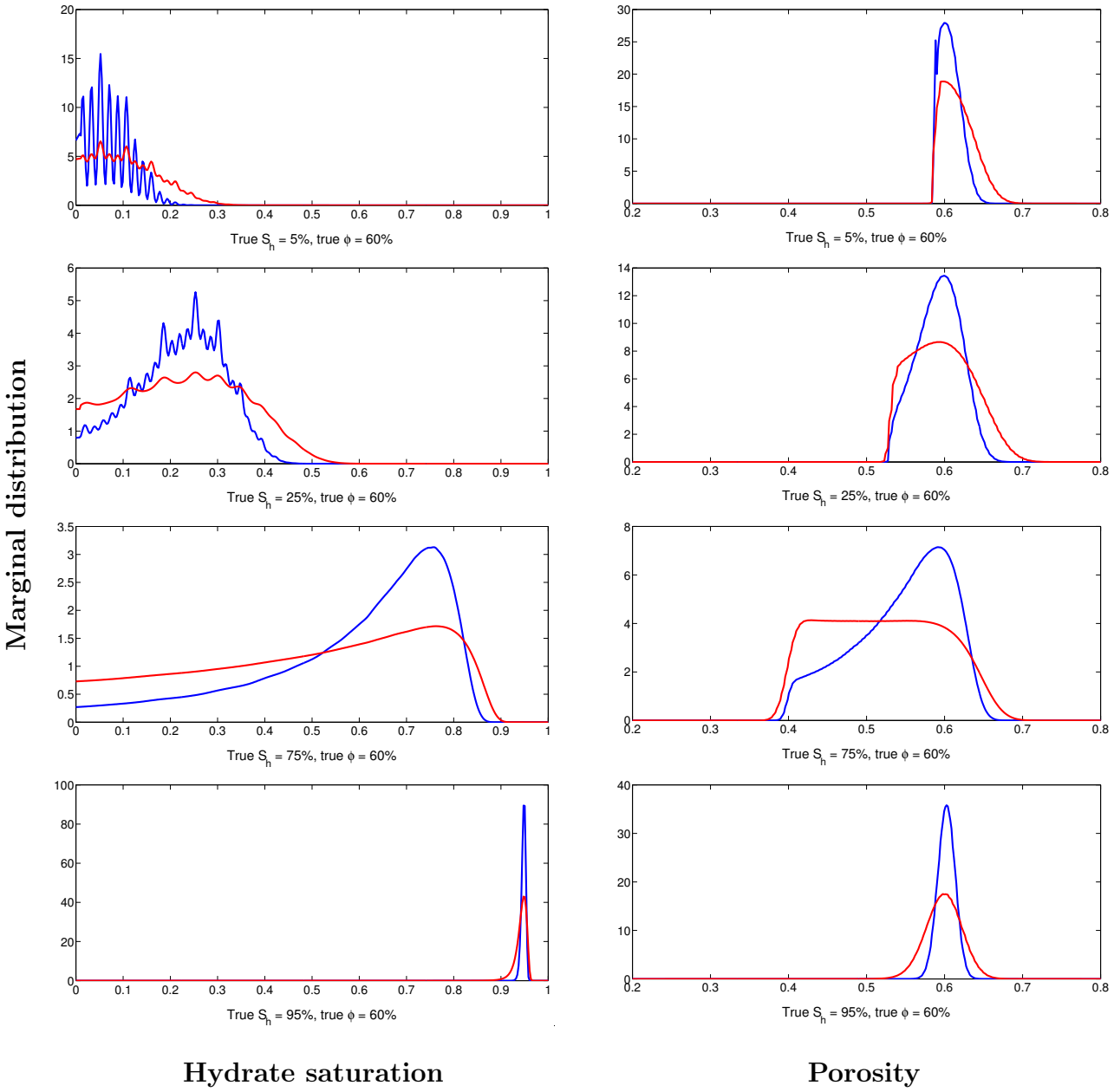

Figure 3.4: Marginal distributions for inversion with the DEM (non-spherical) model with completely disordered building blocks, with the same model used to generate the data as was used for the inversion. The blue line is for 5% standard deviation for the data error and the red line is for 10%.

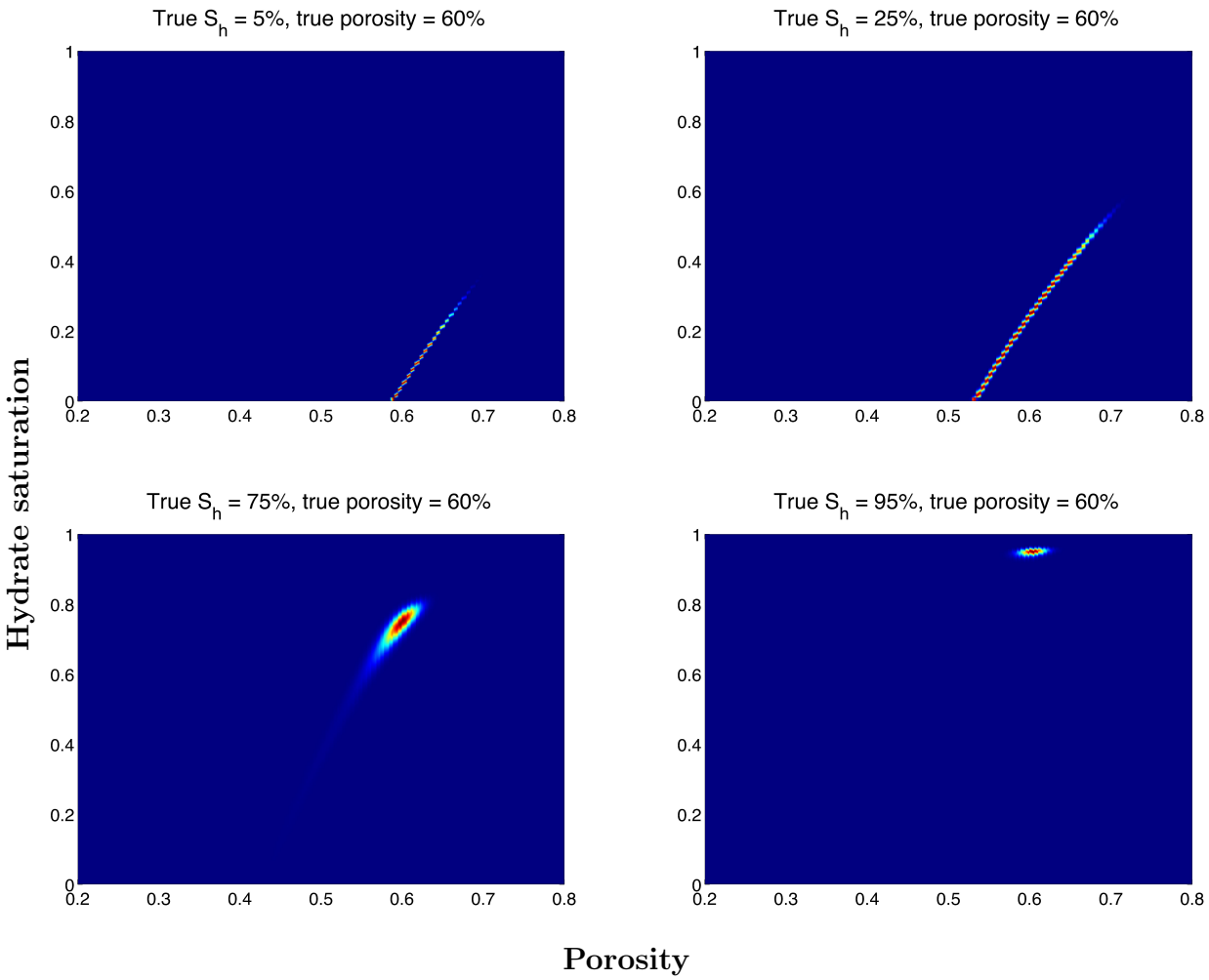

Figure 3.5: Posterior distribution for the DEM model with spherical components used for both forward and inverse modeling.

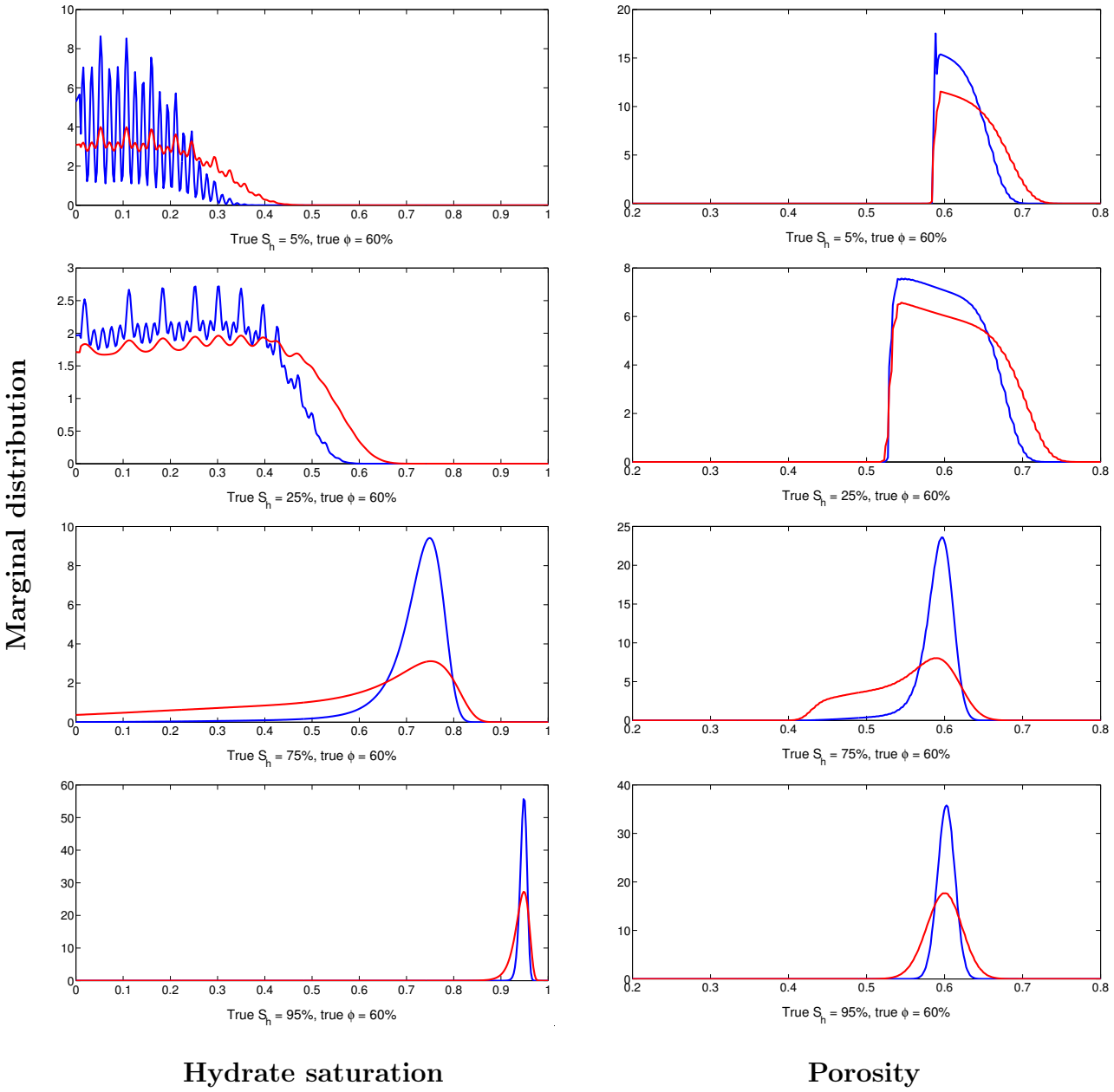

Figure 3.6: Marginal distributions for inversion with the DEM (spherical), with the same model used to generate the data as was used for the inversion. The blue line is for 5% standard deviation for the data error and the red line is for 10%.

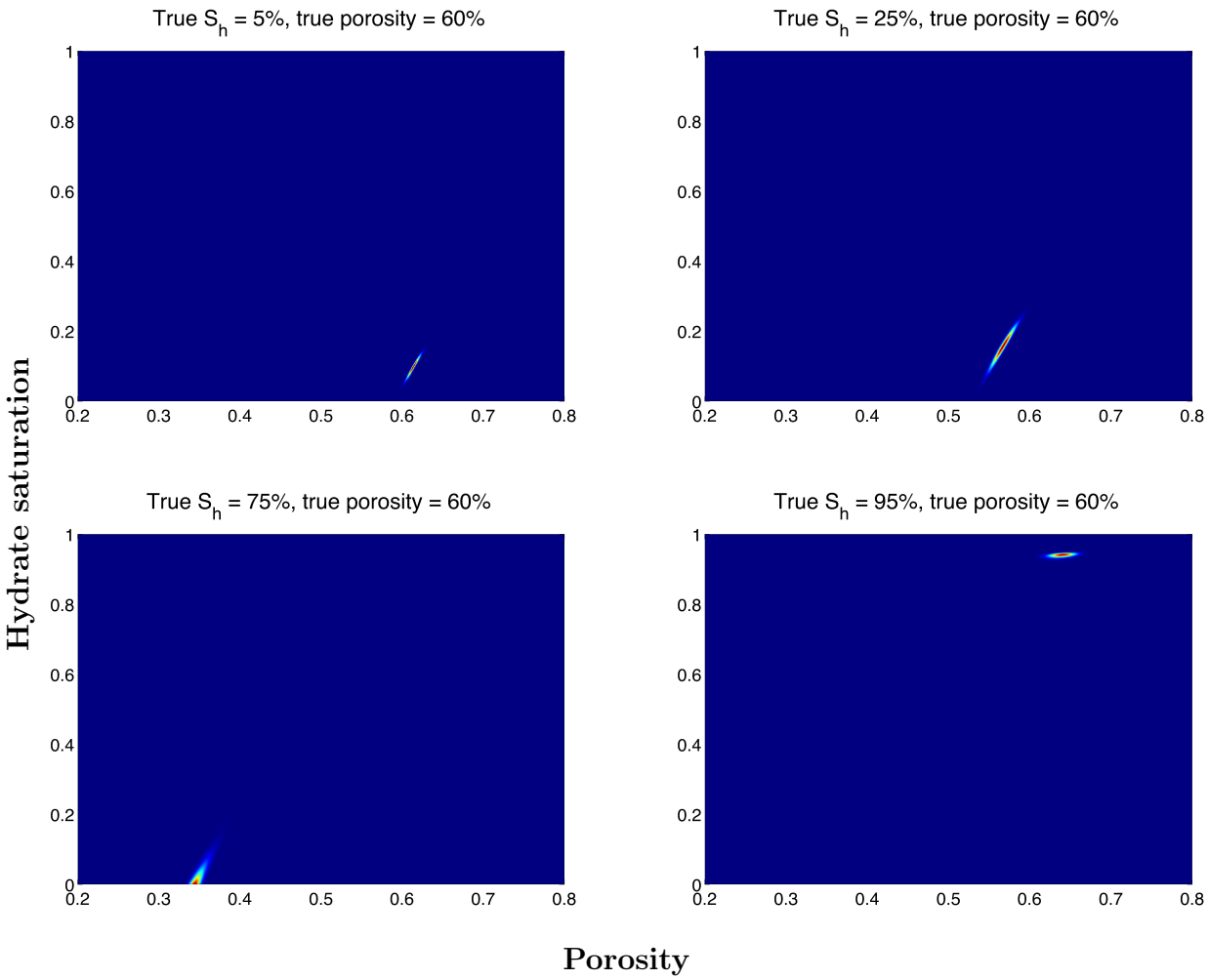

Figure 3.7: Posterior distribution for the TPEM model, with the DEM model with completely disordered non-spherical components used to generate the data.

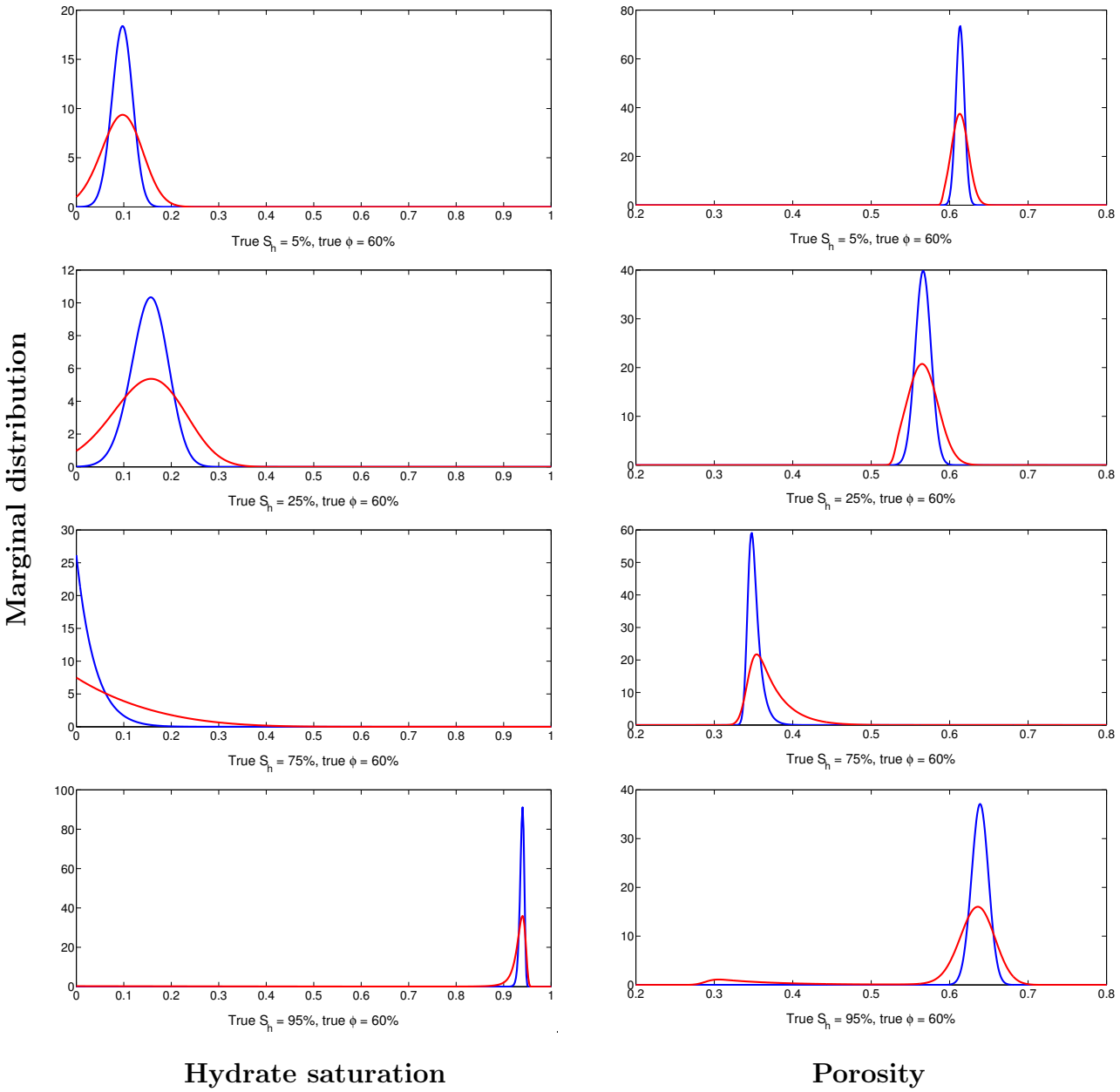

Figure 3.8: Marginal distributions for inversion with the TPEM model, with the DEM model used to generate the data. The blue line is for 5% standard deviation for the data error and the red line is for 10%.

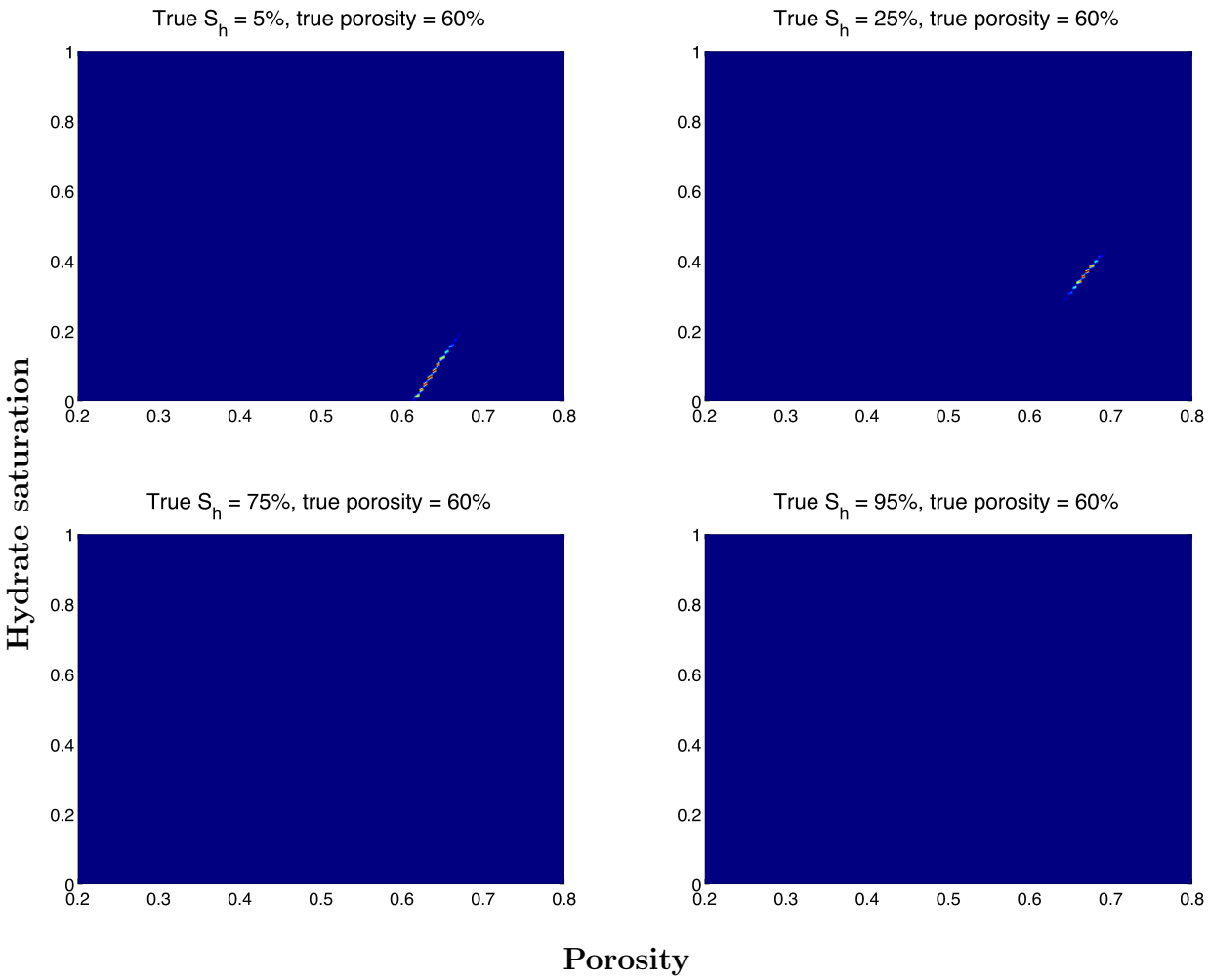

Figure 3.9: Posterior distribution for the DEM model with completely disordered microstructure, with the DEM model with partially aligned microstructure used to generate the data.

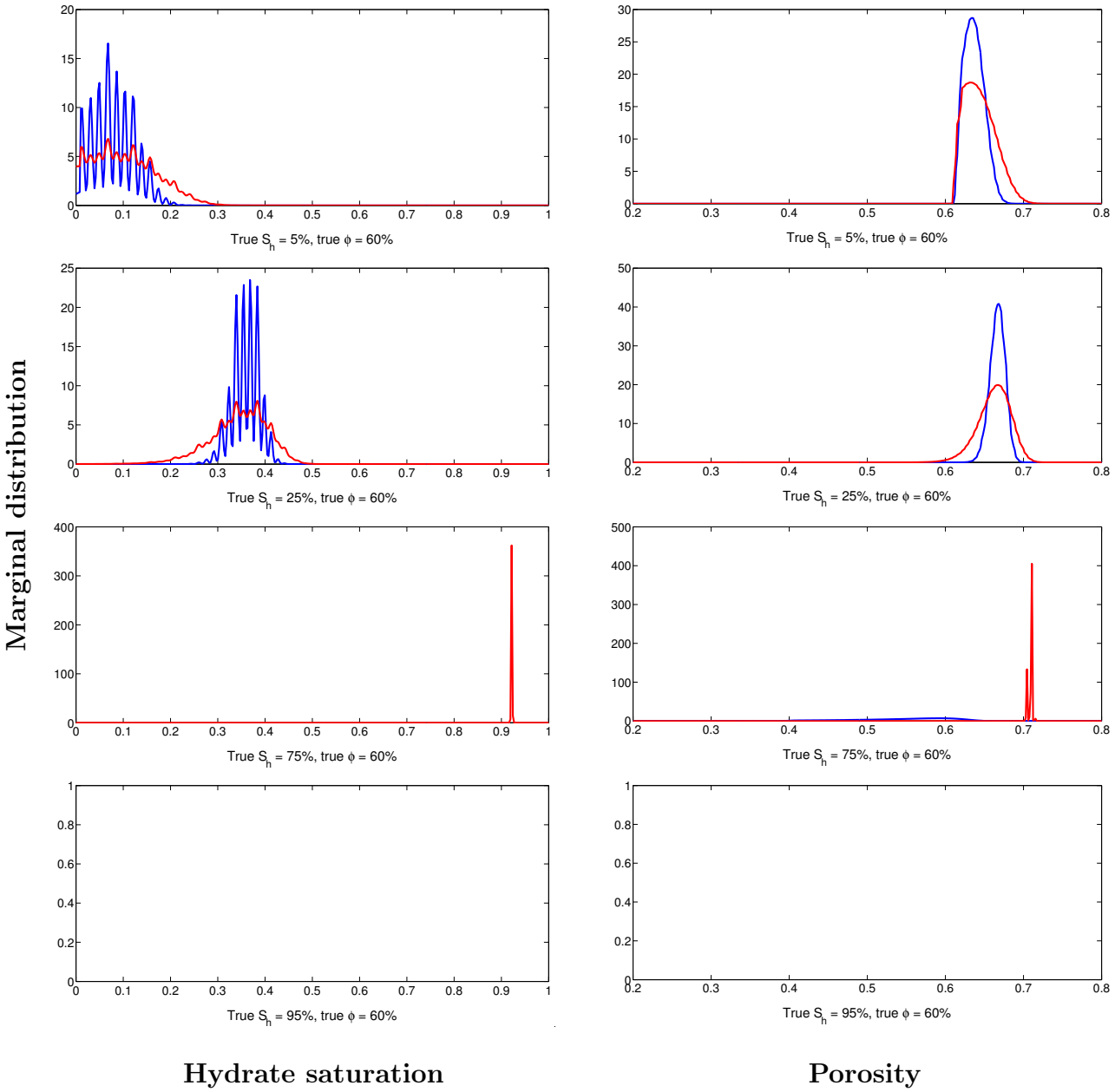

Figure 3.10: Marginal distributions for inversion with the DEM (non-spherical) model with completely disordered microstructure, with the same model but with partially aligned structure used to generate the data. The blue line is for 5% standard deviation for the data error and the red line is for 10%.

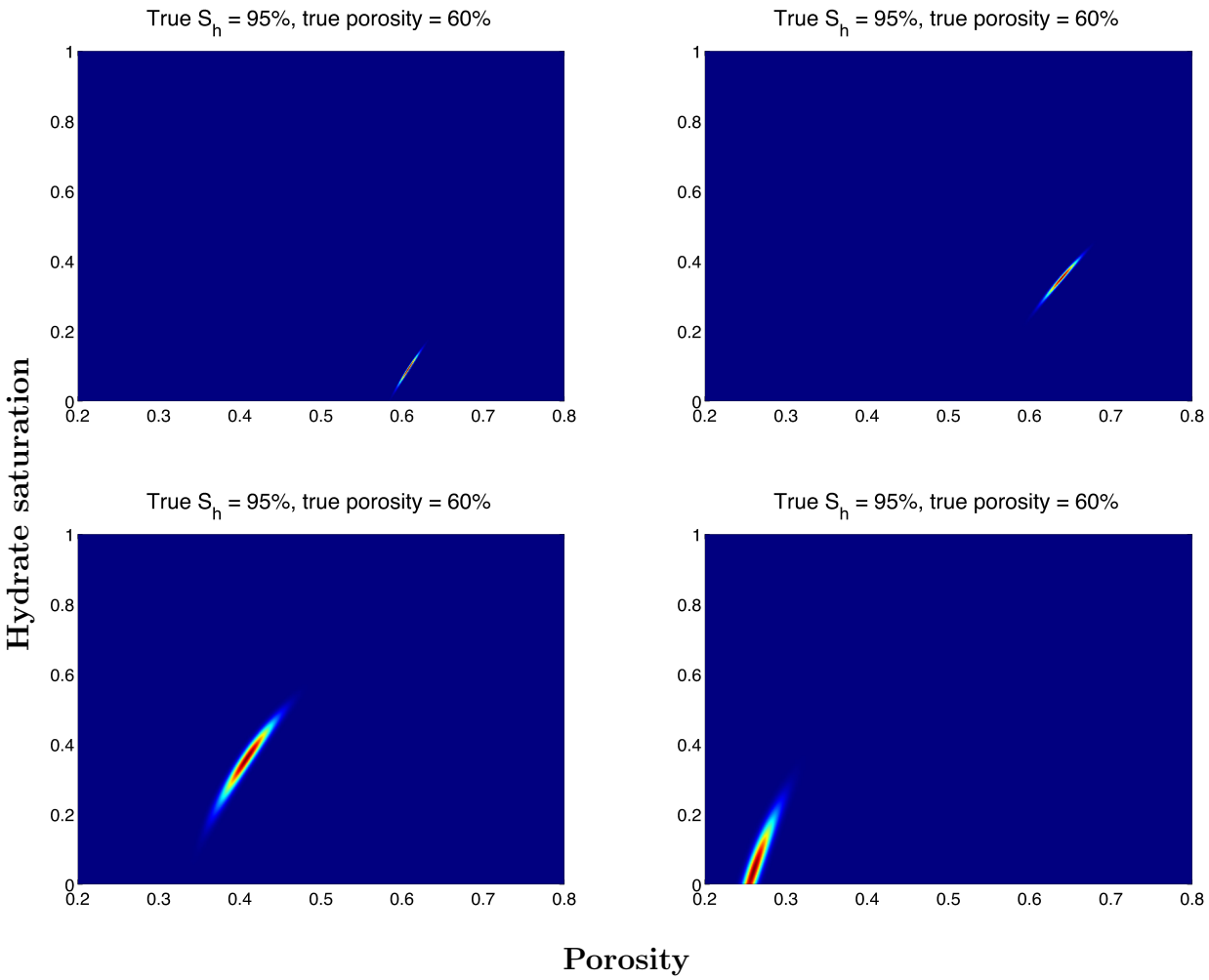

Figure 3.11: Posterior distribution for the TPEM model with the same model used to generate the data but with different hydrate saturation structure.

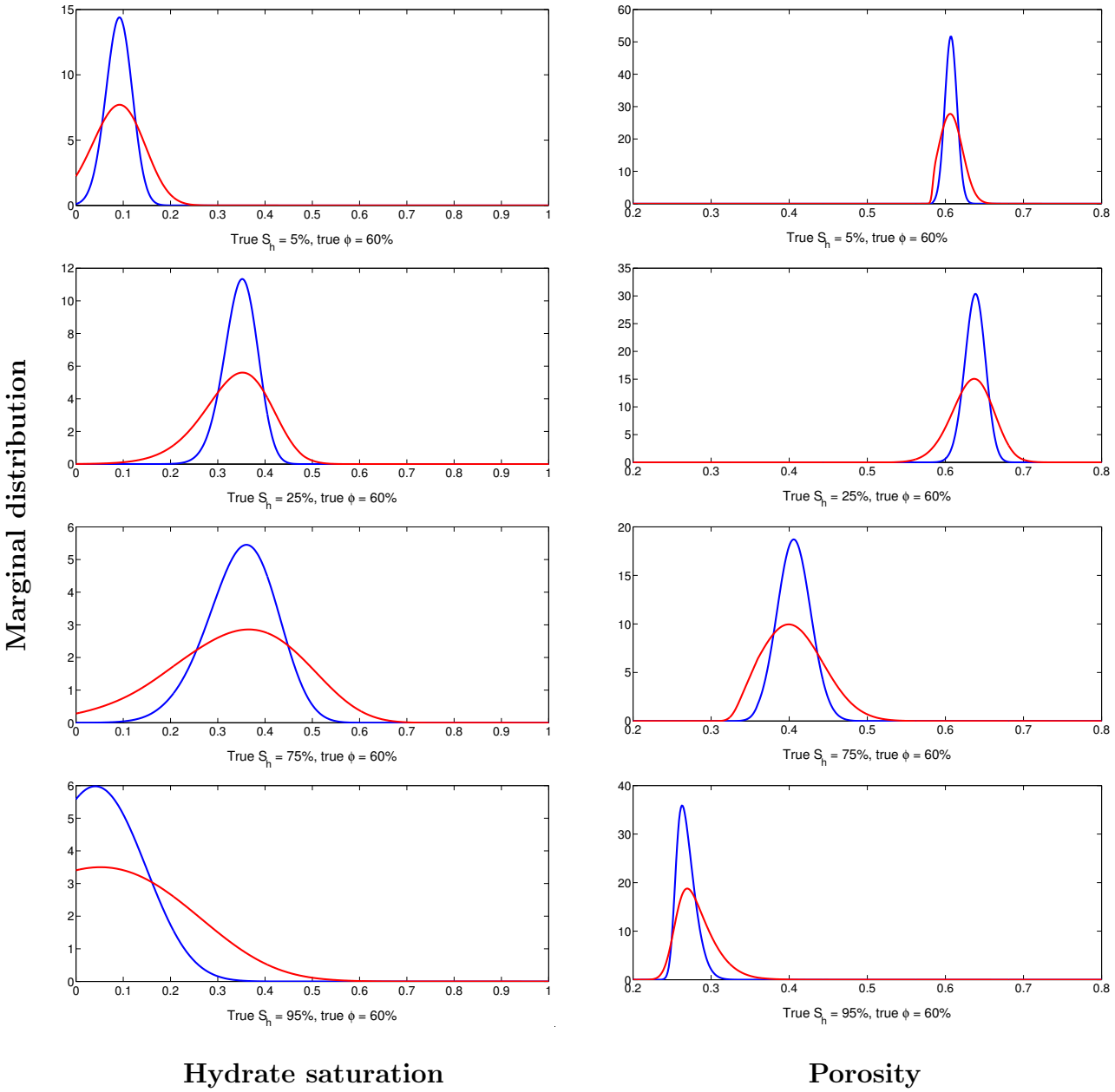

Figure 3.12: Marginal distributions for inversion with the TPEM model, with the same model used to generate the data but with different hydrate saturation structure. The blue line is for 5% standard deviation for the data error and the red line is for 10%.

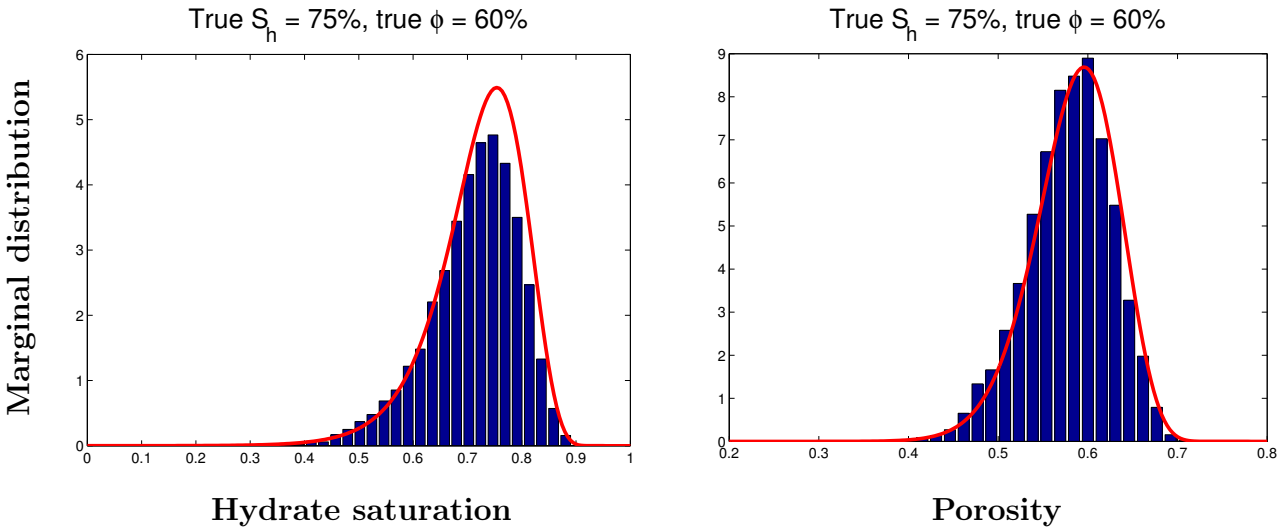

Figure 3.13: Comparison of marginal distributions calculated with numerical integration and Monte Carlo Markov Chain. The posterior distribution is from inversion with the TPEM model, with the same model used to generate the data.

Chapter 4

CONCLUDING REMARKS AND SUGGESTIONS FOR FUTURE WORK

4.1 Concluding remarks

In this thesis the effect of gas hydrates on elastic and reflectivity properties of sediments has been investigated. This has been done by using two different rock physics models, the three phase effective medium (TPEM) and differential effective medium (DEM) model and their results have been observed and compared. Velocities were modeled and reflection coefficients were calculated for an interface between a hydrated layer and brine saturated overburden, and synthetic seismograms were computed for a layered model. We have seen that these models can have large variations in trends and estimated properties, although the seismograms looked very similar for the different models. It was also seen in the inversion results that using the wrong model can give accurate results in some cases while it in other cases cause large errors in estimates. Caution is therefore advised when selecting the rock physics model, even if it gives a good match at one saturation it can give large errors for another.

The DEM model is computationally intensive and is hard to implement on large dimensional inverse problems, while TPEM model is relatively simple and provided a easy way of calculating elastic moduli of the sediment. However, it was seen that using the TPEM model to invert results from this model did not give satisfying results. This challenge can to some extent be bypassed by using Monte Carlo methods, but even in this case it will demand large amounts of computing time.

4.2 Suggestions for future work

Inversion of seismic AVA data for hydrate concentration has been investigated in this thesis. However, this was only done for data sets corresponding to a single set of hydrate saturation and porosity. These methods can be extended to inversion for a full reservoir model. In this case, Monte Carlo methods discussed in the previous chapter can be useful. The DEM model

can be problematic to use in this case due to large computation time. It can therefore also be useful to derive a less computationally expensive alternative.

References

Aki, K. and P. Richards (1980). Quantitative seismology: Theory and methods, Volume 2. Freeman and Company.

Aster, R. C., B. Borchers and C. H. Thurber (2013). Parameter estimation and inverse problems, second edition. academic press, Elsevier Inc.

Auld, B. A. (1973). Acoustic fields and waves in solids, Volume 1. Wiley & Sons.

Batzle M. and Z. Wang (1992). Seismic properties of pore fluids. Geophysics **57**, November.

Bonilla, L. L. and J. B. Keller (1985). Acoustoelastic effect and wave propagation in heterogeneous weakly anisotropic materials. J. Mech. Phys. Solids, **33**, 241-261.

Dvorkin, J. and A. Nur (1995). Elasticity of high-porosity sandstones: Theory for two North Sea data sets. Geophysics, **61**.

Dvorkin, J., M. Prasad and A. Sakai (1999). Elasticity of marine sediments: Rock physics modeling. Geophysical Research Letters, **26**, 1781-1784.

Eshelby, J. D. (1957). The determination of the elastic field of an ellipsoidal inclusion, and related problems. Proceedings of the Royal Society of London. Series A, Mathematical and Physical Sciences, **241**, 376-396.

Helgerud, M. B., J. Dvorkin, A. Nur, A. Sakai and T. Collet (1999). Elastic-Wave velocity in marine sediments with gas hydrates: Effective medium modeling. Geophysical Research Letters, **26**, 2021-2024.

Hill, R. (1952). The elastic behavior of a crystalline aggregate. Proc. Phys. Soc., A **65**, 349-354.

Hornby, B. E., L. M. Schwartz and J. A Hudson (1994). Anisotropic effective-medium modeling of elastic properties of shales. Geophysics, **59**, 1570-1583.

Jakobsen, M. (1998). Acoustics of complex porous media. Ph.D. Disertation, University of Bergen.

Jakobsen, M., J. A. Hudson, T. A. Minshull and S. C Singh (2000). Elastic properties of hydrate-bearing sediments using effective medium theory. Journal of Geophysical Research, **105**, 561-577.

Jakobsen, M., T. A. Johansen and B. O. Ruud (2001). Modeled velocity and reflectivity properties of anisotropic hydrated sediments. Journal of Computational Acoustics, **9**, 1507-1522.

Krebes, E. S. (2004). Seismic forward modeling Cseg Recorder, 28-39.

Kvenvolden, K. A., M. A. McMenamin (1980). Hydrates of natural gas: a review of their geological occurences. U. S. Geological Survey, Circular No. 825.

Kvenvolden, K. A. (1993). Gas hydrates-geological perspective and global change. Reviews of Geophysics, **31**, 173-187.

Kvenvolden, K. A. (2000). Natural Gas Hydrate: Background and History of Discovery. Natural Gas Hydrate in Oceanic and Permafrost Environments, pp 9-16.

Lee, M. V., D. R. Hutchinson, T. S. Collet and W. P. Dillon (1996). Seismic velocities for hydrate-bearing sediments using weighted equation. Journal of Geophysical Research, **101**, 20347-20358.

Mavko, G., T. Mukerji and J. Dvorkin (2009). The rock physics handbook: Tools for seismic analysis of porous media. Cambridge University Press.

Menke, W. (2012). Geophysical data analysis: discrete inverse theory, MATLAB edition, third edition. academic press, Elsevier Inc.

Morris, P. R. (1969). Averaging fourth-rank tensors with weight functions. Journal of Applied Physics, **40**, 447-448.

Mura, T. (1982). Micromechanics of defects in solids. Martinus Nijhoff Publishers.

Murphy, W. F. (1982). Effects of Microstructure and Pore Fluids on the acoustic Properties of Granular Sedimentary Materials. Ph.D. Disertation, Stanford University.

Nishizawa, O. (1982). Seismic velocity anisotropy in a medium containing oriented cracks: Transversely isotropic case. J. Phys. Earth, **30**, 331-347.

Nobes, D. C., H. Villinger, E. E. Davis and L. K. Law (1986). Estimation of Marine Sediment Bulk Physical Properties at Depth From Seafloor Geophysical Measurements. Journal of Geophysical Research, **91**, 14033-14043.

Nur, A., G. Mavko, J. Dvorkin, D. Galmudi (1998). Critical Porosity: A key to Relating Physical Properties to Porosity in Rocks. The Leading Edge, **17**, 357-362.

Reuss, A. (1929). Berechnung der fliessgrense von mischkristallen auf grund der plastizitatbedingung fur einkristalle: Zuitschrift fur Angewandte Mathematik aus Mechanik, **9**, 49-58.

Rüger, A. (1997). P-wave reflection coefficients for transversely isotropic models with vertical and horizontal axis of symmetry. Geophysics, **62**, 713-722.

Sayers, C. M. (1994). The elastic anisotropy of shales. Journal of Geophysical Research, **99**, 764-774.

Schoenberg, M. and J. Protazio (1980) Zoeppritz rationalized and generalized to anisotropy. Journal of Seismic Exploration, **1**, 125-144.

Sheng, P. (1990). Effective-medium theory of sedimentary rocks. Physical Review B, **41**.

Sloan, E. D., A. C. Koh (2009). Clathrate Hydrates of Natural Gases, 3rd edition. New York.

Tarantola, A. (2005). Inverse problem theory and methods for model parameter estimation. Society for Industrial and Applied Mathematics Philadelphia.

Thomsen, L. (1956). Weak elastic anisotropy. Geophysics, **51**.

Voigt, W. (1928). Lehrbuch der Kirstallphysik: Teubner.

Waite W.F., M.B. Helgerud, A. Nur, J.C. Pinkston, L.A. Stern, S.H. Kirby and W.B. Durham (1999). Laboratory Measurements of Compressional and Shear Wave Speeds Through Methane Hydrate. 3rd International Conference on Gas Hydrates.

Willis, J. R. (1977). Bounds and self-consistent estimates for the overall properties of anisotropic composites. J. Mech. Phys. Solids, **25**, 185-202.

Zoeppritz, K. (1919). Erdbebenwellen VIIIB, On the reflection and propagation of seismic waves. Göttinger Nachr., **1**, 66-84.